Meta(llic) Clay

Molding and Firing of Multibody Systems

de Jong, P.H.

DOI
10.4233/uuid:ae72c06d-7e7c-41ad-a558-f040348845ec

Publication date
2025

Document Version
Final published version

Citation (APA)
de Jong, P. H. (2025). *Meta(llic) Clay: Molding and Firing of Multibody Systems*. [Dissertation (TU Delft), Delft University of Technology]. https://doi.org/10.4233/uuid:ae72c06d-7e7c-41ad-a558-f040348845ec

meta(llic) clay

molding and firing of multibody systems

pier h. de jong

Meta(llic) Clay

Molding and Firing of Multibody Systems

Proefschrift

ter verkrijging van de graad van doctor
aan de Technische Universiteit Delft,
op gezag van de Rector Magnificus, prof. dr. ir. T.H.J.J. van der Hagen,
voorzitter van het College voor Promoties,
in het openbaar te verdedigen op
donderdag 20 november 2025 om 15:00 uur.

door

Pier Hendrik DE JONG

werktuigbouwkundig ingenieur, Technische Universiteit Delft, Nederland,
geboren te Sneek, Nederland.

Dit proefschrift is goedgekeurd door de promotoren.

Samenstelling promotiecommissie bestaat uit:

Rector Magnificus,	voorzitter
Prof. dr. Amir A. Zadpoor,	TU Delft, *promotor*
Dr. Mohammad J. Mirzaali,	TU Delft, *promotor*

Onafhankelijke leden:

Prof. dr. C. A. Dransfeld,	TU Delft
Prof. dr. ir. J. L. Herder,	TU Delft
Prof. dr. ir. M. Langelaar,	TU Delft
Prof. dr. ir. H. van der Kooij,	Universiteit Twente
Prof. dr. M. R. K. Mofrad,	University of California, Berkeley

The research leading to these results has received funding from the Dutch Research Council under NWO agreement number 16582, "Metallic clay: shape-matching orthopaedic implants".

Keywords: shape; morph; lock; kinematic; metamaterial

ISBN: 978-94-6518-170-7

An electronic copy of this dissertation is available at
`https://repository.tudelft.nl/`.

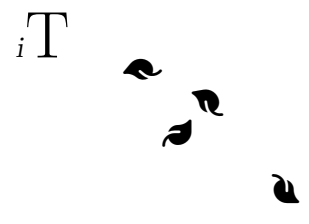

s t ᵉʳrt s ***S*** o$\mathcal{F}f$

emβaЯK

floatinᵍ at the bottom of a wanderfal

stiλl r0ugH and unpolıshᵉd

inqUieto

e v e n t u a l l y i t p i c k s u p

m o l d i n g shape . . . perfcetion nor disaster

many misprints and ditto adventures further

here we are —noflik—

welcome

Contents

Summary

Shape-morphing and shape-locking describe objects' ability to transform their shape and stay in that state, respectively. These qualities often come into play when grabbing or supporting an object. The contact area is increased by changing the shape, after which sustaining the shape maintains the support over time. We can imagine several ways of implementing this in engineered structures. One way of implementing shape-morphing and -locking is using kinematic movement, where a structure comprises relatively rigid parts connected by joints that allow motion. This work focuses on this type and presents a framework for analyzing it.

We identified and studied the factors determining the performance of kinematic morphing and locking structures. Three distinct steps were employed that explore the envelope of possible designs by i) creating and verifying a morphing modeling approach based on multibody dynamics principles, ii) analyzing a morphing and locking structure by applying the model, designing and experimentation, and iii) analyzing the effects of design parameters on the morphing and locking qualities in the light of geometrical features such as curvature. Spanning these steps, we developed several structures and fabricated them with additive manufacturing. These structures are i) a 3D modular system that allows easy experimentation with layouts and joint types, ii) an essentially 2D system that deforms in-plane and is selectively and reversibly locked by applying magnetic fields, and iii) a 3D deforming non-assembly metallic structure that can follow single and double curvatures and is irreversibly locked as a whole by applying bone cement. To assess the performance of these structures, in addition to the presented simulation approach, we developed methods that test the physical morphing and locking qualities visually and

mechanically. These methods included 3D-scanning and mechanical testing, accompanied by digital image correlation to measure full-field strain distribution.

The presented framework shows the potential of kinematic shape-morphing and -locking mechanisms to endow structures with new functionalities. Specifically, we showed that structures incorporating the mechanism can be rationally designed, manufactured, and assessed. A multi-body model predicts the morphing behavior accurately. We can use such a method to design the structures for specific applications such as orthopedic implants or soft robotics. Locking the mechanism as a whole or per individual degree of freedom obstructed the morphing capability effectively, whether or not in a reversible manner. Simulations and experiments show that we can alter the transformation and load-bearing performance of the structures as desired by changing their design parameters. The matching capacities are affected by parameters like structural body shape, dimensional ratios, and the curvature of the to-be-attained shape. These principles can be further developed and tailored for specific needs in a variety of fields.

Propositions

1. Degrees of freedom decrease freedom of design. (*this dissertation*)
2. Locking is merely a motion resistance increase. (*this dissertation*)
3. Foremost, dissertations are a testament to one's wanderings.
4. The researchers' job is to morph professors' ideas into rationality.
5. Proper advice supports one's thinking instead of pose a solution.
6. Discontent and inspiration are viral; they spread, skip, and linger.
7. Solutions are mental products; you think, try, tire ... and settle.
8. Every dead-end brings one closer to the right track.
9. Every question is an invite to commitment.
10. Every answer is non-exclusive and trivial.

Samenvatting

Vormverandering en vormvergrendeling verwijzen respectievelijk naar het vermogen van objecten om van vorm te veranderen en in die toestand te blijven. Deze eigenschappen zijn van belang bij het grijpen of ondersteunen van een object. Door de vorm aan te passen wordt het contactoppervlak vergroot; vervolgens zorgt het vasthouden van de vorm voor blijvende ondersteuning. Er bestaan verschillende manieren om dit principe toe te passen in technische constructies. Eén benadering maakt gebruik van kinematische beweging, waarbij een structuur bestaat uit relatief stijve onderdelen die met gewrichten zijn verbonden en zo beweging toelaten. Dit werk richt zich op deze benadering en stelt een analyse raamwerk voor.

We hebben de bepalende factoren onderzocht die invloed hebben op de prestaties van kinematisch vervormbare en vergrendelbare constructies. Drie opeenvolgende stappen werden gebruikt om het ontwerpbereik te verkennen: i) het opzetten en verifiëren van een vervormingsmodel gebaseerd op meerlichaamdynamica, ii) het analyseren van een structuur met behulp van het model, ontwerp en experimenten, en iii) het bestuderen van de invloed van ontwerpvariabelen op vervorming en vergrendeling in relatie tot geometrieën zoals kromming. In het kader van deze stappen ontwikkelden en vervaardigden we diverse structuren via additieve productie. Deze structuren zijn: i) een 3D modulair systeem dat experimenteren met opstellingen en scharnieren mogelijk maakt, ii) een voornamelijk 2D systeem dat in het vlak vervormt en selectief, omkeerbaar kan worden vergrendeld met behulp van magnetische velden, en iii) een 3D metalen structuur zonder assemblage die enkel- en dubbelgekromde vormen volgt en als geheel onomkeerbaar wordt vergrendeld met botcement. Ter evaluatie van

deze structuren ontwikkelden we, naast simulaties, testmethoden om de fysieke vervormings- en vergrendelingsprestaties zowel visueel als mechanisch te beoordelen. Deze methoden omvatten onder meer 3D-scannen, mechanische tests en digitale beeldcorrelatie om spanningsverdelingen in kaart te brengen.

Het voorgestelde raamwerk toont het potentieel van kinematische vervorming en vergrendeling om structuren met nieuwe functionaliteiten uit te rusten. We tonen aan dat structuren met dit mechanisme doelgericht ontworpen, geproduceerd en geëvalueerd kunnen worden. Een multilichaammodel voorspelt het vervormingsgedrag accuraat. Deze aanpak kan worden ingezet voor toepassingen zoals orthopedische implantaten of zachte robotica. Het vergrendelen van het mechanisme in zijn geheel of per afzonderlijke bewegingsvrijheid blokkeert vervorming effectief, al dan niet omkeerbaar. Simulaties en proeven tonen aan dat het vervormings- en draagvermogen naar wens kan worden beïnvloed door ontwerpkeuzes. Factoren zoals vorm, afmetingen en de kromming van de beoogde eindvorm spelen hierin een belangrijke rol. Deze principes zijn verder te ontwikkelen voor uiteenlopende toepassingen.

Stellingen

1. Vrijheidsgraden beperken ontwerpvrijheid. (*dit proefschrift*)
2. Borging is slechts bewegingsweerstand verhoging. (*dit proefschrift*)
3. Boven alles, tonen proefschriften iemands omzwervingen.
4. De onderzoekerstaak is het kneden van professor's ideeën tot logica.
5. Goed advies helpt iemands denken en legt geen oplossing op.
6. Onvrede en inspiratie zijn viraal; ze verspreiden, missen en gisten.
7. Oplossingen zijn mentaal: je denkt, probeert, vermoeit ... en schikt.
8. Elke doodlopende weg geeft meer richting.
9. Elke vraag is een uitnodiging tot toewijding.
10. Elk antwoord is niet-uitsluitend en triviaal.

Chapter 1

Introduction

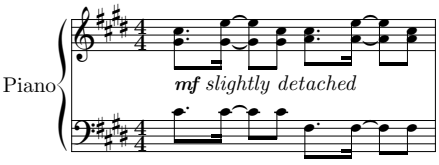

Ed Sheeran, Steve Mac and John McDaid,
opening bar from *Shape of You* (2017)

As if it were made for it, it fits like a glove [1]. A perfectly fitting shoe follows the contours of the foot [2], a chair adapts to its user's posture [3], and even a cat instinctively finds comfort in the tightest spaces [4]. From playing with a shape sorter as a child to fitting an equation to data [5], the concept of a perfect fit is deeply embedded in our daily experiences. The phrase "If I fits, I sits" humorously encapsulates the innate satisfaction of an object that conforms snugly to its environment. However, this satisfaction is not only psychological; it also has tangible functional benefits.

Beyond the personal comfort of a well-defined shoe or chair, the principle of shape adaptation plays a critical role in various engineering and design applications. In architecture, adaptive façades optimize energy efficiency and aesthetics [6]. In furniture design, modular and morphing elements enhance ergonomic support [7]. Aviation engineers develop shape-morphing wings for improved aerodynamics and fuel efficiency [8],

while soft robotics leverages compliant structures for dexterous manipulation [9]. Even in biomedical engineering, implantable devices are designed to morph and conform to biological tissues for better integration [10]. These examples are just a glimpse [11] of the broad spectrum of fields in which shape-morphing technologies are harnessed for both functional and aesthetic gains.

One size fits all: The need for shape-matching mechanisms. One conventional approach to achieving a perfect fit involves designing objects with fixed geometries tailored for specific applications. However, this bespoke strategy is inherently limited. Custom fabrication enhances precision but increases costs, manufacturing time, and the lack of adaptability to unexpected variations. A more universal "one-size-fits-all" solution would be a material or structure capable of adjusting its shape to accommodate different contours and applications.

Consider a bed that adapts to different body types, optimizing comfort for each user. Similarly, a robotic grasper capable of securely handling delicate drinking glasses of varying shapes and sizes requires a mechanism that conforms to each object while maintaining a firm grip. In such cases, a shape-matching system must provide flexibility during adaptation and stability once the desired shape is reached. This dual challenge, achieving morphability while ensuring structural integrity, guides the search for an effective and versatile solution.

Matching and maintaining: the role of locking mechanisms. Once a structure has morphed into a desired shape, it must maintain that configuration under operational loads. A shape that conforms well distributes stresses evenly, potentially reducing peak forces in mechanical systems and enabling the effective distribution of other loads, such as thermal or chemical stresses. A structure that can morph shape and then be locked in that shape offers these load-supporting features for different cases with various shapes.

Nature offers inspiration in the form of materials such as clay, which can be molded into any form before being solidified by drying or firing [12] (Figure 1.1a). This ability to shape and set suggests an ideal approach towards an adaptable yet stable material system. However, traditional natural clay has certain limitations. For example, it lacks tunability in strength, flexibility, and other material properties. Making artificial clay-

like materials, such as cement, could improve the usability and give the desired material properties. Still, one is then restricted to tuning material properties only. A more refined approach would be to mimic the formability of clay while integrating custom mechanical properties tailored for specific applications. This pursuit leads to the concept of a metamaterial system that can be shaped and then "locked" in place, providing both adaptability and structural reliability.

Metametal: a structural approach to morphing and locking. If we restrict our search to continuum materials, we miss the opportunity to fine-tune mechanical properties, such as weight, strength, and biocompatibility features, which are crucial for application in biomedical devices or lightweight aerospace components. Instead, by exploring metamaterials, we shift our focus from altering material properties to engineering structural designs that enable morphing and locking.

A promising approach is to leverage additive manufacturing to fabricate intricate lattice structures composed of relatively rigid materials, such as metals. By incorporating movable joints, these structures gain the capacity to deform in a restrained way while retaining the strength and durability of metals. This principle underlies the concept of "metallic clay" [13], where discrete kinematic structures are designed to emulate traditional clay's moldability and setting properties. Unlike a continuum material, metallic clay consists of interconnected elements that provide mechanical flexibility during morphing and structural rigidity after locking. The transition from continuum deformable materials to discrete kinematic architectures represents a fundamental shift in how we approach shape adaptation. Figure 1.1b illustrates this conceptual transformation.

Craft & conquer: design, manufacturing, and analysis challenges. The shift from continuous materials to kinematic metamaterials presents several design, fabrication, and functional performance challenges. A major challenge is achieving sufficient deformability by introducing numerous joints, which increase the system's degrees of freedom. Many degrees of freedom on their part hinder the effective locking to transition from a flexible state to a rigid one. The numerous degrees of freedom in the flexible state and the change in these degrees of freedom introduce complexity in predicting the morphing behavior of these highly articulated structures.

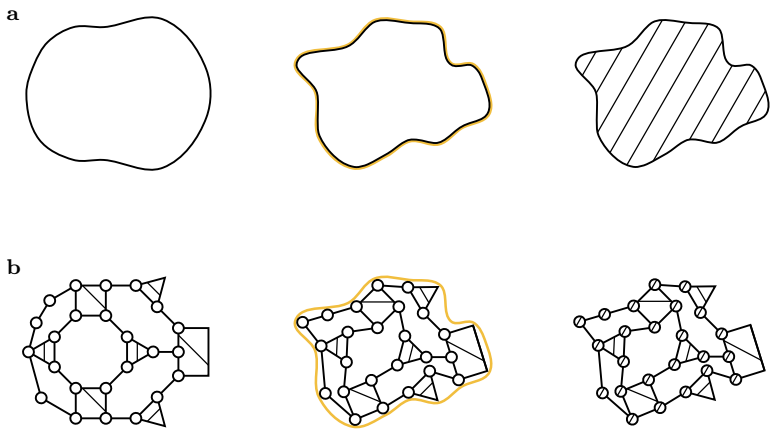

Figure 1.1: (Caption on next page.)

Figure 1.1: Clay behavior imitated by "metallic clay". a) Continuous morphing by material deformation *vs.* b) discrete morphing by kinematic joint deformation. The initial shape of the object displayed on the left is morphed into a substrate/goal shape as depicted in the middle. After "firing", the object stays in this configuration as shown on the right.

As in many instances, design, manufacturing, and analysis are highly intertwined. Manufacturing poses additional hurdles to the design, especially if structures are to be produced efficiently without requiring extensive assembly or other post-processing. Numerous joints complicate manufacturing and operation since each additional degree of freedom requires activation in morphing and locking. In effect, computational complexity in modeling and simulation is also increased. Unlike some traditional engineering problems where behavior can be predicted using closed-form analytical solutions, morphing kinematic systems often demand numerical or experimental validation due to their complex motion characteristics. These challenges necessitate a deeper exploration of these structures to develop a robust framework for their design and application.

Scope and research approach. This thesis explores the theoretical foundations and practical implementation of metallic clay, laying the foundation for its integration into a broader engineering framework. In this case, the concept, *i.e.*, a mechanism deforming with many joints that can be locked, is explored with a foundational approach. Inspiration is drawn from existing tools that are successfully used in creating and analyzing deforming mechanisms. However, in order to avoid the introduction of unnecessary complexities, these are not used directly. Relying directly upon fully developed tools might limit the directions of design and analysis in an early stage. Instead, here we provide insight into the concept's viability and future possibilities by employing seemingly elementary methods. These methods have not been used previously, in general in engineering or specifically for metallic clay.

We systematically investigate the metallic clay concept. Therefore, we research mathematical and physical principles of kinematic shape morphing, the role and implications of shape locking in simulations and practice, and the design parameters' influence on overall system functioning in morphing and locking. This naturally leads to the employment of an approach in three stages (Figure 1.2):

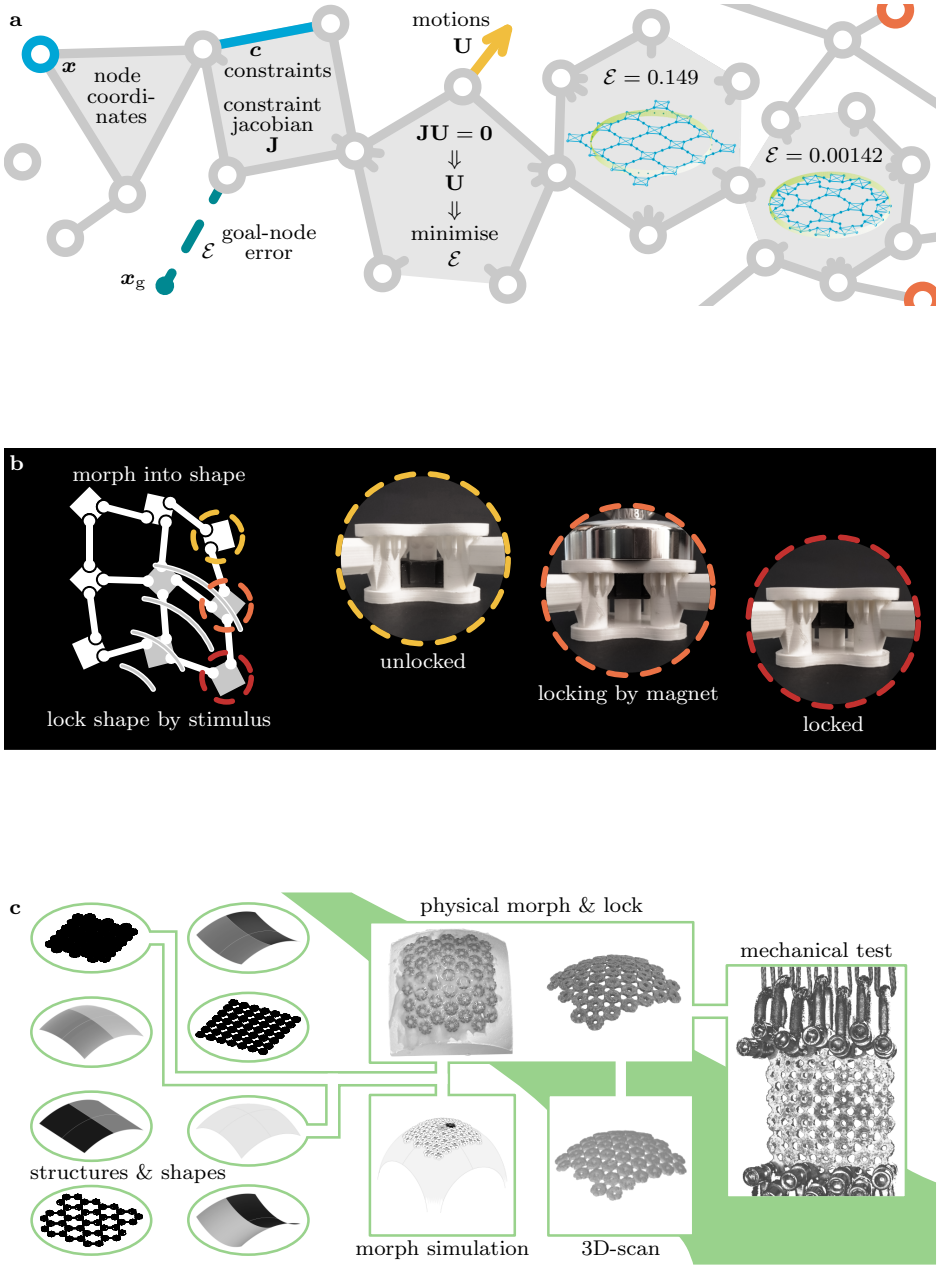

Figure 1.2: (Caption on next page.)

Figure 1.2: Graphical representation of the research stages: a) Morphing Model, b) Locking Lattice, and c) Discerning Design.

- **Morphing Model (Chapter 2).** A multibody modeling approach analyzes the fundamental morphing behavior of kinematic structures. By treating the system as an assortment of relatively rigid parts coupled by movable joints, we focus on kinematics rather than dynamics, enabling the precise characterization of shape adaptation. Modular prototypes are developed to validate the applicability of this modeling framework in real-world scenarios. The straightforward method shows how metallic clay can be simulated effectively by focusing fully on kinematics. (Figure 1.2a, modified from [14].)

- **Locking Lattice (Chapter 3).** To ensure stability after morphing, mechanical locking is introduced. The proposed system consists of bodies and struts connected by hinges made from polymer-metal composites with magnetically activated locking mechanisms. The effectiveness of these locks is evaluated through simulation and physical testing, examining their ability to constrain degrees of freedom and enhance structural rigidity. (Figure 1.2b, modified from [15].)

- **Discerning Design (Chapter 4).** The influence of geometric parameters on morphing and mechanical performance after locking is explored using chain-mail-like structures composed of interconnected elements with spherical joints. Non-assembly metallic structures are fabricated, and their adaptation to single and doubly curved shapes is investigated. The relationship between structural design choices (*e.g.*, triangular vs. square body patterns) and mechanical performance is assessed through simulations and experimental testing. (Figure 1.2c, modified from [16].)

Pursuing a universally adaptable shape-matching system combines elements of mechanical engineering, materials science, and computational modeling. By drawing inspiration from nature and leveraging modern manufacturing techniques, metallic clay offers a novel approach to achieving both morphing flexibility and post-deformation stability. This thesis aims to establish a foundational understanding of kinematic metamaterials and their potential for future implementations in adaptive structures.

Chapter 2

Morphing Model

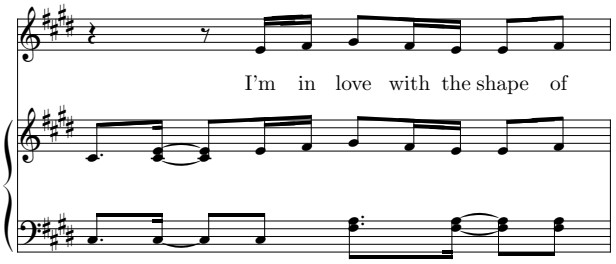

Ed Sheeran, Steve Mac and John McDaid,
first chorus bar from *Shape of You* (2017)

Abstract

Shape-morphing structures have the ability to adapt to various target shapes, offering significant advantages for many applications. However, predicting their behavior presents challenges. Here, we present a method to assess the shape-matching behavior of shape-morphing structures using a multibody systems approach wherein the structure is represented by a collection of nodes and their associated constraints. This representation preserves the kinematic properties of the original structure while allowing for a rigorous treatment of the shape-morphing behavior of the underlying metamaterial. We assessed the utility of the proposed method by applying

Modified from [14]

it to a wide range of 2D/3D sample shape-morphing structures. A modular system of joints and links was also 3D printed for the experimental realization of the systems under study. Both our simulations and the experiments confirmed the ability of the presented technique to capture the true shape-morphing behavior of complex shape-morphing metamaterials.

Keywords

multibody system; shape-morphing; shape-matching; kinematic; metamaterials.

2.1 Introduction

Shape transformation or shape-morphing is a ubiquitous phenomenon in nature. Organic materials, such as clay, exhibit shape-morphing. Living organisms manifest such behaviors too. Examples are plants, such as codariocalyx motorius (or telegraph plants), venus flytraps, pine cones, or animals, such as octopuses with their tentacles or tree frogs and their toe pads [17–23]. Many biological materials can deform their bodies substantially without losing their integrity in a response to external stimuli, such as temperature, humidity, and predation. Shape-morphing then serves as a means to facilitate other biological processes. The microstructures of such biological materials are responsible for their (dynamic) shape-morphing behavior.

Shape-morphing has numerous applications in (high added value) industries [23]. These include architecture [6, 24], furniture [7], automotive (interior [25], exterior [26]), soft robotics [9], and biomedical engineering. In those fields, we often tweak structures on the microscale to make them morph their shape in a way that they can resemble the contour of another object. This type of shape transformation is useful when an object needs to maximize its contact area with another object (Figure 2.1a). Changing the shape of grippers and fixtures to comply with the shape of the objects they grab onto or propel over helps in distributing the contact forces in the most favorable manner. To design shape-morphing objects that deliver the most favorable shape transformation properties, designers often resort to architected materials otherwise referred to as metamaterials [27].

Metamaterials allow us to design shape-morphing objects that incorporate other desired properties as well. Materials like clay are almost perfect in matching shapes, but are also continua. A more porous meta-material could have the shape-morphing properties of clay but be lighter or offer other advantages afforded by its cavities (*e.g.*, bony ingrowth in the case of orthopedic implants). Furthermore, an architected metamaterial makes it possible to realize effective (mechanical) properties that the base material used to create the metamaterial lacks. Shape-morphing metamaterials can, for example, fold (origami/kirigami) [28], bend [27, 29], or deform through kinematic joints [30]. Here, we investigate the versatility of the shape-morphing behavior of such kinematic structures.

Kinematic structures can be created from highly stiff materials but still exhibit shape transformations [13, 30]. One could, for example, connect (relatively) rigid parts through kinematic or compliant joints that are made from a base material with high stiffness. The complete structure then possesses the overall ability to easily adapt its shape. We see many manifestations of physical kinematic structures [13, 30]. A successful design of a metamaterial with a "universal shape-morphing" behavior relies on the rational geometrical design of its connecting elements (*i.e.*, links) and joints.

Here, we introduce a methodology to predict the shape-morphing behavior of architected kinematic structures. Through several examples, we illustrate the connection between this representation and physical phenomena. These predictions are essential because they enable an analysis of the envelope of possible shape transformations for any given design. Such an envelope of possible shapes can then be assessed in its own right.

Mobility describes the possible motions that an object can undergo. This number of motions is captured by the degrees of freedom (DoF) of the object. A single rigid body has six DoF in 3D: rotations around three axes and translations along three axes. A deforming body has more DoF: as many as there are isolated deform possibilities. Solidly deforming objects have infinitely many DoF and can, therefore, transform theoretically into infinitely many shapes. This is illustrated in Figure 2.1a–b. Such structures are generally studied by finite element modeling (FEM) [31–34]. Kinematic structures, illustrated in Figure 2.1c–e, have a limited number of DoF. The current designs and mathematical representations of

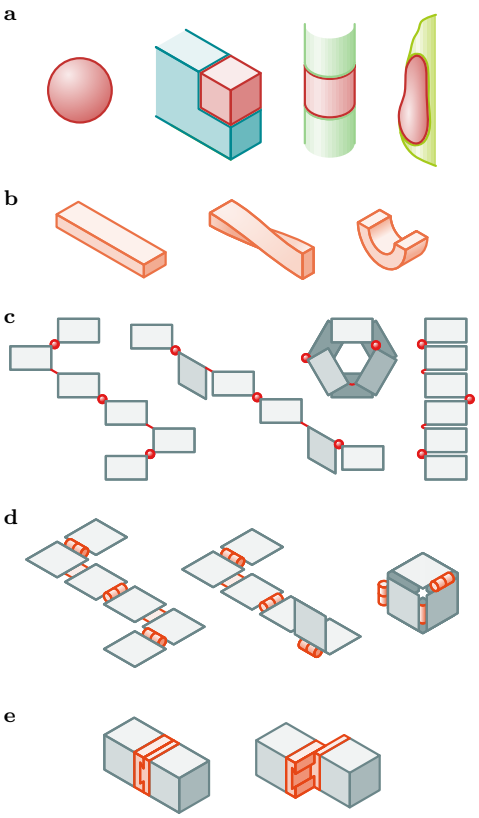

Figure 2.1: (Caption on next page.)

Figure 2.1: An illustration of the ability of different structures to deform. a) A solid deforming structure with an infinite number of DoF. A single structure can deform to take the shape of different substrates. b) A solid deforming structure with an infinite number of DoF, which more easily deforms along specific directions. c) A multibody structure with both kinematic and compliant spherical joints, providing it with many transformation DoF. d) A multibody structure with both kinematic and compliant hinges, giving it a few transformation DoF. e) A multibody structure with prismatic joint, leaving one transformation DoF. In the multibody examples, the revolute hinges are represented by "cans" [42].

shape-morphing structures often have limited mobility and can transform, or be deployed, from one starting shape into one final shape, as the final shape is programmed into the mechanism's design [28, 35–41]. The more DoF a structure has, the more shapes it can match. For a structure with limited mobility, it might be possible to predict the shapes it can attain. However, even with a finite number of DoF, a structure could match a vast number of shapes. Simulations are needed to determine whether and how well a structure can deform into different shapes. To perform these simulations, we turn to the theory of rigid multibody systems.

Rigid multibody systems describe the motions of structures consisting of rigid bodies and (kinematic) joints. Since we are modeling kinematic structures, we need to make sure their integrity is not violated. In fields that deal with shape-morphing (*e.g.* (meshing) in computer graphics/vision [43–45]), shapes are often described using points and vertices. Combining this approach with multibody principles assures that such a mesh can also describe the motions of a physical structure. This would guarantee that the integrity of the structure is preserved and that the relations between the different sections of the structure are maintained during the whole process of shape transformation. This idea of using points motivates the use of a discrete multibody approach.

A discrete multibody approach defines the entire kinematic structure by looking at specific points of interest. This is a systematic and scalable approach that we adopt here because we are primarily interested in the kinematics and not so much in the kinetics of such architected materials. A morphing shape is said to resemble another shape when they share enough contact points. To match a discrete structure to a shape, one must move selected points within the structure toward their target locations. This discretization of solid bodies to points is already used in

multibody dynamics [46–50]. Here, however, the approach is specifically tailored to study shape-morphing with as few nodes as possible. Such an approach also makes sure that kinematic structures can be modeled in a systematic way and that the obtained simulations are free from singularities. With this design representation, for any given target shape, we can determine how well a structure design is able to approach this shape. This could provide means to find combinations of design parameters that result in optimal designs. We assess the utility of the developed method by performing both simulations and experiments. The experiments are performed using an additively manufactured (AM or 3D printed) modular system that enables us to connect links and joints in arbitrarily complex ways, thereby creating many possible designs of kinematic structures.

2.2 Methods

2.2.1 Structure representation

The shape-morphing model proposed here consists of two main components, namely nodes and constraints, with which the mobility of structures can be fully described. Using this discrete approach, the overall configuration of the structure is simply defined by evaluating the local displacements of individual nodes in the 3D space. The analysis starts by expressing the system in terms of nodes and constraints. Subsequently, we find the possible motions of individual nodes and transform the complete system into a target shape that is defined as the superposition of the local motions of individual nodes. Further information on the kinetics of the system (*i.e.*, force and moments at individual nodes and links) can be also inferred from this approach but is outside the scope of the present study.

The mathematical description of a system with such few types of elements is relatively straightforward and systematic, and relies on positional descriptions provided by vectors and the applicable vector algebra. Figure 2.2 illustrates the usage of vectors for such mathematical descriptions. For each obstructed DoF, we define a constraint c that vanishes at all times (*i.e.*, $c = 0$). In what follows, we describe the theoretical model by going from a single node towards a full multibody system with different joints and a large number of DoF.

Nodes, links and bodies

Nodes are the basic elements in the description of our multibody systems and define the primary points of interest. Moreover, constraints are written in terms of the relative motions of nodes. The relative fixation and motion of nodes can all be described in terms of vectors. A single node has no dimensions. It, therefore, has only three DoF, including translations along the x-, y-, and z-axis. The coordinate of a node "1" is then defined as (Figure 2.2a)

$$\boldsymbol{r}_1 = \begin{pmatrix} x_1 & y_1 & z_1 \end{pmatrix}^{\mathrm{T}}. \tag{2.1}$$

Each system can be modelled using n nodes whose relationships with each other are described by m constraints. The overall number of DoF of the system f can then be approximated as: $f = 3n - m$. Multiple constraints may remove the same DoF. This approximation may, therefore, not hold exactly. To describe the relative motion between different (subsets of) nodes, we use the node locations and relate them to each other.

Links are defined as a constant distance between two nodes (Figure 2.2b). Such a constraint removes one DoF from the set of nodes. Therefore, a link has five DoF and can be considered as a simplified body where the rotation is undefined along the link axis. To mathematically describe a link, the length of the vector from one node to the other needs to be set equal to a constant. As is shown in Figure 2.2b, this is done through the constraint c. With the relative vector between both nodes defined as $\boldsymbol{d}$, the rigid link can be formulated as $\boldsymbol{d} \cdot \boldsymbol{d} = d$, where d is a prescribed constant of the link. The constant value of d is, thus, calculated in the original undeformed state. Since constraints need to always vanish, they are written as $c = \boldsymbol{d} \cdot \boldsymbol{d} - d = 0$.

Bodies are composed of three out-of-line nodes whose relative positions are rigidly constrained (Figure 2.2c). This is the simplest form of a rigid body, since it requires the minimum number of nodes for a fully defined set of six DoF. The (sub)system of nodes creating a rigid body has a position as well as orientations along and about all three axes. In order to not prioritize any node over another, the vectors are simply drawn in a head-tail fashion. Any other choice of node order or vector directions in which all minimal three nodes of a body are related to each other would be acceptable too.

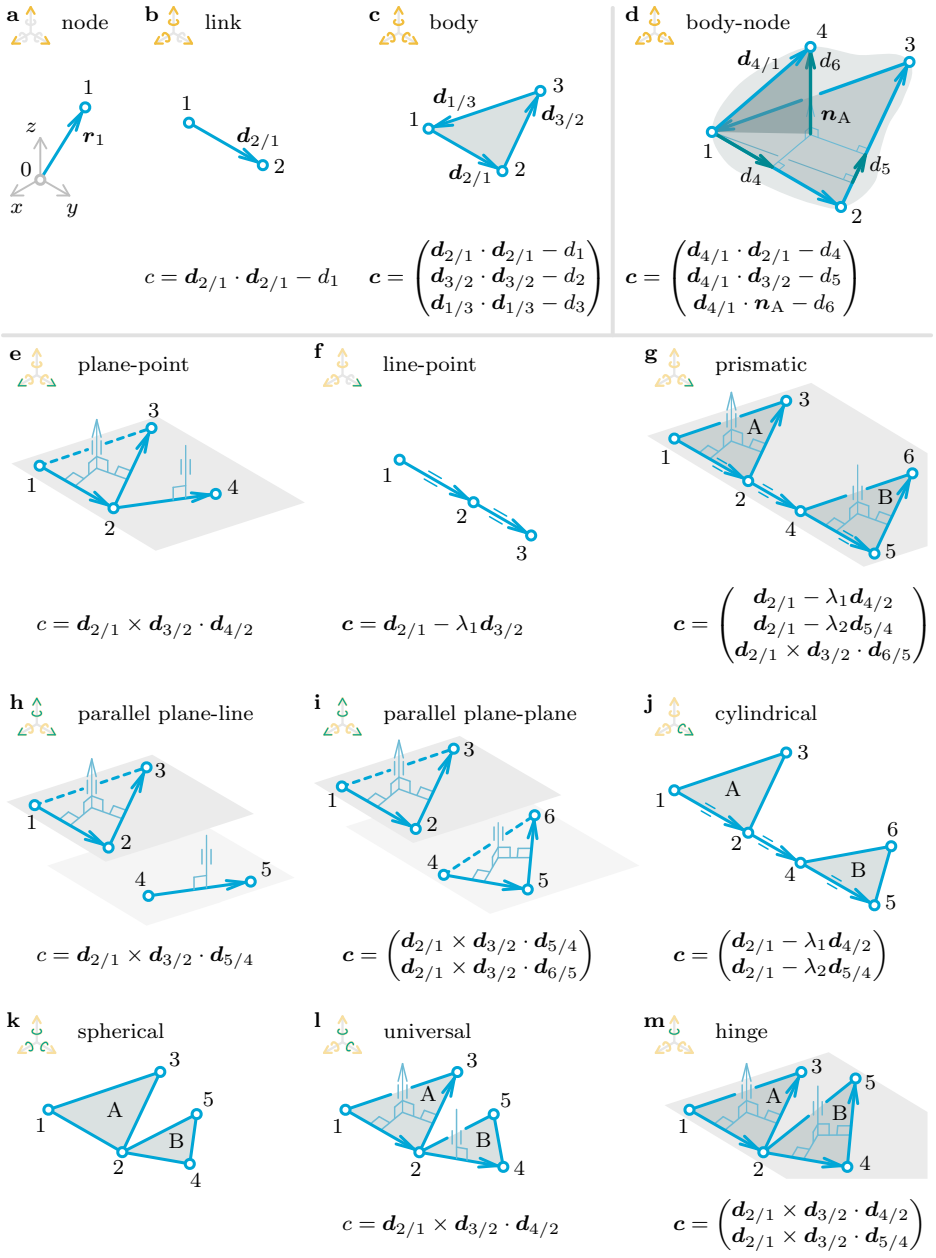

Figure 2.2: (Caption on next page.)

Figure 2.2: Description of the nodes and constraints as the building blocks of our modeling approach. Based on a multibody analysis of kinematic systems, three rigid elements are considered: a) A single node has three DoF, b) A link is created by constraining the distance between two nodes, leaving five DoF, c) Linking three nodes creates a body with six DoF. d) Nodes are rigidly added to a body through projections on a normal vector and the sides of the base plane. e)–m) Different kinds of constraints and joints can be applied in-between bodies by using orthogonal and parallel vectors. The presented list of nine examples is non-exclusive and non-exhaustive. Depending on the situation at hand, the same relative motions can be defined in different ways and more constraints can be defined in terms of the relative motions of the system components. The triads depict the possible motions, either absolute (yellow) or relative to another body (green).

The three components defined above (*i.e.*, nodes, links, and bodies) are needed to define any other relationships between the nodes. From here on, we describe two mutually compatible ways separately. First, the body is extended with more nodes than the base three. Secondly, we combine nodes with links and/or bodies in order to generate large shape-morphing structures. In a structure, we can encounter both simultaneously. Structures could have bodies with more than three nodes and many different joints between their elements.

Body-node

The number of nodes of a body can be extended beyond three (Figure 2.2d). However, singularity issues may arise when distance constraints are used for the extra nodes positioned within the plane formed by the three base nodes. We, therefore, had to find a way to attach the extra nodes while avoiding such singularities. Fortunately, the base body can be used to define the normal vectors in such a way that singularity is avoided.

We propose to extend a body's nodes beyond three by projecting the relative distance vector of the extra nodes onto the vectors related to the base plane. We start by separately projecting the relative distance vector on either two of the three base plane vectors. This provides us with two constraints. The remaining constraint is then obtained by setting the normal distance to the plane using the base plane's normal vector. To construct the normal vector, two separate vectors of the base are used (*e.g.*, $\boldsymbol{n} = \boldsymbol{d}_{2/1} \times \boldsymbol{d}_{3/2}$).

Kinematic joints

Kinematic joints, or kinematic pairs, were introduced between nodes, links, and bodies to create transformation mechanisms. Every joint within a kinematic structure allows for a certain type of motion between the nodes of the system. There are many possible joint types of which nine examples are presented in Figure 2.2e–m. This list of examples is non-exhaustive and serves solely to illustrate the principles. The relative nodal behavior of such joints can often be expressed through different definitions of constraints depending on what is most convenient in any specific case. The general idea, however, remains the same in all cases: the joints are mathematically described by constraining the movement of vectors with respect to each other.

One of the basic examples of joints that only confines translation is the plane-point joint (Figure 2.2e). This joint blocks the relative translation of any arbitrary node (*e.g.*, 4 in this particular example) with respect to a node of the plane of a rigid body. We, therefore, need a single constraint to describe this joint type. This constraint includes the normal vector of the plane that is found by taking the cross-product of two vectors of the plane. Subsequently, a third vector from a plane point towards the to-be-constrained point is projected on the normal vector. Since this projection is set equal to zero, the vector is orthogonal.

The next example of a basic joint is the line-point joint. This joint does not involve orthogonal vectors but is, instead, based on parallel vectors. The idea behind this choice is that a minimum number of nodes would be required as compared to the case where orthogonal vectors are used. These orthogonal vectors would need to be normal to the line and need an extra node to be robustly defined [47]. This is a result of the hairy-ball theorem and stems from the fact that a line has an infinite number of orthogonal vectors (Section 2.6.1). We circumvent this issue by making the vectors parallel but not necessarily equal in length. For the line-point joint, one of the vectors defines the line while the other defines the position of the third node with respect to one of the other nodes (Figure 2.2f). Both vectors are subtracted from each other to make them parallel and an extra DoF is added in the form of a multiplier λ. Eventually, this joint has three constraints but also introduces an extra DoF. The net effect of the joint, therefore, is to remove two DoF from the system.

A prismatic joint allows for relative translation between bodies (Figure 2.2g). It uses two line-point constraints and a parallel plane-line constraint. This last constraint is very similar to the plane-point joint with the difference that the vector does not originate from the body. This allows for translations as well as rotations. Other joints that allow for both rotations and translations are the parallel plane and cylindrical joints. Joints that only allow for rotation are the spherical, universal, and hinge joints. The basic elements of orthogonal and parallel vectors provide the means to define the most common types of engineering joints.

System description

Kinematic structure are fully described through their instantaneous configuration and the constrained motions between their nodes. The overall configuration of the system can be described using two main sets containing n nodal coordinates and k multipliers:

$$\boldsymbol{x} = \begin{pmatrix} \boldsymbol{r}_1^{\mathrm{T}} & \boldsymbol{r}_2^{\mathrm{T}} & \dots & \boldsymbol{r}_n^{\mathrm{T}} \end{pmatrix}^{\mathrm{T}}, \tag{2.2}$$

$$\boldsymbol{\lambda} = \begin{pmatrix} \lambda_1 & \lambda_2 & \dots & \lambda_k \end{pmatrix}^{\mathrm{T}}. \tag{2.3}$$

The mathematical relations between all these nodes are the constraints that are stored in an $m \times 1$ constraint set:

$$\boldsymbol{c} = \begin{pmatrix} c_1 & c_2 & \dots & c_m \end{pmatrix}^{\mathrm{T}} = \boldsymbol{0}. \tag{2.4}$$

These constraints, which are usually nonlinear in $\boldsymbol{x}$, make sure that the configuration of the system remains within the kinematic limitations of the structure, thereby safeguarding the overall integrity of the structure during motions.

2.2.2 Morphing simulation

Once all the nodes and constraints are defined, kinematic transformations can be analyzed. The simulation has to be performed in an iterative manner from a start configuration toward a target configuration. This iterative algorithm uses the coordinates of a target shape and minimizes the difference between the current configuration of the structure and the target one. This process continues as the structure goes through successive

steps, s, that gradually bring it closer to the target shape. The simulation stops when the change in the configuration is negligible and the algorithm is said to have converged.

We require a measure to assess the difference between the current shape and the target one [44]. For that, we adopted the normalized distance error between the current configuration of all nodes, $\boldsymbol{r}_j$, and their target configuration, $\boldsymbol{g}_j$, which is defined as

$$\mathcal{E} = \frac{1}{L}\sqrt{\frac{1}{n}\sum_{j=1}^{n}(\boldsymbol{r}_j - \boldsymbol{g}_j)\cdot(\boldsymbol{r}_j - \boldsymbol{g}_j)}, \tag{2.5}$$

where n is the total number of nodes and L is a characteristic length of the structure. This metric effectively measures the standard deviation of the distances between the locations of individual nodes and their target locations.

To assess the achieved shapes, we introduced a nondimensionalized shape factor, $\mathcal{S}$. The error defined in (2.5) measures how well a structure matches a target shape but does not tell us how the different shapes of a structure compare to each other. We, therefore, defined the shape factor such that it measures the standard deviation of the node locations from the instantaneous centroid of the structure:

$$\mathcal{S} = \frac{1}{L}\sqrt{\frac{1}{n}\sum_{j=1}^{n}\left(\boldsymbol{r}_j - \tfrac{1}{n}\textstyle\sum_{j=1}^{n}\boldsymbol{r}_j\right)\cdot\left(\boldsymbol{r}_j - \tfrac{1}{n}\textstyle\sum_{j=1}^{n}\boldsymbol{r}_j\right)}, \tag{2.6}$$

where $\frac{1}{n}\sum_{j=1}^{n}\boldsymbol{r}_j$ is the instantaneous centroid of the structure while L is a characteristic length of the structure. While this number may be the same for highly different structures, it allows for a quick first comparison between different shapes.

The iterative process of morphing the structure continues until the configuration does not change anymore. We can choose to evaluate either $\mathcal{E}$ or $\mathcal{S}$ to decide whether the end configuration has been reached. Here, we measured the absolute difference in error with respect to a step, $\bar{\mathcal{E}} = |\mathrm{d}\mathcal{E}/\mathrm{d}s|$, and repeated the process until $\bar{\mathcal{E}}$ was within a specified tolerance. This process is illustrated in Figure 2.3.

Goal coordinates

Every node, $\boldsymbol{r}_j$, needs to have a target location $\boldsymbol{g}_j$. We adopted a method where the target points are chosen based on the Euclidean distance (2-norm) between the node and a target shape. As seen in Figure 2.3a, the structure starts off with an initial configuration $\boldsymbol{x}$ (no multiplier constraints). A to-be-morphed-to shape is defined by the target configuration $\boldsymbol{x}_\mathrm{g}$. In most shape-morphing instances, the exact target location of each node is not known beforehand. The target configuration can be updated after each step based on the actual configuration of the structure. These instantaneous target locations are stored in a vector $\boldsymbol{x}_\mathrm{g}$. Note that $\boldsymbol{x}_\mathrm{g}$ always has a size of $3n \times 1$ but does not necessarily need the targets specified for each node. It is also possible to provide a certain set of new location targets for the "leading" nodes, while the target locations of the other nodes are set equal to their current location. The "leading" nodes will then move towards the new position while "pulling" the remaining nodes with them.

Mobility

A multibody system with f degrees of freedom has at least f independent ways to deform. To investigate mobility, all these possible motions will be evaluated both in isolation and in combination with each other. The independent modes of motion are the possible sets of variations in the node coordinates. For a structure undergoing a 2D motion, the modes are shown in Figure 2.3b. Having defined the constraints in the form of (2.4), we can find all the small variations which satisfy the constraints using the first derivative of (2.4) as

$$\mathbf{J} \begin{pmatrix} \mathbf{U} \\ \mathbf{\Psi} \end{pmatrix} = \mathbf{0}, \tag{2.7}$$

where $\mathbf{J}$ is the $m \times (3n + k)$ Jacobian of the constraints and $\mathbf{U}$ and $\mathbf{\Psi}$ are matrices with its null spaces. The Jacobian is calculated as

$$\mathbf{J} = \begin{pmatrix} \partial \boldsymbol{c}/\partial x_1 & \partial \boldsymbol{c}/\partial y_1 & \dots & \partial \boldsymbol{c}/\partial z_n & \partial \boldsymbol{c}/\partial \lambda_1 & \dots & \partial \boldsymbol{c}/\partial \lambda_k \end{pmatrix} \tag{2.8}$$

while the null space can be subsequently determined using singular value decomposition (SVD). The columns of the Jacobian represent small deviations that are combinations of coordinate variations and can take place

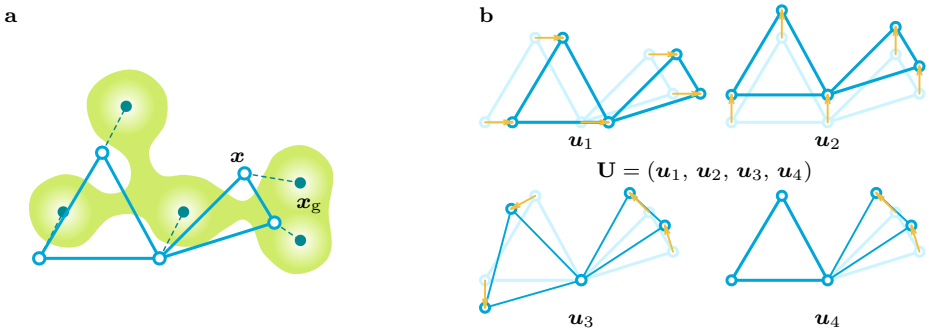

Figure 2.3: (Caption on next page.)

Figure 2.3: An illustration of the steps involved in the shape-morphing algorithm that is applied to a structure moving in 2D. The target of each node is to reach the nearest bump on the surface as seen from the top view. The process iterates through steps a)–d) until the shape error derivative $\bar{\mathcal{E}}$ is below a pre-defined threshold.

simultaneously. The separated modes containing the admissible variations of $\boldsymbol{x}$ and $\boldsymbol{\lambda}$ are then the null spaces:

$$\mathbf{U} = \begin{pmatrix} \boldsymbol{u}_1 & \boldsymbol{u}_2 & \dots & \boldsymbol{u}_f \end{pmatrix}, \tag{2.9}$$

$$\boldsymbol{\Psi} = \begin{pmatrix} \boldsymbol{\psi}_1 & \boldsymbol{\psi}_2 & \dots & \boldsymbol{\psi}_f \end{pmatrix}, \tag{2.10}$$

respectively of size $3n \times f$ and $k \times f$.

Modal superposition

Modal superposition is used to move and deform the structure to a desired configuration. In this way, the nodes move along linear paths admissible by the constraints up to the first order (Figure 2.3c). We selected and combined the admissible motions stored in $\mathbf{U}$ by minimizing the distance that the nodes travel towards their target $\boldsymbol{x}_\mathrm{g}$. Then, at each step of the motion, a change in the current configuration leads to the creation of a new configuration according to the following relationship (Section 2.6.1):

$$\boldsymbol{x}_* = \boldsymbol{x} + \mathbf{U}\left(\mathbf{U}^+ \left(\boldsymbol{x}_\mathrm{g} - \boldsymbol{x}\right)\right), \tag{2.11}$$

where $\mathbf{U}^+ = \left(\mathbf{U}^\mathrm{T}\mathbf{U}\right)^{-1}\mathbf{U}^\mathrm{T}$ is the left pseudo-inverse of $\mathbf{U}$ and both $\mathbf{U}$ and $\mathbf{U}^+$ are evaluated in $\boldsymbol{x}$. Note that the variations in $\boldsymbol{\lambda}$ are not used in the modal superposition. Since the obtained information regarding the motions is a linear approximation, multiple steps are generally required to move to a new configuration while satisfying all the applicable constraints.

Constraint satisfaction

In each step, the nodes make a small linear movement with respect to their initial configuration that tends to slightly violate the constraints of the structure. As the number of steps increases, these initially negligible errors accumulate, requiring corrective measures. In fact, nodes that are part of bodies follow a curved path that cannot be described with a linear movement. Therefore, in each step, a constraint satisfaction step

in the form of a Gauss-Newton algorithm is applied to the coordinates $(\boldsymbol{x}_*^{\mathrm{T}}, \boldsymbol{\lambda}_*{}^{\mathrm{T}})^{\mathrm{T}}$ to guarantee the constraints are satisfied up to a permissible residual (Figure 2.3d). These corrections lead to new actual configurations after each step, which are given as (Section 2.6.1):

$$\begin{pmatrix} \boldsymbol{x} \\ \boldsymbol{\lambda} \end{pmatrix} = \begin{pmatrix} \boldsymbol{x}_* \\ \boldsymbol{\lambda}_* \end{pmatrix} - \mathbf{J}^{+}\boldsymbol{c}, \tag{2.12}$$

where $\mathbf{J}^{+} = \mathbf{J}^{\mathrm{T}} \left(\mathbf{J}\mathbf{J}^{\mathrm{T}}\right)^{-1}$ is the right pseudo-inverse of the constraint Jacobian $\mathbf{J}$ and $\boldsymbol{c}$ includes the constraint errors, both evaluated in the configuration $(\boldsymbol{x}_*^{\mathrm{T}}, \boldsymbol{\lambda}_*^{\mathrm{T}})^{\mathrm{T}}$. The constraints with $\boldsymbol{\lambda}$ are affected as well and need to be corrected too. These corrections are performed in an iterative manner (within the overall iterative process) to guarantee the satisfaction of the constraints up to a permissible residual.

2.2.3 Case studies

Experiments are conducted to illustrate and validate the usage of the approach. Simulations show how different structures can be implemented and transformed into different shapes. A reconstruction with a physical modular system shows how the simulations compare to the physical world.

Simulations

For the simulations, the target shapes are point clouds that are either created through the direct applications of mathematical expressions or by converting a CAD drawing. Shapes with constant (Gaussian) curvature are created with straightforward functions. To create more irregular surfaces, we used Fourier expansions. While the "organical" CAD model is hand-drawn, any real-world physical objects could be handled similarly. The only additional step would be some type of 3D scanning.

Two parameters were defined to run the simulations. In all the simulations performed here, the characteristic length is given by

$$L = \sqrt{\frac{1}{n}\sum_{j=1}^{n} \left(\boldsymbol{r}_{j0} - \tfrac{1}{n}\textstyle\sum_{j=1}^{n} \boldsymbol{r}_{j0}\right) \cdot \left(\boldsymbol{r}_{j0} - \tfrac{1}{n}\textstyle\sum_{j=1}^{n} \boldsymbol{r}_{j0}\right)}, \tag{2.13}$$

where we use the initial structure node configurations, $\boldsymbol{r}_{j0}$, such that $\mathcal{S} = 1$ at $s = 0$. Moreover, all the simulations stopped when $|\bar{\mathcal{E}}| < 1 \cdot 10^{-6}$.

Modular physical system

To illustrate and validate the capability of the presented modeling approach, we designed a modular system to recreate some of the various joint types discussed here as physical models and demonstrate their physical kinematic motions (Figure 2.4a–e). In the created modular system, spheres represent nodes in kinematic systems. These spheres were connected to different parts to create rigid bodies that allowed for different types of motion variations. The rigid body shapes can be combined with different joint types to form shape-morphing structures (Figure 2.4f). We used 3D printers to fabricate our physical models (Section 2.6.2). Different pieces were combined to make different kinematic joints and structures with different shape-morphing behaviors. The spheres were printed using vat photopolymerization (VAT-UVL/P [51]; Form 3, Formlabs, United States; color resin). The spheres were connected to each other to create links and bodies. Links were printed using VAT-UVL/P [51] (Form 3, Formlabs, United States; grey resin) while ridged shafts and bodies were printed using material extrusion (MEX-TRB/P/PLA [51]; Ultimaker 2+, Ultimaker, The Netherlands; silver metallic filament). Different circular clamping pieces were made with vat photopolymerization (VAT-UVL/P [51], Form 3, Formlabs, United States; tough 1500 resin) which could be snapped around or into the ridges of the spheres. The shapes of these clamps determine whether or not they can rotate and with how many DoF. Different combinations of circular pieces create either a fixed, spherical, hinge, universal, or hinge connection around the sphere. The shafts are snapped into the other ends of the circular pieces. Furthermore, the shafts are snapped into tubes to create cylindrical or prismatic joints, where the prismatic joints make use of the ridges of the shafts to block any rotations.

The modular system was first evaluated for a specific structure whose morphing behavior is quite intuitive and was similarly captured by both simulations and experiments. This allowed for a comparison between the shape as predicted by the model and the physically realized shape. The model yielded the final positions of the nodes and the corresponding shape value. The physical representation of the system was put into different shapes and its node locations were recorded.

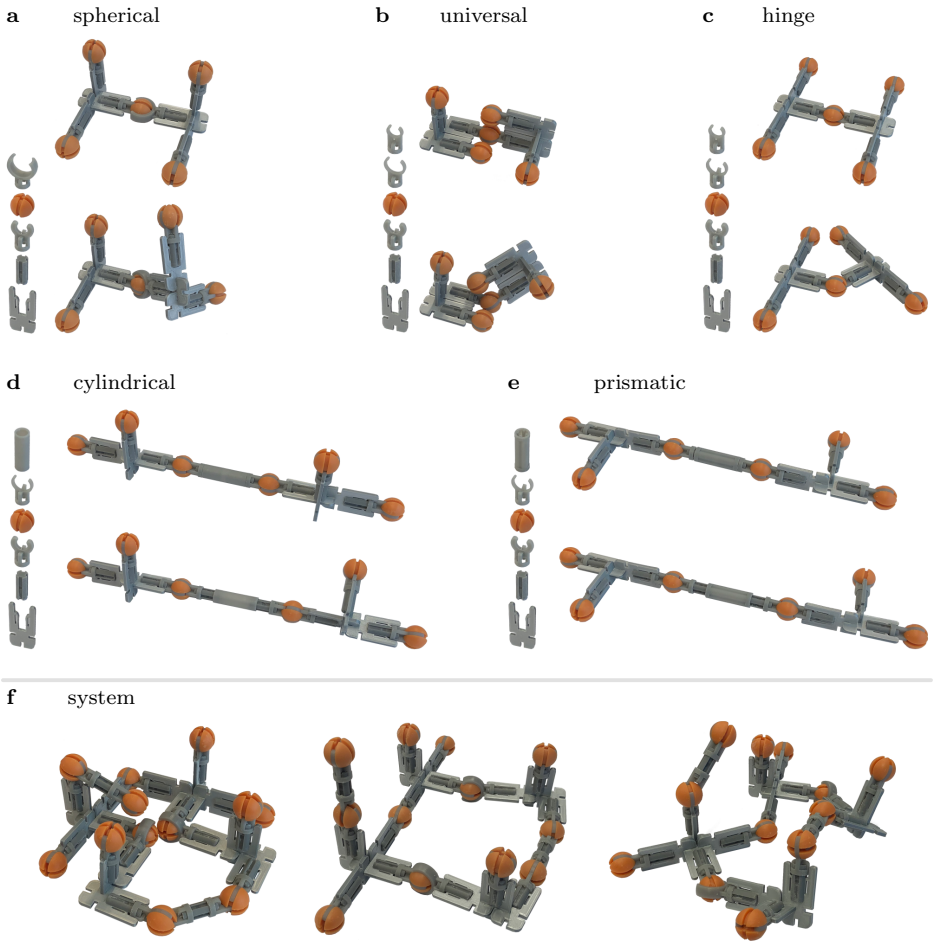

Figure 2.4: (Caption on next page.)

Figure 2.4: A modular system illustrating the physical behavior of multibody systems. a)–e) Five common kinematic joints. The modular pieces were used in different combinations to create the different behaviors of the structures. The spheres were placed such that they can be easily used in mathematical definitions of the joints. f) Different kinematic joints were combined to create versatile systems, including both closed-loop systems and systems with open ends.

Target shapes

Target shapes were physically created for the validation experiments as well (MEX-TRB/P/PLA [51]; Ultimaker 2+, Ultimaker, The Netherlands; green filament). These substrates have an open design that provides the opportunity to capture the structure's configuration once it is placed on or in the target shape. The three shapes are a circle, a cylindrical surface, and an ellipsoidal enclosure, which were sized to be compatible with the simulations (Section 2.6.2).

Configuration capturing

As for capturing the positions of individual nodes, we used a 3D optical scanner (Scan-in-a-Box-FX, Open Technologies S.r.l., Italy) and extracted the coordinates of the nodes by manually selecting the spheres from the 3D scanned point clouds. Then, the shape factor was calculated and compared between our simulations and the physical model. The characteristic length for all cases (simulation and scanning) was that of the simulation's initial configuration as calculated with (2.13).

2.3 Results

The simulation results corresponding to case studies show that the proposed design representation in the current study for modeling the shape-morphing behavior of kinematic structures works well in terms of finding the correct matching shape (Figure 2.5). The simulation and experimental results were generated by considering different sample structures that were specifically selected to showcase the different types of constraints and their associated shape-morphing behaviors. The kinematic structures used for the assessment of the morphing behaviors of the sample cases were created by defining their initial node positions and the constraints limiting the rel-

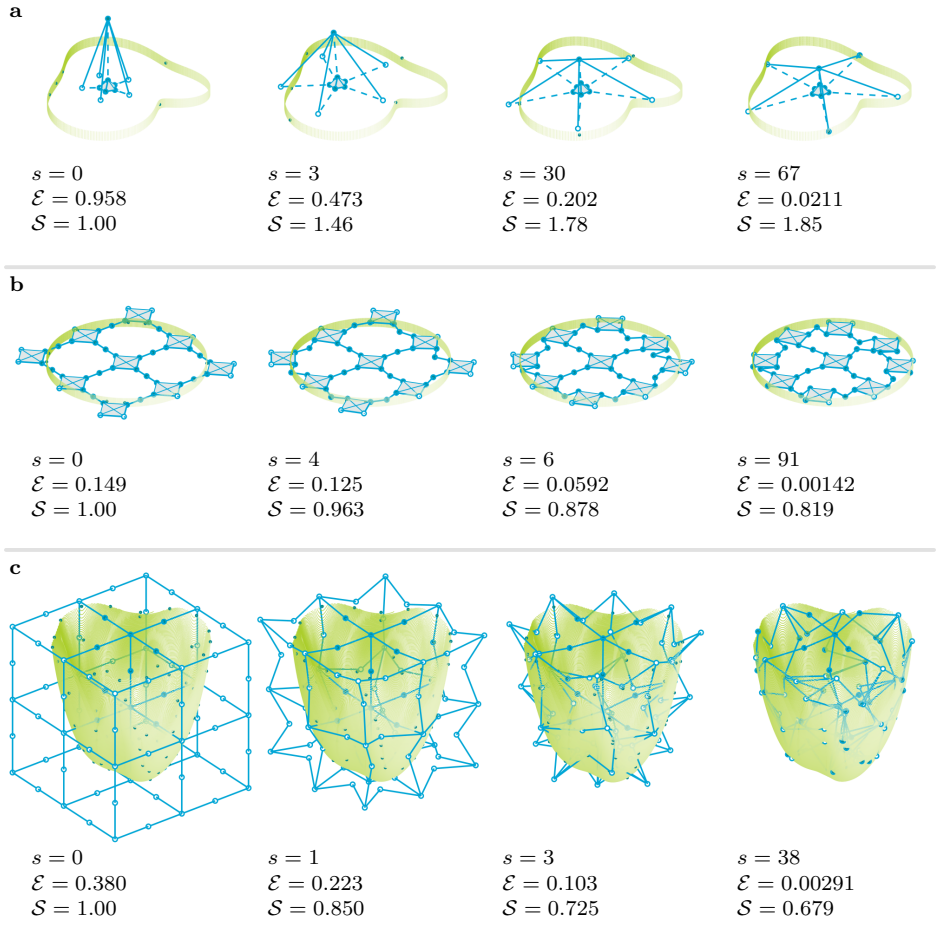

Figure 2.5: (Caption on next page.)

Figure 2.5: Three sample applications of our shape-morphing simulations. Nodes are depicted by blue circles and links are represented by blue solid lines. Line-point joints are depicted by dashed lines. For a selection of steps s, the configurations with shape factor $\mathcal{S}$ is shown. The targets for the upcoming step are shown with dots. The distance error $\mathcal{E}$ indicates how far the current configuration is from the targets. a) A "pentapod" matching its shape to a cylindrical surface with a randomly varying radius. Only the five outer nodes were moved toward the shape. Line-point constraints were used to make the outer nodes move in one plane (simultaneously). Next to the six DoF of the overall motion, this structure has only one shape-transforming DoF. b) A structure with square bodies connected by hinging links [13] was morphed into a circular shape. Only the nodes on the edges were given target locations. Plane-point constraints were used to restrain all the nodes in one plane. c) A 3D structure with spherical joints was morphed into an organically created 3D shape. Only the nodes on the bottom and side faces of the structure were given target locations.

ative motions of the nodes according to the generally developed principles (Section 2.2.1). Subsequently, a generally developed morphing algorithm (Section 2.2.2) was applied to transform the shape of the mathematical structures into a desired one. The here presented morphing simulations and the experimental comparison with a physical representation follow study-specific methods (Section 2.2.3).

An overview of some sample structures and target shapes is presented in Figure 2.5. Here, a 3D deforming "pentapod" is composed in such a way that it only has one morphing DoF (Figure 2.5a). There is a rationally designed coupling between the nodes along different axes that makes this possible. Although the space in which the movements take place is 3D, we can apply hinges in such a way that only 2D in-plane morphing of structures is possible (Figure 2.5b). This structure has multiple DoF because of the network of many hinges. A fully 3D defined structure with spherical joints has many DoF and can transform its shape into irregular 3D shapes (Figure 2.5c).

In the specific examples considered here, not all nodes were moved toward the target surface. We selected the structure's peripheral nodes as "leading nodes" that moved toward the target shape. The inner nodes were initially allowed to stay close to their starting positions. The internal nodes followed the leading nodes only when they had to provide extra movements so that the leading nodes could approach their target positions.

The simulations confirmed the capability of the structures to transform into the specific target shapes. The "leading nodes" at the edges

move toward the target shape. The nodes located at the center of the structures remained mostly in their original positions, if they did not have to accommodate the movement of the edge nodes. The residual error of the "pentapod" in (Figure 2.5a) was relatively large as compared to the other examples. That is due to the fact that its target shape is irregular and the structure has effectively only one transforming DoF. Moreover, the pentapod showed "expansion" with increasing shape factor while the shape factor of both other structures reduced. These results can be used to improve the designs of these structures in terms of shape-morphing behavior and reduce the residual error.

A comparison between the simulated shape-morphing and the experimentally obtained shapes shows that they are in agreement with each other. The 2D structure could deform into a 1D circular shape (Figure 2.6a–b), a 2D cylindrical surface (Figure 2.6c–c–d), and a 3D ellipsoidal enclosure (Figure 2.6e–f). The simulations predicted this, and although the physical dimensions and possible imperfections limited the range of motion of the physical structure, it could approximate the shape factor of the simulations.

2.4 Discussion

The multibody kinematic approach presented here provides the required steps for an initial configuration to morph into a target shape. This was initially demonstrated for different structures in a first set of simulations (Figure 2.5). To illustrate the working principles of the approach further and demonstrate the physical realization and compare it with our simulation results, we analyzed the capabilities of the presented approach in predicting the shape-morphing steps required for several arbitrary shapes.

A second set of experiments showed how one single structure can morph into multiple shapes by simply defining different target shapes. We simulated the behavior of a 2D structure that morphs into various shapes in 1D, 2D, and 3D (Figure 2.6). The simple structure consisted of two triangular bodies connected through spherical joints by a link. The same structure was morphed into three different target shapes, including a circular surface that made the structure deform in one plane along a line, a curved surface that made the structure morph into an out-of-plane shape,

and an ellipsoidal enclosure that required the structure to deform into a 3D shape. The different target shapes of the substrates were purposely chosen to give the structure compelling end shapes. Situations occurred where the combination of structure and target shape was too symmetric, leading to bifurcations. Multiple routes to the target shape were equally ideal which can lead to longer calculation times and undesired structure configurations. To circumvent this, symmetry was removed by translating or rotating the target shape slightly with respect to the morphing structure in order to break the alignment of the symmetry axes of shape and structure.

In our physical representations, we followed the exact same steps obtained from our simulations and found that the resulting shapes matched the target shapes. We need to emphasize here that the 3D printed structures had length ratios that were identical to the simulated ones. However, these physical experiments also made it clear that the intermediate steps resulting from the simulations are primarily of theoretical value. The different steps obtained for the shape-morphing process represent the shortest trajectory from the initial shape to the target shape. This means that our simulations do not take into account all the physical properties of the joints. Some of the physical properties of joints and links, such as their thicknesses, can limit their actual range of motion. One way to apply such limits in the range of motion of a node without changing the current way of defining constraints is to add an additional node (Section 2.6.3). The number and location of nodes that represent a body are chosen carefully in the experiments to represent a physical system while using as few nodes as possible. Adding nodes carelessly can make the calculations longer as well as giving undesired results (Section 2.6.4).

We used a two-step Gauss-Newton iterative procedure to make sure the shape transformation trajectory was as close as possible to the actual physical situation. In this procedure, the nodes were moved toward their target first, followed by corrections that ensured the constraints were satisfied to the desired level of accuracy. The integrity of the system was, therefore, maintained during the shape transformation process. Had we solved the model simultaneously for both target-approaching trajectories and constraint satisfaction, different final configurations would have appeared that would have significantly deviated from what is physically pos-

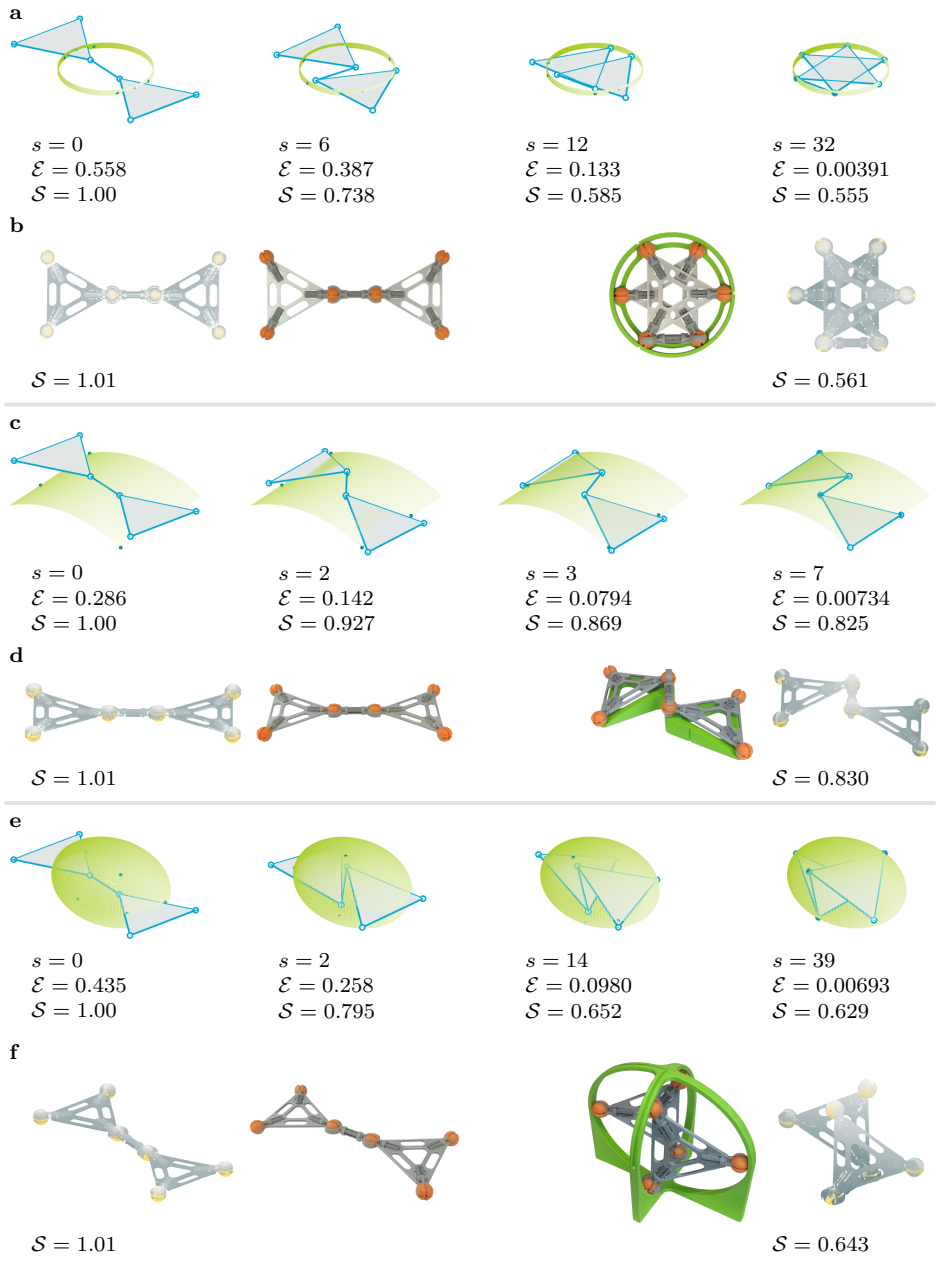

Figure 2.6: (Caption on next page.)

Figure 2.6: Simulation of the transformation of the shape of a structure with triangular bodies into three different shapes. The target shapes are a)–b) a circle, c)–d) a cylindrical surface and e)–f) an ellipsoidal enclosure. In each case, the simulated behavior is shown for selected steps s along with the physical representation of the modular system corresponding to the initial and final configurations. The blue circular nodes are physically represented by orange spheres. The 3D printed structure's shape was captured using a 3D optical scanner. From the point cloud the yellow spheres were selected manually. Both the normalized error $\mathcal{E}$ between the structure and the substrate and the normalized shape $\mathcal{S}$ are presented. The simulations stopped once the absolute error difference $\bar{\mathcal{E}}$ was below $1 \cdot 10^{-6}$. All the values were normalized with respect to a characteristic length which was chosen to be a representative value of the initial shape at $s = 0$.

sible. The physical "insertability" of such shapes would have, therefore, been less predictable. Doing the constraint satisfaction in a separate step of the iterative process is a more effective approach for maintaining the integrity of the kinematic structure as the shape transformation takes place. The final shape of the structure will then preserve its original topology.

Given that the primary purpose of the current paper is to propose a straightforward model for the study of the shape-morphing behavior of kinematic structures, we did not consider some more advanced aspects of kinematic structures, such as shape transformation in the presence of additional constraints that limit the range of motion of individual joints. Every joint could, therefore, move freely along its DoF. In reality, however, the physical nature of a structure limits the range of motion of different joints in a joint- and location-specific manner.

The primary limitation of the proposed method lies in the simplifications that make it somewhat deviate from the actual physical situation. In particular, rigid bodies were simply defined as a collection of theoretical nodes without volume. In the real world, physical bodies occupy volume and cannot penetrate into each other [52, 53]. These aspects have not yet been included in the presented modeling approach. The finite dimensions of the physical structures and the limited range of motions of joints are the other aspects missing from our approach. These omissions mean that one needs to be careful about the selection of the nodes that lie on the surface and the ones that do not. For a qualitative assessment of the shape-morphing behavior, this does not pose a problem since the overall trends are followed, but any quantitative results may be less accurate than those of more complex models.

The current version of the proposed method is also purely kinematic, meaning that stiffness is excluded from the equations. The elements of the model are, thus, either fully rigid –and thus non-deformable– or fully free to move along their DoF. Rigid bodies are, therefore, assumed to possess infinite stiffness while joints are inferred to have zero stiffness. To study how compliant bodies and joints contribute to the shape-morphing behavior of physical structures, we need to introduce forces. A theoretical spring with a finite stiffness does not limit the motion of a point in a multibody model. In reality, however, it limits the deformation that is possible without material failure. Moreover, it can also contribute to mobility through the deformation of parts that are considered rigid in this multibody approach. By introducing masses and/or stiffness values [54] into the system, it would be possible to investigate the reaction forces at different joints. Static forces in the system can then be calculated by evaluating the local stiffness in-between the nodes. This would be somewhat similar to FEM. It is important to emphasize that while multi-step simulations make it look like the kinematic structures move toward their targets, this should not be misinterpreted as a dynamic analysis. This movement purely represents the kinematically optimal path (*i.e.*, the path with the shortest least-square distance) that satisfies the imposed constraints. It is possible to extend the presented node-and-constraint model to include kinetics. The bodies would then need to have at least four nodes with assigned masses to be able to manifest the full kinetic effects of their mass and moments of inertia. Implementing non-rigid bodies is possible within the current modeling framework by assigning stiffness values to the links.

To modify the model, one can change the way through which we find the final position of nodes. In the presented method, the nearest point on a surface was used, but this can be changed to other norms, such as the 1-norm, a projection along an axis, or the Hausdorff distance [55]. These methods have been used in computer graphics algorithms [44] that have many similarities to the algorithm presented here. Another note regarding the search for the target coordinates is that representing the target shape as a point cloud makes the search computationally much more expensive than if the target shape was represented by a function. It is, therefore, advised to use a functional representation of the target shape, as this would allow for more computationally efficient minima handling.

2.5 Conclusions

We proposed a simple method for the study of the shape-morphing behavior of kinematic structures. We then applied this design representation to a number of cases to demonstrate its utility in predicting the shape-morphing behavior of a large class of architected materials consisting of links, bodies, and joints with various DoF. The simulation and experimental results obtained for the case studies confirmed the ability of the proposed technique to match kinematic structures to arbitrary shapes through a variety of mechanisms. The presented approach, therefore, provides us with a way of determining a structure's ability to transform into arbitrary shapes particularly when the target shape is complex and does not lend itself to other more rudimentary techniques of shape analysis. The methodological advances made through the proposed technique pave the way for more systematic investigations of shape-morphing phenomena, including the determination of the envelope of the shape-morphing behaviors that can be exhibited by any given kinematic structure. Such information would be also essential for the algorithmic optimization of kinematic structures with the aim of making them morph into any specific classes of shapes or for enlarging the envelope of possible achievable shapes as much as possible.

2.6 Supporting information

2.6.1 Derivation refreshers

Algebraic difficulties in line orthogonals

Finding a robust algebraic expression for a normal vector of a line is impossible. An algebraic expression is required when the vector is later used in finding (partial) derivatives. If the line is part of a plane, it is straightforward to find the normal vector. That is because there is only one normal vector. For an isolated line, however, there are infinitely many normal vectors contained in a plane. This is a common challenge in computer graphics. It can be shown that for a single line, any expression found for the normal vector has a combination of entries that result in a zero normal vector. We illustrate this by first giving some examples of applicable

numerical methods and then trying to apply them to an algebraic case.

The intuitive way (in 3D) for finding the normal vector to an isolated line is the projection of the relative position vector of the point on two distinct orthogonal vectors of the line. This is illustrated in Figure 2.7. Numerically, these vectors can always be found, even in multiple ways. Three examples are presented below:

1. One can use a (base-)vector $\hat{\boldsymbol{e}}$ that is non-parallel to $\boldsymbol{d}$. First, we find the index i of (one of) the smallest absolute component(s) of $\boldsymbol{d}$. The non-parallel vector is then $\hat{\boldsymbol{e}}_i$ where the i^{th}-component is 1. Subsequently, the normal vector is found as $\boldsymbol{n} = \boldsymbol{d} \times \hat{\boldsymbol{e}}_i$. For example, if we have $\boldsymbol{d} = (3,\, 2,\, -5)^{\mathrm{T}}$, we use $\hat{\boldsymbol{e}}_2 = (0,\, 1,\, 0)^{\mathrm{T}}$ which gives the normal vector as $\boldsymbol{n}_1 = \boldsymbol{d} \times \hat{\boldsymbol{e}}_2 = (5,\, 0,\, 3)^{\mathrm{T}}$. A second normal vector can easily be found as $\boldsymbol{n}_2 = \boldsymbol{d} \times \boldsymbol{n}_1$.

2. Another method uses the matrix product representation of the cross-product: $\boldsymbol{d} \times \boldsymbol{d} = \tilde{\mathbf{d}}\boldsymbol{d}$. By definition, this (skew-symmetric) matrix $\tilde{\mathbf{d}}$ has elements for which $\tilde{\mathbf{d}}\boldsymbol{d} = \mathbf{0}$. Therefore, the rows and columns of this matrix are all orthogonal to $\boldsymbol{d}$: $\tilde{\mathbf{d}} = (\boldsymbol{n}_1,\, \boldsymbol{n}_2,\, \boldsymbol{n}_3)$. For a non-zero vector $\boldsymbol{d}$, at least two columns of $\tilde{\mathbf{d}}$ are non-zero and could serve as useful orthogonal vectors. For example, when $\boldsymbol{d} = (3,\, 2,\, -5)^{\mathrm{T}}$, we find $\boldsymbol{n}_1 = (0,\, -5,\, -2)^{\mathrm{T}}$, $\boldsymbol{n}_2 = (5,\, 0,\, 3)^{\mathrm{T}}$, and $\boldsymbol{n}_3 = (2,\, -3,\, 0)^{\mathrm{T}}$. Note that these vectors are not mutually orthogonal among themselves.

3. For any given 3D numerical vector $\boldsymbol{d}$ of size 3×1, it is possible to find a vector $\boldsymbol{n}$ that is orthogonal to this vector such that $\boldsymbol{d} \cdot \boldsymbol{n} = 0$. There are infinitely many $\boldsymbol{n}$ that are contained in the plane of which $\boldsymbol{d}$ is the normal vector. It follows that the orthogonal vectors $\boldsymbol{n}$ can be found by determining the (right) null space of $\boldsymbol{d}^{\mathrm{T}}$, for example, by using singular value decomposition (SVD). The right-singular vectors corresponding to zero singular values describe the vectors orthonormal to $\boldsymbol{d}$.

All of the above-mentioned methods are associated with certain issues when applied algebraically. The method which requires working with the base vector involves finding the minimum numerical value of the entries of the vector, which immediately disqualifies the method. We could try

the tilde matrix method with a vector $\boldsymbol{d} = (x, y, z)^{\mathrm{T}}$. We would then obtain $\boldsymbol{n}_1 = (0, -\gamma, y)^{\mathrm{T}}$, $\boldsymbol{n}_2 = (z, 0, -x)^{\mathrm{T}}$, and $\boldsymbol{n}_3 = (-y, x, 0)^{\mathrm{T}}$. It can be seen that if we choose the first normal vector, $\boldsymbol{n}_1$, we would get $\boldsymbol{n}_1 = \boldsymbol{0}$ in the case $\boldsymbol{d} = (1, 0, 0)^{\mathrm{T}}$. Therefore, a zero normal vector is obtained for a nonzero vector, which is undesirable. Since it is unknown beforehand which column of the tilde matrix must be chosen, this method cannot be used. It appears to be the case that for any nonzero vector, one zero normal vector is found regardless of the applied method. This issue is related to the hairy ball theorem [56]. The line vectors $\boldsymbol{d} = (x, y, z)^{\mathrm{T}}$ correspond to points on a sphere's surface. The normal vectors could be interpreted as vectors tangent to the sphere, originating from $\boldsymbol{d}$. Therefore, there is always a combination of x, y, and z that gives a zero $\boldsymbol{n}$.

Finding an algebraic expression for the normal vector of an isolated line, therefore, requires an explicit definition of that normal vector. In our multibody system, this requirement can be satisfied through the addition of an extra node. Given the fact that we aim to use the minimum number of nodes, we prefer to use the multiplier method to constrain a point on a line.

Optimising the shape transformation path

In the modal superposition step of the morphing algorithm, we would like the nodes to move to their targets along the shortest path. Therefore, the modes need to be selected and scaled (through the use of weighting factors) such that their combined motion is the desired one. Mathematically, we select modes from $\mathbf{U}$ and add them to the current configuration as:

$$\boldsymbol{x}_* = \boldsymbol{x} + \mathbf{U}\boldsymbol{w}, \tag{2.14}$$

where $\boldsymbol{w}$ is a $f \times 1$ weight vector that scales the contribution of each mode to the motion.

In order to find $\boldsymbol{w}$ that results in the next configuration closest to the target configuration, a least-squares approach is used to minimize the error between $\boldsymbol{x}_*$ and $\boldsymbol{x}_{\mathrm{g}}$. This error is defined as the squared normalized magnitude (Euclidean norm) of the difference between both vectors and is minimized with respect to $\boldsymbol{w}$ as:

$$\min_{\boldsymbol{w}} \sqrt{(\boldsymbol{x}_* - \boldsymbol{x}_{\mathrm{g}})^{\mathrm{T}} (\boldsymbol{x}_* - \boldsymbol{x}_{\mathrm{g}})}. \tag{2.15}$$

line-point

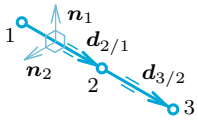

$$\boldsymbol{c} = \begin{pmatrix} \boldsymbol{n}_1 \cdot \boldsymbol{d}_{3/2} \\ \boldsymbol{n}_2 \cdot \boldsymbol{d}_{3/2} \end{pmatrix}$$

Figure 2.7: (Caption on next page.)

Figure 2.7: Constraining a point to lie on a line by using two vectors that are orthogonal to the line. This method of constraining works numerically, but is not robust algebraically.

To solve this problem, we substitute (2.14) into (2.15). The minimum error can then be found by evaluating the term inside the square root:

$$\min_{\boldsymbol{w}} \left((\mathbf{U}\boldsymbol{w} + \boldsymbol{x} - \boldsymbol{x}_\mathrm{g})^\mathrm{T} (\mathbf{U}\boldsymbol{w} + \boldsymbol{x} - \boldsymbol{x}_\mathrm{g}) \right). \tag{2.16}$$

We take the derivative, which is zero at the minimum,

$$\frac{\mathrm{d}}{\mathrm{d}\boldsymbol{w}} \left((\mathbf{U}\boldsymbol{w} + \boldsymbol{x} - \boldsymbol{x}_\mathrm{g})^\mathrm{T} (\mathbf{U}\boldsymbol{w} + \boldsymbol{x} - \boldsymbol{x}_\mathrm{g}) \right) = \tag{2.17}$$

$$2\mathbf{U}^\mathrm{T} (\mathbf{U}\boldsymbol{w} + \boldsymbol{x} - \boldsymbol{x}_\mathrm{g}) = \mathbf{0} \tag{2.18}$$

and solve for $\boldsymbol{w}$:

$$\boldsymbol{w} = \left(\mathbf{U}^\mathrm{T}\mathbf{U}\right)^{-1} \mathbf{U}^\mathrm{T} (\boldsymbol{x}_\mathrm{g} - \boldsymbol{x}), \tag{2.19}$$

where $\mathbf{U}^+ = \left(\mathbf{U}^\mathrm{T}\mathbf{U}\right)^{-1} \mathbf{U}^\mathrm{T}$ is the left pseudo-inverse.

Constraint satisfaction

The violations in the constraints are corrected by applying the Gauss-Newton method. We want to correct the configuration $\boldsymbol{q}_* = (\boldsymbol{x}_*^\mathrm{T}, \boldsymbol{\lambda}_*^\mathrm{T})^\mathrm{T}$ in such a way that the configuration does not violate the constraints. The configuration is, therefore, linearized around $\boldsymbol{q}_*$ to move it closer to a configuration that fulfills the constraints,

$$\boldsymbol{q} = \boldsymbol{q}_* + \boldsymbol{\delta}, \tag{2.20}$$

where $\boldsymbol{\delta}$ are small changes or corrections that make sure the constraints are satisfied up to any arbitrary residual. To move to the closest of these configurations (according to the least-square analysis), the 2-norm between $\boldsymbol{q}$ and $\boldsymbol{q}_*$ is minimized as:

$$\min_{(\boldsymbol{q}_* - \boldsymbol{q})} \sqrt{(\boldsymbol{q}_* - \boldsymbol{q})^\mathrm{T} (\boldsymbol{q}_* - \boldsymbol{q})}, \tag{2.21}$$

which should hold for all $\boldsymbol{q}$ that fulfil the constraints in the form:

$$\boldsymbol{c}(\boldsymbol{q}) = \mathbf{0}. \tag{2.22}$$

We solve this equation by first substituting (2.20) into (2.21) and (2.22) and obtaining two equations. The term under the square root of (2.21) after substitution gives

$$\min_{\boldsymbol{\delta}} \left(\boldsymbol{\delta}^{\mathrm{T}} \boldsymbol{\delta} \right). \tag{2.23}$$

The minimum is then obtained by setting the derivative of this term equal to zero:

$$\frac{\mathrm{d}}{\mathrm{d}\boldsymbol{\delta}} \left(\boldsymbol{\delta}^{\mathrm{T}} \boldsymbol{\delta} \right) = \tag{2.24}$$

$$2\boldsymbol{\delta} = \mathbf{0}. \tag{2.25}$$

The second equation is found by substitution into (2.22) with a first-order Taylor series linear approximation as:

$$\boldsymbol{c}(\boldsymbol{q}_*) + \mathbf{J}(\boldsymbol{q}_*)\boldsymbol{\delta} = \mathbf{0}, \tag{2.26}$$

where $\mathbf{J}$ is the Jacobian of the constraints. The linear optimization problem of (2.25) and (2.26) can be solved simultaneously by using Lagrange multipliers:

$$\begin{pmatrix} \mathbf{I} & \mathbf{J}^{\mathrm{T}} \\ \mathbf{J} & \mathbf{0} \end{pmatrix} \begin{pmatrix} \boldsymbol{\delta} \\ \boldsymbol{\mu} \end{pmatrix} = \begin{pmatrix} \mathbf{0} \\ -\boldsymbol{c} \end{pmatrix}, \tag{2.27}$$

where $\mathbf{I}$ is the identity matrix and $\boldsymbol{\mu}$ are the Lagrange multipliers. From the first row, we find

$$\boldsymbol{\delta} = -\mathbf{J}^{\mathrm{T}} \boldsymbol{\mu}. \tag{2.28}$$

Substituting into the second row gives $\boldsymbol{\mu} = (\mathbf{J}\mathbf{J}^{\mathrm{T}})^{-1}\boldsymbol{c}$. Plugging this last result into (2.28) results in the correction values:

$$\boldsymbol{\delta} = -\mathbf{J}^{\mathrm{T}} \left(\mathbf{J}\mathbf{J}^{\mathrm{T}} \right)^{-1} \boldsymbol{c}, \tag{2.29}$$

where $\mathbf{J}^{+} = \mathbf{J}^{\mathrm{T}} \left(\mathbf{J}\mathbf{J}^{\mathrm{T}} \right)^{-1}$ is the right pseudo-inverse.

2.6.2 Technical details of the experiments

The proposed simulation approach is fully scalable and is not affected by absolute dimensions, only relative ones. Therefore, a lot of freedom exists in how the actual structures are created. Nevertheless, to perform the experiments, we needed to make specific designs of the modules (Figure 2.8)

and related objects. Here, we present some more details regarding the construction and design of the experiments, since a physical model requires part dimensions and other design features.

The structures themselves are built up with a modular approach where different components can be combined to create the structure (Figure 2.8a–j). In this case, we chose for the spheres to have a radius of 10 mm. The parts that need to deform more to provide snapping, such as the clamps, are designed to enable this behavior and are printed from a tougher material. The structure used for the validation experiment has two bodies connected by a link. The bodies were created as a tailor-made triangular skeleton, placing the sphere centers at 60 mm from the body center. The link between both bodies ensures that both linked spheres are at a distance of 60 mm from each other.

We must consider the modular structure's nature when designing the target substrate shapes. The spheres have a finite dimension in the modular system. Therefore, if the center of the spheres is seen as the node location, we need to consider that dimension. The created target shapes (Figure 2.8k–m) have dimensions that take this into account, as shown in Table 2.1. This dimensioning ensures that the sphere centers can reach the target locations specified for the corresponding nodes in our analysis of kinematic structures. Furthermore, these shape substrates are manufactured with material extrusion (MEX-TRB/P/PLA [51]; Ultimaker 2+, Ultimaker, The Netherlands; green filament) and have holes to allow 3D scanning of the structure in it by not obscuring it, while still allowing the spheres to touch the substrate in the desired locations. An additional benefit is that the use of material is minimized. One can manually put the structures on the substrates to contact the shapes at those locations. As a reminder, only the end shape is considered in these experiments, so the path that the spheres move towards the shape is irrelevant in this study and does not need to be considered in the substrate designs. Notches are added to the substrates asymmetrically, to provide a cosmetic aid for the 3D-scan postprocessing, where pictures from different angles must be aligned.

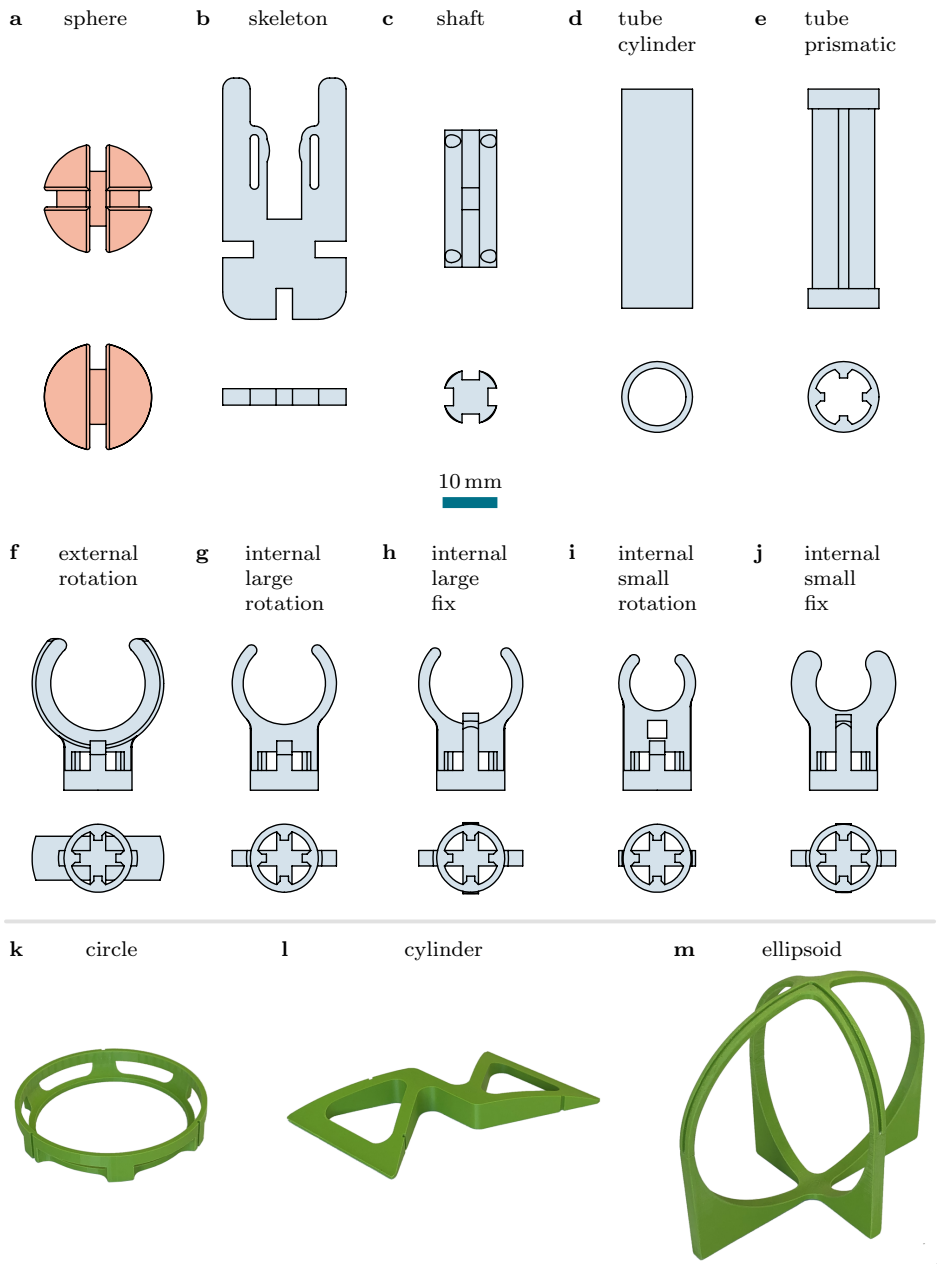

Figure 2.8: (Caption on next page.)

Figure 2.8: Technical designs of all the modular system parts and pictures of the substrate shapes. Two projections each with uniform scale. a) Slotted spheres representing the nodes. b) Skeleton pieces for creating bodies. c) Slotted shafts used as connecting elements. d)–e) Tubular parts to create translational joints. f)–j) Clamps for creating different rotating or fixed joints. k)–m) The 3D-printed substrate shapes.

Table 2.1: The target shape dimensions used for the simulations and experiments.

	simulation	experiment (mm)
circle		
radius	60.00	70.00
cylinder		
radius	192.26	183.00
chord	175.00	165.93
width	163.90	163.90
ellipsoid		
semi-axis 1	47.43	57.43
semi-axis 2	67.08	77.08
semi-axis 3	84.85	94.85

2.6.3 Limiting the range of motion

Without adding more elements to the current constraint descriptions, we can already apply limits to the ranges of motion of various nodes. In order to apply a limit to the of range of motion between two nodes, we can use a phantom system (Figure 2.9). In this approach, an extra node is introduced that does not represent a physical point on the structure. This node is constrained to either one of the other nodes through distance constraints. This has the effect that both nodes can move with respect to each other within a range of distance. The lower and upper bounds of the range are determined by both lengths of the phantom constraints. With reference to the numbering in Figure 2.9, the lengths for $\boldsymbol{d}_{2/1}$ and $\boldsymbol{d}_{3/2}$ are found by solving the following equations:

$$ {}^{-}d_{3/1} = \left|\boldsymbol{d}_{2/1}\right| - \left|\boldsymbol{d}_{3/2}\right|, \quad {}^{+}d_{3/1} = \left|\boldsymbol{d}_{2/1}\right| + \left|\boldsymbol{d}_{3/2}\right|, \tag{2.30} $$

where ${}^{-}d_{3/1}$ is the desired lower distance limit and ${}^{+}d_{3/1}$ is the desired upper distance limit. Note that this distance range limitation is not a constraint itself.

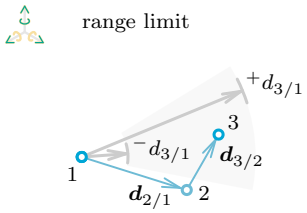

$$\boldsymbol{c} = \begin{pmatrix} \boldsymbol{d}_{2/1} \cdot \boldsymbol{d}_{2/1} - d_1 \\ \boldsymbol{d}_{3/2} \cdot \boldsymbol{d}_{3/2} - d_2 \end{pmatrix}$$

Figure 2.9: (Caption on next page.)

Figure 2.9: Illustration of limiting the range of the distance between two nodes. The nodes 1 and 3 are confined to move within a certain distance, from ${}^{-}d_{3/1}$ to ${}^{+}d_{3/1}$, from each other. This is done by constraining phantom node 2 to them via constraints $\boldsymbol{c}$.

2.6.4 Node representation

Selecting the location and number of nodes used to represent a structure can affect the qualitative and quantitative outcomes of its shape-morphing capabilities. In order to illustrate this point, further simulations were performed with modifications in their nodal representation. In Figure 2.10, these results are presented for one structure morphing into two distinct shapes. The number of nodes was increased across different scenarios. In some cases, the selection of the nodes that aim at the target shape were changed too.

The results of this parametric study showed that, all other things being equal, more nodes generally result in a longer calculation time, t, as well as more required steps, s (Figure 2.10a). However, the average normalized distance error of the nodes from the target, $\mathcal{E}$, and the normalized shape factor, $\mathcal{S}$, which represent the average node distance from the structure's centroid, do not necessarily change among cases. These two quantities are dependent on the target shape and the placement of the nodes within the structure. In this example, all the nodes were defined within a single plane, and the shape was curved in one direction. Employing three nodes per body minimized the surface error, similar to a three-legged chair maintaining three contact points even on curved surfaces. Adding more in-plane nodes to the initial three-node layout with the same curved target shape increased the average error per node. This average error was slightly reduced by further incorporation of nodes within the boundaries delineated by the initial three nodes, as these nodes on average drew nearer to the target shape. Moreover, due to a larger proportion of nodes being placed closer to the centroid of the structure, the shape factor slightly decreased.

While the mild curvature in the previous example resulted in increased error, the next example demonstrates that the quantitative outcome is case-dependent, and can be addressed appropriately. In the case of an ellipsoidal shape (Figure 2.10b), incorporating additional in-plane nodes adversely affected the shape's fit due to the inability of in-plane nodes to properly approach the highly curved surface. However, it may not be

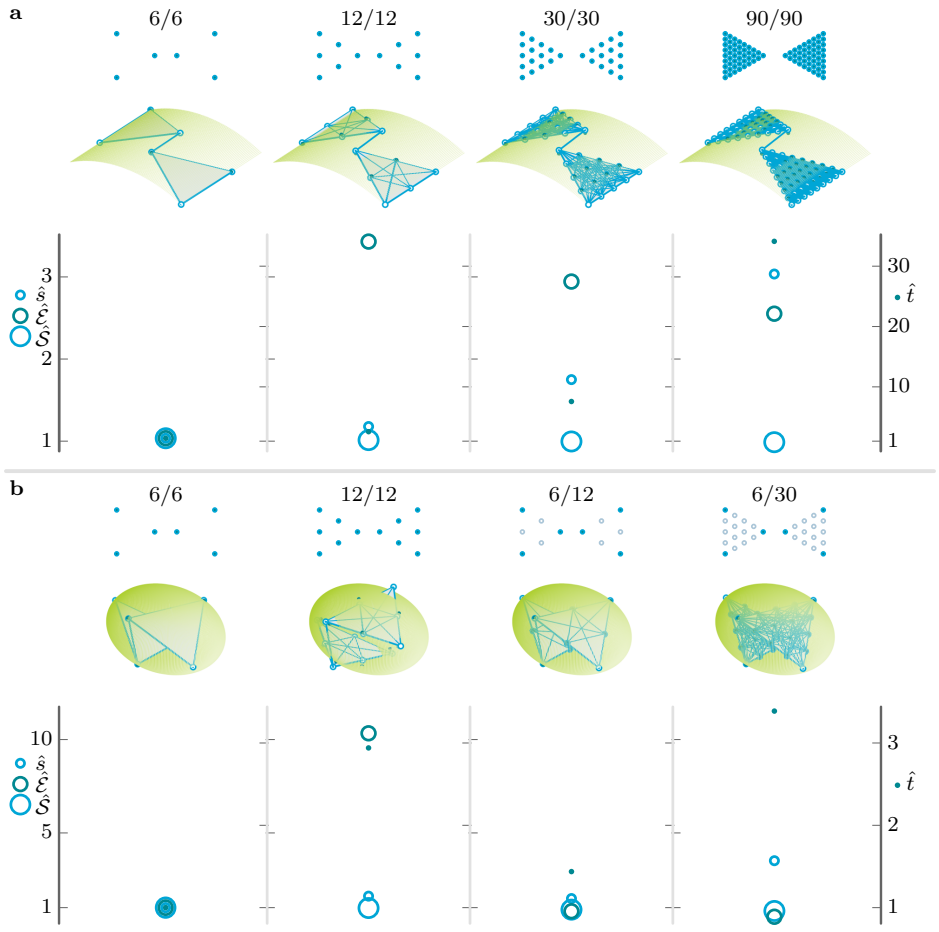

Figure 2.10: (Caption on next page.)

Figure 2.10: The effects of the number of nodes on simulation output variables for a structure transforming into different shapes. The shown variables are the number of steps, s, error metric, $\mathcal{E}$, shape metric, $\mathcal{S}$, and simulation time, t. Both the total number of nodes for each case and the number and location of the nodes translating to the target shape are depicted. For each simulation involving a specific number of nodes, the time is calculated as the mean of the computing times of 20 simulations. a) The structure with a cylindrically curved plate as the target shape. For these four cases the normalized values were calculated as $\hat{s} = s/7$, $\hat{\mathcal{E}} = \mathcal{E}/0.00734$, $\hat{\mathcal{S}} = \mathcal{S}/0.825$, $\hat{t} = t/(0.268\,\mathrm{s})$. b) The structure with a varying number of nodes and different selections of nodes moving towards the ellipsoidal target. For these four cases, the normalized values were calculated as $\hat{s} = s/39$, $\hat{\mathcal{E}} = \mathcal{E}/0.00693$, $\hat{\mathcal{S}} = \mathcal{S}/0.629$ and $\hat{t} = t/(6.28\,\mathrm{s})$.

necessary to direct all the nodes towards the surface. In such instances, one can selectively move certain key nodes towards the surface (*e.g.*, the corners of the body), decreasing the error values to values similar to the initial ones.

In summary, the quantity and placement of nodes as well as the selection of the targeting nodes determines the quantitative performance of the shape-matching method presented in this study. These aspects must be meticulously considered when using the approach proposed here. Nevertheless, when node patterns are identical, comparable qualitative morphing performances of structures can be achieved between different scenarios.

Acknowledgments

P.H.dJ. would like to thank Judith Cueto Fernandez for the support in the early stage shaping of the text and the virtual sculpting of the undefined 3D “blend” (Figure 2.5c).

Chapter 3

Locking Lattice

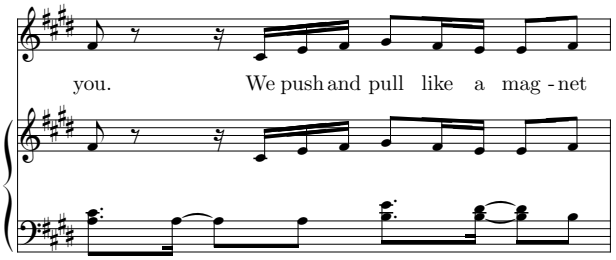

Ed Sheeran, Steve Mac and John McDaid,
second chorus bar from *Shape of You* (2017)

Abstract

Shape morphing is the ability of objects to adapt to different shapes and reduce stress concentrations through increased contact area. This is a common trait of natural and engineered objects and has several applications in, among others, soft robotics and orthopedic implants. Shape morphing is achieved through flexible materials or rigid components with either kinematic or compliant joints. An additional step, namely shape locking, is needed for sustained load support. Activation of a locking mechanism can be done with any energy, among which magnetism is one. Here, we

Modified from [15]

present the implementation of a magnetic locking mechanism for kinematically deformable metamaterial structures that maintain shape and support loads upon locking. The structure consists of 3D printed rigid magnetic and non-magnetic components connected by hinges. We created several prototypes of the proposed designs using two additive manufacturing methods (*i.e.*, material extrusion and multi-material jetting) and demonstrated its application in a closed-loop grid for arbitrary shapes. Moreover, we characterized the performance of the prototypes using mechanical tests and multibody kinematic system simulations. This work highlights the viability of the locking concept and provides design considerations for future applications. Further improvement and optimizations are needed for increased efficiency and effectiveness.

Keywords

shape morphing; locking mechanism; kinematic fixation; magnetism; 3D printing.

3.1 Introduction

Shape-morphing is a crucial aspect of load support in devices working on the basis of contact, such as orthopedic implants [27, 57], exosuits [58], and (soft) robotic grippers [59–62]. That is because shape morphing allows such devices to adapt to different shapes, thereby distributing loads more efficiently through increased contact area and attenuated stress concentrations. In fact, shape-morphing can be also observed in nature (*e.g.*, in human hands and gecko toes). Shape morphing in those structures and systems can be achieved with flexible materials or through the integration of rigid components connected by kinematic or compliant joints [13]. In some cases, shape morphing should be followed by shape locking to ensure the attained shape can be preserved for further use. To achieve shape locking, a shape locking mechanism may need to be implemented in the design of the device (Figure 3.1).

The locking of shape morphing structures is also essential for sustained load support [63]. While shape morphing requires the structure to exhibit a high degree of deformability, a locked structure must retain its shape

and provide sustained support while exhibiting a significant increase in its overall stiffness. Clay is an example of a material that demonstrates the ideal characteristics of both shape morphing and shape locking. In its moldable state, clay has low resistance to deformation. Once fired, however, its resistance to deformation significantly increases. Another example of locking can be seen in the human hand, where multiple muscles interact with each other to lock the hand into a specific shape. In tandem, these structural elements enable the adaptation of the shape morphing structure and the application of gripping force to an object.

The primary challenge when combining shape morphing with shape locking in one single mechanism lies in the fact that these two steps often have contradictory design requirements. For example, while many degrees of freedom (DoF) are essential for shape morphing, it complicates locking a structure in an acquired shape. In this context, it is important to realize that while shape morphing and shape locking are interdependent processes, the mechanism that induces the shape adaptation often also locks the structure in a particular configuration. That is partially because having two separate mechanisms for shape morphing and shape locking can highly complicate the design and fabrication of such structures. Another route to resolve the contradictory design requirements is implementing separate working principles for shape morphing and shape locking in the same structure. The activation energy required for morphing and locking can take various forms, including mechanical [63], chemical [64], thermal [65–72], pneumatic [73], or (electro)magnetic [74–82]. Any combinations of these mechanisms can be utilized for shape morphing and shape locking. For instance, we can use light to alter the chemical composition, heat to control a mechanical system [83], magnetism to both heat and deform a structure [84–86], or mechanically block a joint [87]. The activation energy is crucial for achieving the desired shape morphing properties [61, 62, 75], such as locality [65], reversibility [80, 88] and continuity [89].

In this work, we examine the shape morphing and locking of structures in a kinematic metamaterial concept, also referred to as the “metallic clay” [13]. Kinematic metamaterials are a type of metamaterial [90, 91] composed of rigid components connected by movable joints and are capable of kinematic deformations. The shape morphing and locking of these structures can be independently controlled, offering a wide range of potential

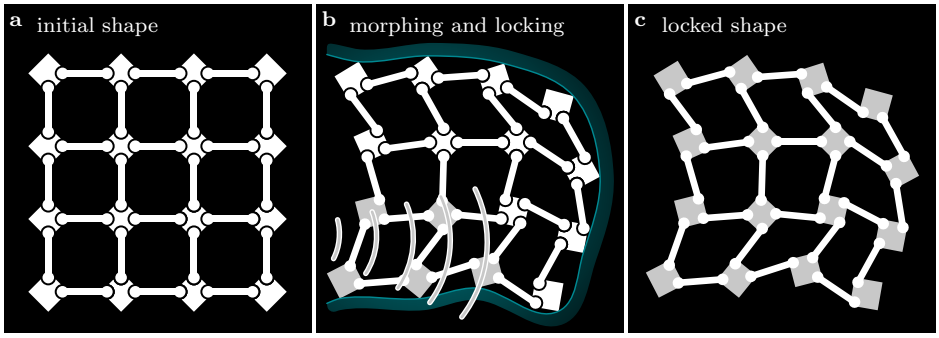

Figure 3.1: (Caption on next page.)

Figure 3.1: An illustration of the shape morphing and shape locking principles using an in-plane deforming structure. a) The structure is equipped with multiple hinges that provide multiple DoF. b) The structure is transformed into a desired shape and a stimulus is applied to lock the hinges in place. c) The locked structure retains its shape even after being removed from the target shape.

applications. To lock the structure, the joints need to be restricted in their motion, which can be accomplished by enhancing their stiffness through deployment and multi-stability [92, 93]. When the stiffness is significantly increased, one may consider the structure to have been locked. The complete elimination of the DoF of a joint or the entire system is, however, only achieved through a locking process [89]. The DoF determine the number of possible transforms that an object can undergo. In the case of kinematically deformable structures, there is a large but finite number of DoF. To fully lock the shape of such a structure, all these DoF must be eliminated, requiring both a locking principle and an activation method.

The aim of this study is to explore the fundamentals of locking of kinematically deformable structures [13] and to propose an approach based on magnetic force for contactless accomplishment of this task in an otherwise purely mechanical structure. We focus on an in-plane deforming design that has multiple DoF and can be transformed into various shapes through mechanical manipulation (Figure 3.1). We designed and implemented a locking mechanism that can be triggered to lock the shape in place. A multibody kinematic system approach was used and expanded upon to numerically simulate the morphing behaviour of the system upon locking individual elements. Eventually, the conceptual design is 3D printed using two different additive manufacturing (AM) techniques and is evaluated using mechanical tests. The unit cells of these structures are designed such that they can be locked individually through mechanical activation through magnetic forces. This study, therefore, aims at providing: i) an in-depth understanding of the challenges in locking shape-morphing, kinematically-deformable structures, and ii) a tangible demonstration of a magnetically-activated locking mechanism that can be utilized to control the shape of a kinematically-deformable structure. Although the interlocking latch mechanism is a classic type of mechanism often used in mechanical systems, the methodology of its implementation in this study presents valuable new insights.

3.2 Materials and methods

To investigate the challenges associated with the locking of shape morphing mechanisms, we examined an existing in-plane deforming kinematic design [13] and modified it to incorporate a reversible, magnetically-activated locking mechanism. The design consisted of a network of rigid bodies and hinged struts, which provided the structure with multiple DoF. These DoF are selectively locked in groups of four at the scale of individual bodies by applying a magnetic field. The locking can be reversed to an unlocked state by redirecting the magnetic field. By using magnetism as the activation method, the internal locking mechanism can be triggered from outside of the structure without the need for physical contact with the moving parts. The shape-morphing and locking mechanism were implemented in two distinct designs: a modular design and a semi-non-assembly design.

3.2.1 Design and working principles

All the designs shared the same principle of locking as well as the same key dimensions. A translating ring is moved by magnetism to interlock with the connected struts and constrain their rotation. Depending on the type of application, one can introduce a "snapping" mechanism to keep the lock in place after the magnetic stimulus is removed. With this principle, two distinct designs were created: a modular design and a semi-non-assembly design.

The first (colored primarily white) design of the proposed structure features modular components that can be connected via struts for the ease of assembly and experimentation (Figure 3.2a). The parts were manufactured using MEX-TRB/P/PLA [51], as detailed in Table 3.1. Each component is equipped with four revolute joints, which are locked using a central ring made of an iron composite material that is attracted to magnetism (Figure 3.2b). The ring can be positioned and snapped into place by using a magnetic field. This design features simple components that can be easily assembled after printing due to the lack of need for overhanging angles. Therefore, the modular design allows for flexibility in adding or removing components and experimenting with them (Supplementary Video 1 of [15]) such that different configurations can be explored

(Figure 3.2c). This leads to a vast number of design possibilities, each of which can be transformed into multiple shapes. The key dimensions of the system, for both the modular design and its developments, are illustrated in Figure 3.2d.

Table 3.1: The materials and manufacturing techniques used for designing components. The table provides information regarding the properties and limitations of each component, aiding in the determination of its suitability for the intended application.

	grey (ring)	white	transparent
material	Composite Iron PLA[a]	PLA white[b]	VeroClear[c]
method	MEX-TRB/P	MEX-TRB/P	MJT-UV/P
printer	Ultimaker 2+[b]	Ultimaker 2+[b]	PolyJet, ObjetJ735[c]
layer height	0.060 mm	0.060 mm	0.027 mm
nozzle size	0.250 mm	0.250 mm	-

[a]Proto-pasta, ProtoPlant Inc., USA, [b]Ultimaker BV, The Netherlands, [c]Stratasys Ltd., USA.

Given that magnetic fields generally have limited strength and reach and to ensure the effective operation of the snapping mechanism, it is important to minimize the required force F applied by the magnetic field on the locking ring. This force is dependent on various factors, including the properties of the magnet, the properties of the ring material, and the friction within the system. The snapping mechanism should keep the lock in place even after the removal of the magnetic stimulus and allow for the release of the lock upon the application of another activation stimulus. To achieve this, it is important to consider the potential for the magnetic field to pull the ring through the snap in two directions. We analyzed the repeatability of the process through the calculation of the decay $\hat{\mathcal{D}}$ associated with the lock and release cycles. This decay was calculated for both the locking and releasing processes and was defined as $\hat{\mathcal{D}} = (F_1 - F_2)/F_1$, where the subscripts indicate the cycle. As many parameters interact with each other, an experimental approach was used to evaluate the different designs in terms of the performance of their snapping mechanism. Four different designs (Figure 3.3a) were fabricated and were subjected to uniform experimentation. All designs rely on compliant deformation of the parts to snap into place. The test samples comprised simplified versions of the design, with the removal of the redundant components. As shown in Table 3.1, the locking ring was printed in grey polymer with thermally

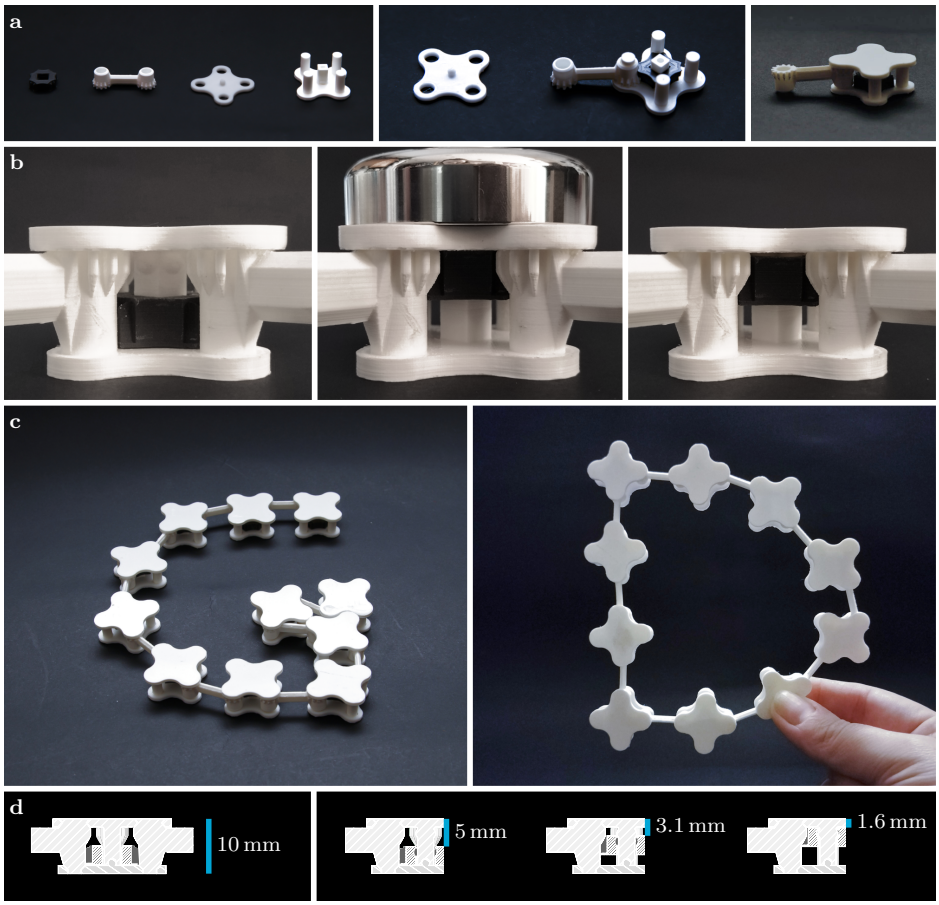

Figure 3.2: (Caption on next page.)

Figure 3.2: An illustration of the design and functionality of the magnetic locking of a shape morphing mechanism. a) The 3D-printed components included the iron-polylactic acid (PLA) composite locking ring (grey), connecting struts (white PLA), and body pieces (white PLA). The ring and struts were placed on one of the body pieces. The full assembly with one unit of each component has a single transforming DoF (excluding the ring's translation). b) In the unlocked state, the ring is down and does not engage with the teeth on the struts, allowing them to rotate. The placement of a magnet on top shifts the ring upward and locks the struts in place, removing the DoF. The design presented here ensures that the ring remains "snapped" in place and remains locked when the magnet is removed. c) Combining unit cells creates a structure that can be locked in a desired shape. We demonstrate an open-loop and a closed-loop structure. d) The cross-sections of the main elements for a non-assembly development of the design with the dimension of all the implementations at hand. On the left, a basic element is shown with a locking ring but without a snapping mechanism for the secure locking of the ring. On the right, a design is presented with a snapping mechanism, showing the distances from the top of the element to the magnetic ring in different stages of the locking process.

bonded material extrusion of polymer (MEX-TRB/P/PLA [51]) and the other part was with material jetting of polymer with UV curing (MJT-UV/P [51]). The specimens featured enlarged, flat heads with a through hole for easy attachment to the pin grips of a testing machine (Figure 3.3b–c). A Lloyd LR5K mechanical testing machine was employed to lock and release the specimens, and the applied force was measured using a 100 N load cell (Figure 3.3d). Quasi-static uniaxial compression and tensile tests were conducted under displacement control at a rate of 1 mm/min until locking and releasing were achieved for each mechanism. The machine recorded the force F, displacement δ, and time (with an average sampling rate of 5 Hz) for each test. Three specimens were evaluated for each design, undergoing two cycles of locking and releasing.

The initial unit cell design enabled the formation of a larger network through structured organization in a grid. This resulted in an in-plane shape-morphing structure that could be securely locked. The unit cell design also facilitated the customization of the number of bodies in the network, allowing for close conformity to the contours of a desired shape by adjusting the position of the edge bodies. Furthermore, the internal bodies provided support to maintain the structure's shape and resist any external loads or stress. Therewith, the network design provided versatility and adaptability to different shapes, while ensuring the structural integrity and stability of the structure.

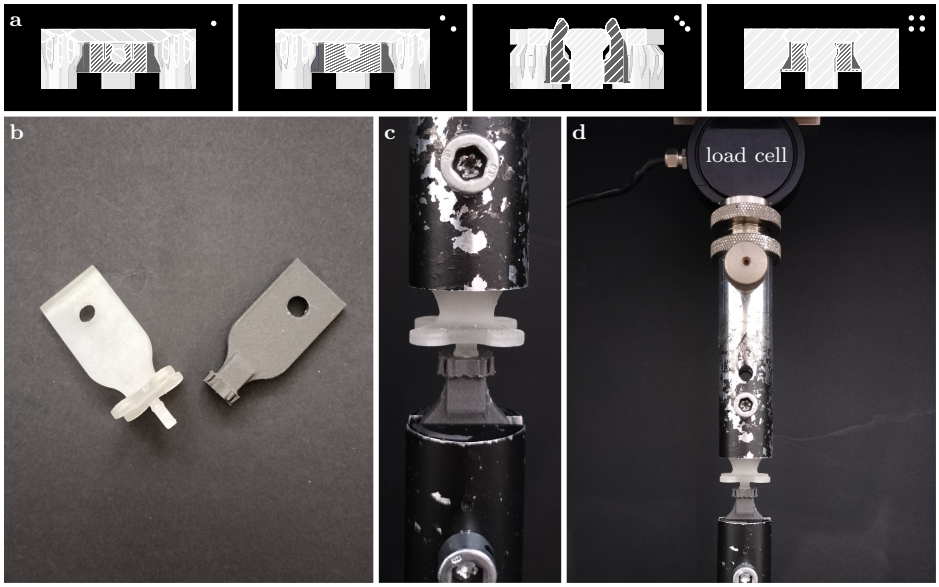

Figure 3.3: (Caption on next page.)

Figure 3.3: The evaluation of the snapping mechanisms using a mechanical test setup to determine the required forces of the mechanism. a) Four examples, 1 to 4, of the different designs of the snapping mechanism to secure the lock in the locked position, after being pulled by a magnetic field. b) One of the four designs (specimen "4") with the notch on the transparent part and the locking ring on the grey part. c) The specimen was initialized for the test with either part placed in one of the mounts. The locking ring was placed in the immobile lower mount, while the transparent part was placed in the moving upper mount. d) The upper part moved down for locking and up for release, as the load cell measured the applied force. The load cell was connected to the upper mount and provided quantifiable data regarding the design's performance by measuring the required mechanism locking force.

The subsequent (primarily transparent) designs that incorporate the unit cells in a grid were variations of the modular design, but they were manufactured using a different approach. The design of these specimens is presented in Figure 3.2d. The grey iron composite ring was manufactured using MEX-TRB/P/PLA [51], whereas the transparent components were printed using MJT-UV/P [51] (Table 3.1). The MJT-UV/P [51] is a 3D printing process in which multiple streams of UV-curable polymers are selectively deposited at each spatial location, and has the potential to produce the entire structure with a grid of unit cells in a single step, potentially resulting in a non-assembly design [94]. The precise tolerances this printing also enabled the creation of functioning revolute joints, given that the design accounted for the limitations of the printing process. For example, with an overhanging angle $> 45°$ (measured with respect to the horizontal plane), an integrated joint can be printed without a need for an assembly step. The non-assembly design has advantages in terms of structural integrity and reduced manufacturing time. However, in the case of the present design, the components that hold the locking ring require assembly, since the locking ring must be made of a different material. Consequently, the main grid along with the revolute joints were printed without the "caps" on the bodies. The separately printed locking rings (MEX-TRB/P/PLA [51]) were then inserted into the bodies after which they were sealed with the caps. This approach provides opportunities to experiment with different morphing and locking mechanisms.

To further explore the versatility of the basic design, the original network structure was modified to enable morphing toward shapes that extend beyond 2D. Multiple layers of the in-plane deforming structure were combined by changing only one unit cell. The layers were connected only

at their center which allowed the bodies on the edges to move independently among layers. Each layer could, therefore, be deformed and locked independently of other layers. The morphing process involved shaping the first layer into a target shape and locking it in place. Next, a connecting piece was used to stack the second layer on top of the first one, which in turn was shaped and locked into the target shape at that height. This process was repeated until the desired 3D shape was being approached through a large enough number of stacked layers.

3.2.2 Simulation of the locking behaviour

The complexity and interconnections of a network configuration make an analysis of the motions it can undergo non-trivial. One could determine the number of DoF through a combination of physical reasoning and calculations that take into account the number of independent constraints [95]. In our previous study [14] (Chapter 2), we developed a multibody kinematic approach aimed at analyzing the shape-morphing behaviour of mechanical metamaterials. Using this approach, the structure can be discritized into a series of nodes (or joints), bodies and links. By modifying the DoF between each node through application of independent constraints, the motion of individual elements relative to one another can be analyzed. This methodology serves as a predictive tool for the final shape of the structure.

Here, we have further extended this model to include toggling the fixation of DoF. This addition allows for the complete locking of the structure once it has morphed into a desired shape. Our analysis identified the minimum number of active elements and their optimal distribution required to fully lock the deformed structure.

The structure has case-specific traits to which we apply the general morphing algorithm. We assumed that all the bodies in the structure were composed of four nodes, representing the joints (or hinges) between the bodies and the links (Figure 3.4a). These nodes were algebraically constrained to one another through constraints $\boldsymbol{c}$ with vectors $\boldsymbol{d}$ and constants d, facilitating either relative motion or relative fixation. We constrained the structure's out-of-plane movements, forcing it to deform only within a 2D plane. This construct of nodes and constraints was extended to a larger network; a 2D mesh consisting of 25 unit cells (Figure 3.4b).

Subsequently, the morphing algorithm transforms the structure by repositioning the nodes. All the nodes can translate with respect to a target shape, but the nodes are limited by the constraints in the possible translations they can undergo with respect to each other. The peripheral nodes at the boundaries of the structure were selected to move toward a target shape (Figure 3.4b). The target shape was created to be a dented circle to show that an initial square structure can deform into a circular shape that is not per se symmetrical. Non-peripheral nodes were allowed to move only if necessitated by the new positioning of the boundary nodes. To move the nodes, first all the possible linear motions of the nodes $\mathbf{U}$ were calculated by solving $\mathbf{JU} = \mathbf{0}$, where $\mathbf{J}$ is the Jacobian of the constraints $\boldsymbol{c}$. The morphing process then selects the allowed linear motions and superpositions them on the node locations to translate them towards new coordinates for all the nodes $\boldsymbol{x}_*$ that resembles the target shape better by using $\boldsymbol{x}_* = \boldsymbol{x} + \mathbf{U}((\mathbf{U}^{\mathrm{T}}\mathbf{U})^{-1}\mathbf{U}^{\mathrm{T}}(\boldsymbol{x}_{\mathrm{g}} - \boldsymbol{x}))$, where $\boldsymbol{x}$ holds all the current coordinates of the nodes and $\boldsymbol{x}_{\mathrm{g}}$ does the same for the target coordinates of the nodes. Therewith, the distance error $\mathcal{E}$ that represents the Euclidean distance between the deformed structure and the target location of the nodes was minimized by repositioning the nodes. Because the movements of the nodes are linear, the constraints may be violated after a movement. This was corrected with a Gauss-Newton algorithm by applying $\boldsymbol{x} = \boldsymbol{x}_* - \mathbf{J}^{\mathrm{T}}\left(\mathbf{J}\mathbf{J}^{\mathrm{T}}\right)^{-1}\boldsymbol{c}$ until the constraints are satisfied within the chosen tolerance. This whole process required several iterations over multiple steps s to come to a point where $\mathcal{E}$ settles on a constant minimum value. To assess the shape, we introduced a parameter called shape factor $\mathcal{S}$ that measures the average distance of all the nodes from their collective geometrical centroid. This parameter, therefore, provides a quantitative metric for comparing various shapes.

To lock parts of the structure, we developed and applied additional constraints (Figure 3.4c). Specifically, nodes were locked in groups of four per body, thereby imposing four extra constraints and removing four DoF around a body.

Given the presence of multiple bodies and joints in a closed loop, it is unnecessary to lock every joint to fully lock the deformed structure. Our multibody kinematic system approach, involving varying distributions of active elements (Figure 3.4d–i) showed that even with not all the elements

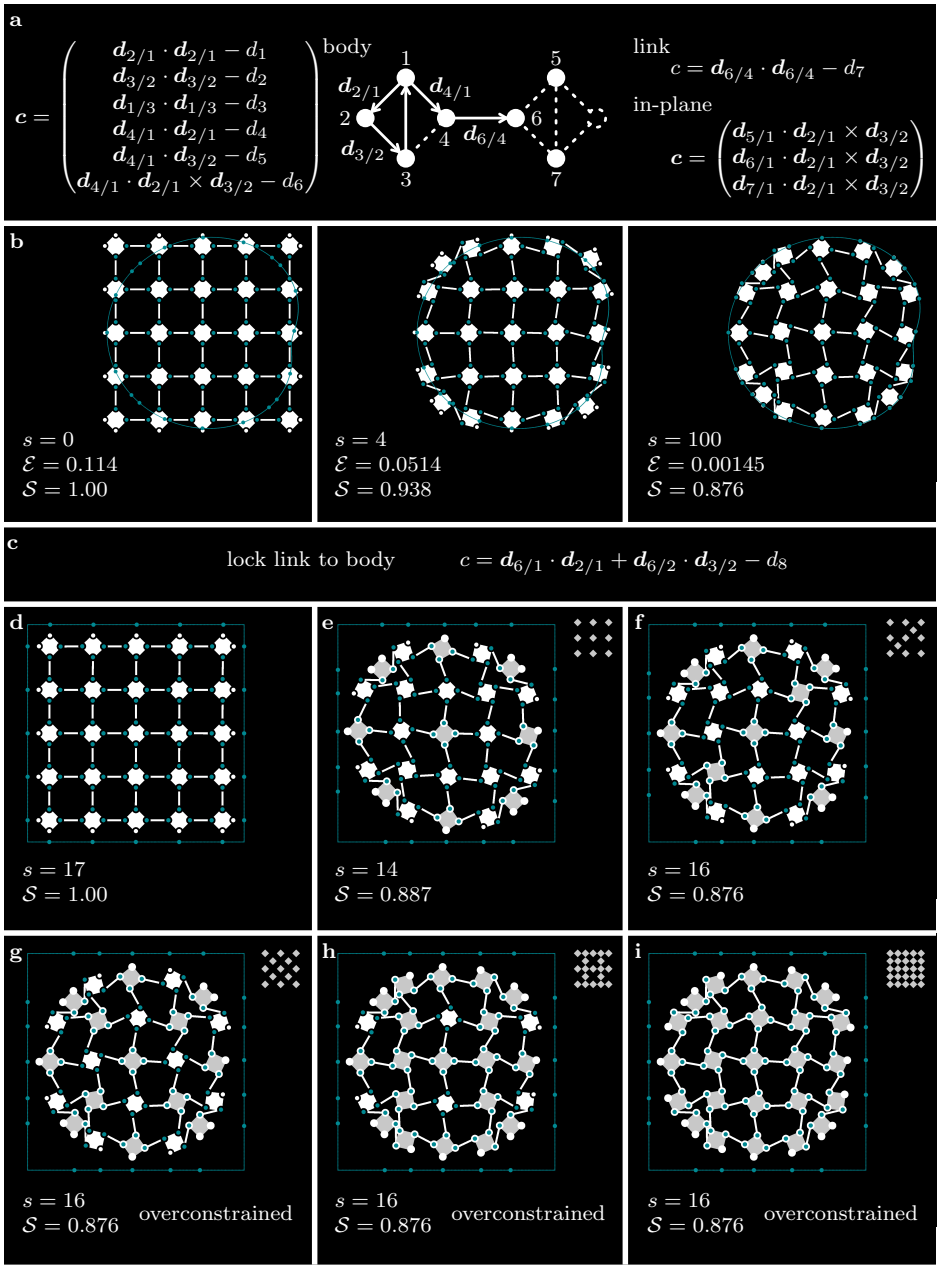

Figure 3.4: (Caption on next page.)

Figure 3.4: Simulation of shape-morphing and -locking using a multibody kinematic system approach and different distributions of actively locked elements. a) Nodes (white circles) and constraints $\boldsymbol{c}$, comprised of vectors $\boldsymbol{d}$ and distances d, define the structure. b) Combining a sufficient number of these nodes and constraints results in a network of rigid bodies (white squares) and rigid links (white lines) connected via hinges. Each simulation proceeds through multiple steps, s, during which the peripheral nodes move toward the desired shape (green line), minimizing the distance error $\mathcal{E}$ between the node and the nearest point (green dot) on the target shape. A shape factor $\mathcal{S}$ was introduced to quantify the current shape relative to its initial shape. The position of nodes at various steps in this process are depicted. c) After the deformation, DoF were removed by applying additional constraints at specific locations. d)–i) Final states in an effort to return the structure to its original state, using a square target shape and altering the distribution of the locked bodies (grey squares). A locked body restricted all its attached links from rotating relative to that specific body which, in certain instances, may result in an over-constrained system.

individually locked, still all DoF can be constrained. The absence of active elements enables the structure to return to its original configuration (Figure 3.4d). However, converting all passive joints into active ones resulted in an overconstrained system, introducing singularities in our model (Figure 3.4i). Hence, our multibody kinematic system approach provides a platform to rationally distribute active elements within the structure, making it possible to fully lock the system without introducing redundant constraints (Figure 3.4f).

3.3 Results and discussion

Physical locking and releasing experiments were performed to gather information on the maximum required snapping forces and the force decay for the four designs of the snapping mechanism (Figure 3.3). The results were used to determine the maximum force required for each locking and releasing cycle and for each specimen of the four designs (Figure 3.5). The collected data was analyzed to compute the average locking and releasing forces for each design, as well as the force decay between cycles. These experiments offered insights into the snapping performance and can inform the optimization of the design for specific applications. The results of the mechanical testing of the four snap designs indicated variability in the maximum required forces and force decays among the different (semi-)cycles for each design. Nevertheless, one design (*i.e.*, design “4”

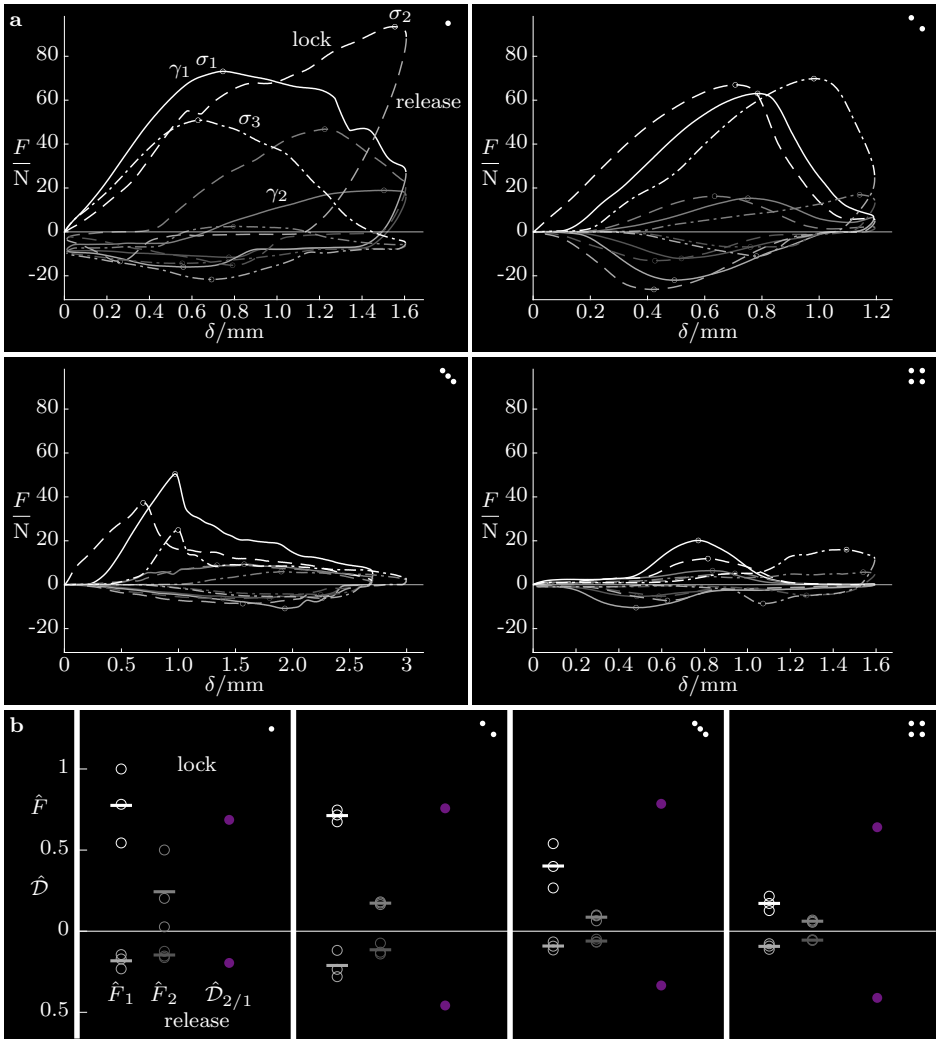

Figure 3.5: (Caption on next page.)

Figure 3.5: The results of the mechanical tests for the snapping mechanisms of designs 1 to 4. a) Force F is plotted versus displacement δ. Three specimens σ were tested for each design and two lock/release cycles γ were performed. The maximum force values during the locking and releasing phases were determined and were plotted as open circles (units and quantities as per [96]). b) The processed results of the mechanical tests on the four designs for both cycles, 1 and 2, of locking and releasing. The normalized maximum locking and releasing forces $\hat{F}$ are indicated by open circles, with the plotted bars representing the mean of these measurements. All the values are normalized with respect to the maximum measured force across all the experiments for comparison purposes. The decays $\hat{\mathcal{D}}$ in the mean required forces between the cycles are presented as purple dots.

where the grey locking ring has a notch that is snapped over a rim on the body) outperformed the others. The forces required for releasing were lower than for locking, which can be attributed to asymmetry in certain designs and mechanism wear after a snap for all designs. This wear sometimes caused cracks to form and parts to break in either the ring or notch components. The force decay was utilized as a measure of wear. Based on this analysis, design "4" was selected for implementation in the structures due to its low force requirements for both locking and releasing and its average force decay. Note that the selection of design "4" is merely an indication of the best snapping design. Actual values are application-dependent and contingent upon various factors, such as dimensions, material properties (including magnetic properties), manufacturing process, locking speed (dynamics), and the strength of the magnetic field. Further optimization is, therefore, necessary to customize the design to the specific needs of any particular application.

The network structures, with their different variations, could be deformed and locked into various shapes, displaying a range of design possibilities. The simplest way to achieve this is by incorporating a locking mechanism in each individual body. By deforming the structure into a target shape and locking it with a magnet, the structure maintained its form (Figure 3.6a–eand (Supplementary Video 2 of [15]). For example, the deformed structure could support and lift a load (Figure 3.6f). By attaching a connecting piece to one of the slightly modified unit cells, multiple independent layers could be stacked on top of each other, thereby offering the possibility to approximate 3D shapes (Figure 3.7a–c). Making selective bodies passive (Figure 3.7d–e) facilitates the possibility to achieve locking by activating a smaller number of cells, while keeping all the unit cells in

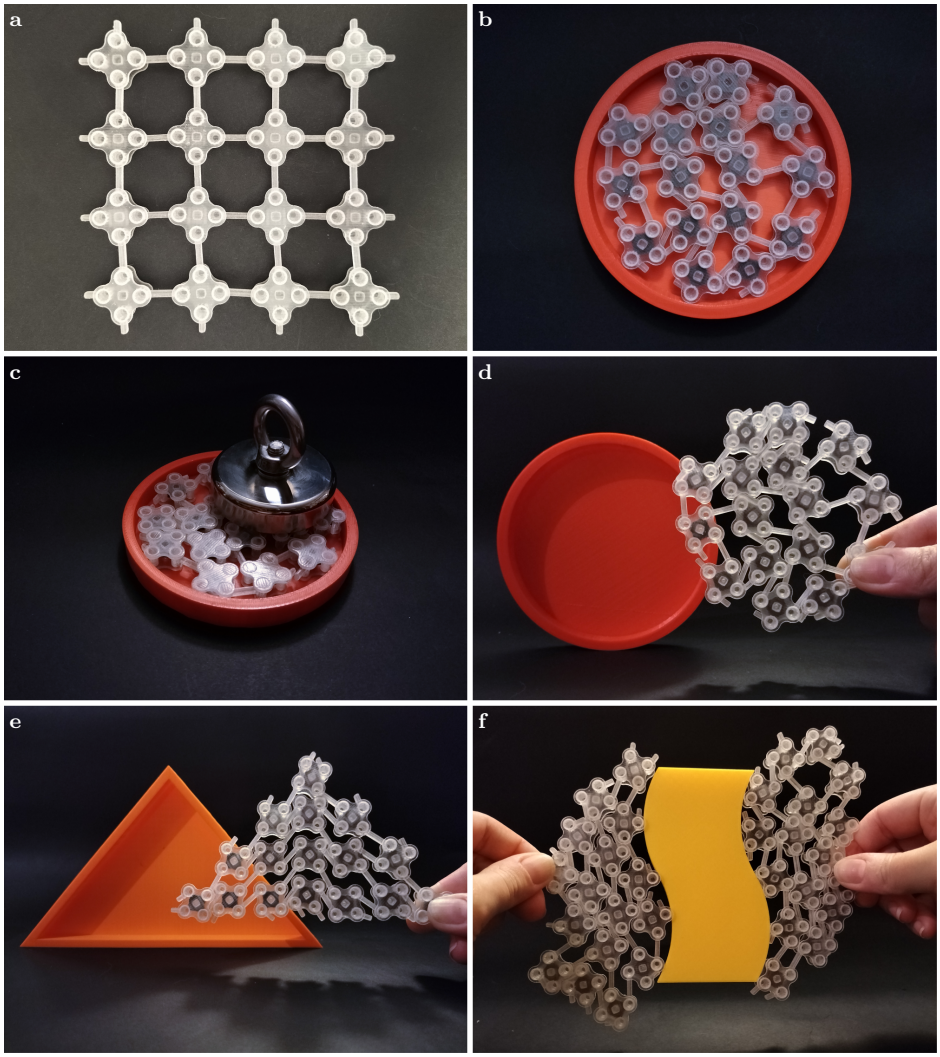

Figure 3.6: (Caption on next page.)

Figure 3.6: The final design of the in-plane shape morphing magnetic locking structures. The structure included ferromagnetic locking rings (MEX-TRB/P/PLA [51]) that are depicted in grey and transparent elements (MJT-UV/P [51]). a) The assembled structure prior to morphing. b) The structure after morphing into a circular shape. c) Shape locking was achieved by a magnetic field. d) The locked structure maintains its acquired shape. e) Different target shapes, such as a triangle, can also be attained. f) A potential application is the grasping of objects.

a fixed position after locking. These passive elements were manufactured as a single piece, eliminating the need for assembly.

Locking mechanisms can be introduced into the design of specific kinematic in-plane deforming structures [13]. The specific locking mechanism introduced in the current study utilizes magnetism to mechanically block the rotation of revolute joints and lock the system in place (Figure 3.2 and Figure 3.6 and Supplementary Video 1-2 of [15]). This enables non-contact shape locking, which are particularly important in such applications as implantable medical devices where shape locking may need to be realized during the surgery in which case the non-contact nature of our proposed technique can both minimize the invasiveness of the surgical procedure and reduce the risk of bacterial infections. While the proposed principle has the potential for various practical applications beyond implantable devices, it also serves as a representative example to study the general features of locking mechanisms in shape morphing structures. We, therefore, investigated morphing and locking mechanisms and studied how the current design fits into those considerations.

3.3.1 Activation energy

Activation mechanisms are necessary for controlling the shape morphing and shape locking capabilities of a structure. These mechanisms can be powered by various energy sources or a combination of them. The choice of the activation method has a significant impact on the performance of the structure. It also determines the reversibility and repeatability of the shape morphing and locking processes, as well as whether they can be applied locally or globally. It is important to note that shape-morphing itself can function as a form of self-locking, as demonstrated by such examples as a spring-tensioned array of kinematic joints pushed into a cavity maintaining its shape by exerting pressure against the object [13].

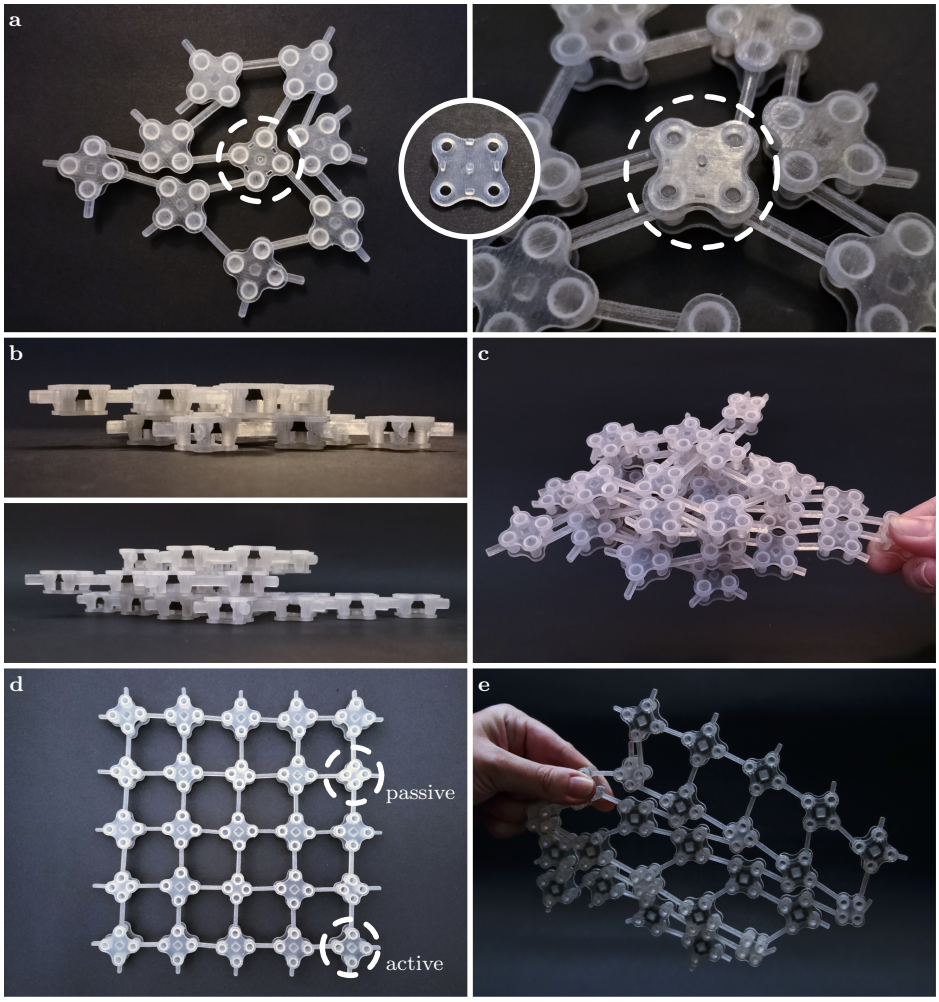

Figure 3.7: (Caption on next page.)

Figure 3.7: Design additions to the basic design. a) Stacking multiple layers enhances the morphing capabilities of the structure, allowing for the approximation of certain types of 3D shapes. An insert piece was attached to the center element of the first layer, which has been morphed and locked. b) A second layer was attached to the first one and underwent similar morphing and locking processes. Additional layers can be added if necessary. c) Each layer can be morphed and locked independently, resulting in a stable fixation. d) Removing redundant constraints after locking by a combination of active locking elements and passive elements that do not possess any locking elements. e) The DoF of the structure can all still be locked.

Here, the locking mechanism is mechanical and uses magnetism for activation (Figure 3.2a–c). This mechanism works by applying a magnetic field perpendicular to the plane of the structure, which pulls a piece into place that blocks the rotation of the joints. Although this design has limitations in its in-plane deforming capabilities, it makes it easier to apply a unidirectional magnetic field to activate the lock. The loads on the structure are solely related to the activation force required to lock the system by means of friction forces. Magnetic locking offers potential advantages, including non-contact activation from a distance and the ability to locally manipulate the shape of the structure [86]. In applications where a strong magnetic field can be used, the design can be implemented as is, for example to fill 2D holes. In other applications, such as (soft) robotics, the lock activation can be performed both onboard the structure by integrating electromagnets that can move the magnetic ring between the lock and release position and remotely through external magnetic fields. The performance of the mechanism depends on the strength and controllability of the magnetic field and the magnetic properties of the part being manipulated.

3.3.2 Reversibility and repeatability

The morphing and locking processes can be reversed, allowing the structure to return to its initial state. Given that this cycle can occur multiple times, it is referred to as a repeatable process. While in some applications, such as shape-morphing orthopedic implants, permanent locking is required, some other applications, such as robotics, require reversible and repeatable locking. The reversibility and repeatability of the locking mechanism is dependent on the activation energy required and its implementation in a specific design. The design also determines whether the

reversal process occurs passively (*i.e.*, through removal of the initial stimulus) or actively (*i.e.*, through the application of a second stimulus after the initial).

The proposed designs exhibit both reversibility and repeatability in their shape morphing and shape locking behaviours. The reversal process can occur passively or actively, depending on whether a snapping mechanism is present in the locking mechanism. In the absence of a snapping mechanism, the lock can be released by removing the magnetic stimulus, either due to gravity or by implementing a spring, making it independent of the orientation of the structure. When a snapping mechanism is present, the lock must be released by applying a magnetic stimulus in the opposite direction. Following the release of the lock, the structure can be transformed and locked again. These processes can be repeated multiple times, although repeated use may induce wear as suggested by the diminishing snapping forces depicted in Figure 3.5.

3.3.3 Selective locking

Selective locking refers to the ability to restrict or manipulate the motion of a structure by constraining specific joints or DoF rather than affecting the motion of the entire structure. The optimal method of constraining depends on the application. In the case of implantable devices, for instance, it is advisable to ensure maximum stability by completely locking the mechanism using a minimum number of locking elements [13]. In soft robotics, however, it may be beneficial to have selected region locking, allowing certain regions of the structure to deform easily while other regions remain locked. The current design locks the joints in groups of four per body. The magnetic field can be manipulated and directed to lock several or all joints. This localized behaviour is also applicable to the manipulation of individual body positions.

The simulated findings of making elements passive and removing redundant constraints (Figure 3.4d–i) were implemented in a physical design (Figure 3.7d–e). Indeed, not all elements need to be locked to remove all DoF from a structure. This approach reduced the complexity of activation. However, it also limited the options for selective locking and decreased the locking strength as compared to the case where redundant constraints were used. In physical implementations, the strength of the locked structure

decreases as passive elements are introduced. The redundant constraints contribute to the maintenance of the structural integrity and could result in a more stable load bearing structure. Therefore, adding too many passive elements without this consideration is suboptimal. One of the benefits of using passive elements, especially those made of a single material, is the feasibility of fabricating the structure using efficient, non-assembly manufacturing techniques, such as via MJT-UV [51] printing technology, which could lead to reduced manufacturing costs.

3.3.4 Continuity

The locking of a morphing structure can be applied at specific stages of the morphing process or continuously to any arbitrary shape of the structure. A ratchet system, for example, has discrete steps at which the position is fixed. To eliminate these steps, a mechanism that operates with deforming materials or friction can be incorporated.

The mechanical lock in the presented designs is based on the discrete blocking of a joint. The teeth of the non-rotating ring engage with those of the struts ends. This lock is more straightforward and easier to implement than a friction lock, but it has the disadvantage of having a limited number of discrete locking positions. This may constrain the range of the shapes and positions that the structure can assume. This design, however, also offers the advantage of being more reliable and easier to control than a friction-based lock, since it is less impacted by external factors, such as temperature and humidity.

3.3.5 Applications, design, and manufacturing

Shape-morphing and locking structures can be applied across a diverse range of research areas from biomedical engineering (*e.g.*, orthopedic implants and exoskeletal suits), to both soft and conventional robotics, and the design of gripping systems. Within the medical implants domain, these advanced structures facilitate the creation of adaptive implants specifically engineered to integrate seamlessly with the human anatomy [27, 57]. This enhances not only patient comfort but also the functional efficacy of the implants and prosthetic devices. Moreover, exosuits, integrated with shape morphing technologies, offer ergonomic and mechanically effi-

cient support for human locomotion. These suits find diverse applications ranging from physical rehabilitation and augmentation to specialized industrial tasks [58]. In the robotics sector, shape-morphing technologies endow robots with the capacity to dynamically adapt their shape, thereby enhancing their functional capabilities in terms of locomotion, manipulation, and overall versatility [59–62]. Soft robotics, in particular, can benefit from these advanced structures, as they enable more secure and nuanced interactions with delicate objects (*e.g.*, human soft tissue) [60]. This expansion in interaction modalities consequently broadens the scope for human-robot interactions, for example, in minimally invasive surgeries [60]. Regarding robotic grippers, the incorporation of shape-morphing and locking materials into such devices provides them an ability to grasp a wide range of objects regardless of their varied shapes and sizes [59]. This capability is particularly valuable in industrial contexts that require flexible automation strategies. It should be noted that the applicability of shape-morphing structures is not limited to the aforementioned categories. The design of these structures can be precisely tailored to optimize performance across a myriad of applications, suggesting new horizons for developing smart materials with multiple functionalities.

The design and manufacturing choices play a significant role in determining the performance of a mechanism. For instance, not all the joints in a network need to be hinges to ensure planar deformation. Cleverly alternating between hinges and spherical joints can ensure the desired deformation behavior is achieved while preventing self-stress in the structure as much as possible. Reduction in the number of locked elements as presented here is a first step toward optimization for reducing self-stress. Further and more sophisticated mechanical analyses using finite element models combined with optimization algorithms could further enhance the design in terms of minimizing self-stresses and is suggested as an avenue of future research. Another example is that a morphing structure with many DoF and smaller components will generally perform better in reaching a target shape. Different manufacturing methods that use various materials result in different characteristics, including dimensions, weight, resolution, tolerance, surface roughness, friction, wear, biocompatibility, and ease of operation and processing. These characteristics can be fine-tuned to satisfy the specific requirements associated with any application.

This work aimed at demonstrating the concept of locking a kinematically deforming mechanism, rather than optimizing it for a specific application. To this end, the structures were made as small as possible using available 3D printing techniques (Table 3.1). While (some of) the proposed designs are manufacturable using other fabrication approaches, AM provides additional flexibility, lower costs, and shorter lead times that make it easier for researchers to experiment with different designs. AM also has the potential to be used for an end product because non-assembly AM approaches could circumvent much of the challenges associated with the assembly of large kinematic structures made using other techniques. The post-processing required for the MEX printed parts was minimal, while MJT printed parts required more extensive post-processing. It was observed that the friction between the locking ring and the MEX printed parts was less than the one between the locking ring and MJT printed parts, possibly due to differences in their surface roughness. The selected design presents some limitations in terms of its morphing capabilities, as it can only deform in-plane. Nonetheless, stacking multiple layers can approximate 3D target shapes (Figure 3.7a–c). The manufacturing techniques were selected based on the ease of experimentation, which is why 3D printing was used. Ideally, the designs would be non-assembly. Given the current state of 3D printing technology, this is only possible for specific parts of the designs. That is because the application of the magnetic fields requires differential magnetic responses in the 3D printed materials. This calls for the simultaneous printing of magnetic and non-magnetic materials. Moreover, the clearances required for the kinematic joints necessitate the use of a solvent-soluble or otherwise removable support material. There are currently no readily available multi-material 3D printing techniques that can simultaneously print all these materials with sufficient quality and resolution to enable smooth functioning of both shape morphing and shape locking mechanisms. While we were successful in removing many of the otherwise required assembly steps, there were still a few assembly stages that were needed for incorporating all the printed materials and components.

To improve the manufacturing of the structures, alternative methods and materials, such as powder bed fusion of metal using a laser beam (PBF-LB/M [51]), could be employed. PBF-LB/M [51] has a resolution

that varies with the granulometry of the powder used and the laser spot size and is typically in the 0.01 mm to 0.1 mm range. It also enables the use of both magnetic and non-magnetic powders (*e.g.*, iron, nickel, or cobalt alloys), although most printers can print only one material at a time. Other extrusion-based metal printing techniques may offer the potential for multi-material printing and the use of biocompatible magnetic materials [97, 98]. Another avenue for improvement is the development of multi-material 3D printing on a small scale, which would enable the creation of an integrated, non-assembly structure. Further improvements in material selection, geometry, and dimensions could lead to the creation of alternative configurations with the same basic conceptual design and functionality. For a magnetism-based mechanism as presented here, we need a non-magnetic as well as a magnetic material. The composition of these materials can be polymer-based, as used here, or fully metallic if AM techniques allow it [99]. Numerical simulation serves as a pivotal tool in optimizing the design of these structures, as demonstrated through the kinematic analysis presented in Figure 3.4. Additional computational models may be utilized, for example, to predict the overall strength of the structure. In all these choices, it is essential to emphasize that the primary goal of locking is to stiffen the structure, enabling it to maintain its shape and support the loads it experiences as required by the design objectives.

3.4 Conclusions

In this study, we presented the implementation of a magnetic locking mechanism in a shape morphing structure to support loads. The kinematic structure, which deforms in-plane, has revolute joints that are mechanically locked using magnetism. We utilized two additive manufacturing methods to fabricate prototypes of the conceptual designs. We also evaluated the mechanical performance of the locking mechanism and demonstrated its application in a closed-loop grid and showed how the activation effort can be reduced through design iterations. Furthermore, we extended the design of the proposed mechanism and demonstrated its applicability for certain types of 3D encapsulations by stacking in-plane structures. Our study highlights the feasibility of a locking concept and

provides insight into design considerations for the locking mechanisms. It also offers a methodology for analyzing the kinematics of the system through simulation. With further improvements and optimization, the designs presented here may have the potential for broader applications in such fields as robotics, architecture, and biomedical engineering. The design can be further enhanced and optimized to increase its efficiency and effectiveness.

Acknowledgments

The authors would like to thank Mauricio Cruz Saldivar for his support, especially in the deployment of the PolyJet.

Chapter 4

Discerning Design

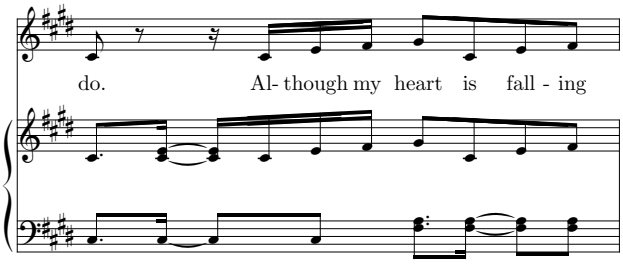

Ed Sheeran, Steve Mac and John McDaid,
third chorus bar from *Shape of You* (2017)

Abstract

Biocompatible and shape-morphing metallic structures have been proposed for musculoskeletal applications to provide structural support to bony tissues. However, fabricating these structures to conform to a wide range of curvatures, including both single and double curvatures, remains a significant challenge. In this study, we present and analyze structures featuring a regular tiling network connected by spherical joints, forming a chain mail-like mechanism capable of adapting to complex geometries with clay-like flexibility. Simulations using a multibody kinematics model

Modified from [16]

show that parameters such as unit cell shape, dimension ratios, and substrate curvature affect the shape-matching abilities of the structure. Experimental validation using specimens additively manufactured through laser-based powder bed fusion (from Ti6Al4V) and full-field strain measurements performed through digital image correlation confirms the simulation results, demonstrating that reducing structural density (*i.e.*, fewer bodies, struts, and joints per unit area) improves shape adaptability. However, the improved shape morphing capability often comes at the expense of mechanical strength under uni-axial tensile loads. These findings provide a framework for optimizing structures designed to achieve efficient surface conformance and adaptability in load-bearing applications.

Keywords

shape-morphing; shape-locking; metallic clay; laser-based powder bed fusion; curvatures.

4.1 Introduction

Medical devices perform better when closely conforming to each patient's unique anatomy. An anatomically tailored fit improves functionality and patient outcomes in applications requiring precise structural integration and stability. Examples of those are orthopedic implants and casts (Figure 4.1a), or cloaking of the warping heart where the timing of each contraction demands precision by a stable fit [100]. However, achieving this level of customization presents a significant challenge. Therefore, a key question is whether medical devices should be individually tailored to each patient or if adaptable designs can be developed to fit a wide range of anatomies. Currently, there are two main approaches to addressing this issue: first, fully patient-specific devices, which provide a precise anatomical fit but are costly and time-consuming to produce, and second, generic devices, which are more scalable and affordable but lack precise customization. One of the primary geometric challenges of both approaches is accommodating complex curvatures (*i.e.*, single or double curvatures) that vary significantly between different anatomical regions and among different people.

This need for adaptable, shape-matching structures extends beyond healthcare [101]. It is also critical in fields such as robotics [9, 102], aerospace [103], and automotive engineering [26, 104], where components often need to interface with curved or irregular surfaces. In healthcare, particularly in musculoskeletal applications, advances in additive manufacturing (AM) and image-based design techniques have enabled the development of "patient-specific" devices that precisely match individual anatomies [105–116]. Clinical studies have shown that these customized devices reduce the stresses on surrounding tissues, promote faster healing, and improve integration with bone structures, resulting in better patient outcomes [114, 117]. However, despite these benefits, patient-specific devices' high costs and extended production times limit their accessibility. While more affordable in manufacturing, mass-produced generic devices often require additional surgical adjustments [118] and can lead to longer recovery times and less favorable results [106, 119].

The trade-off between customization and cost-effectiveness highlights a critical limitation of patient-specific devices [120, 121]. While these customized devices offer improved clinical outcomes in treating various musculoskeletal diseases [122], they are usually much more expensive than their generic counterparts. Most of the costs of patient-specific medical devices stem from the time-consuming and labor-intensive design process required to tailor each device to the anatomy of individual patients. As a result, it is often not feasible to use such medical devices to treat all patients who might benefit from such a customization process. Moreover, the long lead time required for the design of patient-specific implants (*e.g.*, up to six weeks for some orthopedic implants) makes them unsuitable for urgent surgical cases, such as trauma interventions. Although advanced planning techniques and additive manufacturing in the surgical process have helped reduce surgical times and costs [111, 120, 123–127], these approaches still require an intermediate step between diagnosis and treatment, limiting their practicality in time-sensitive situations.

To address these challenges, we proposed the concept of "metallic clay" [13], a design approach in which medical devices, in general, and orthopedic implants, in particular, are engineered to exhibit both shape-morphing and shape-locking capabilities. This concept enables the devices to adapt to various anatomical shapes during installation and maintain the required

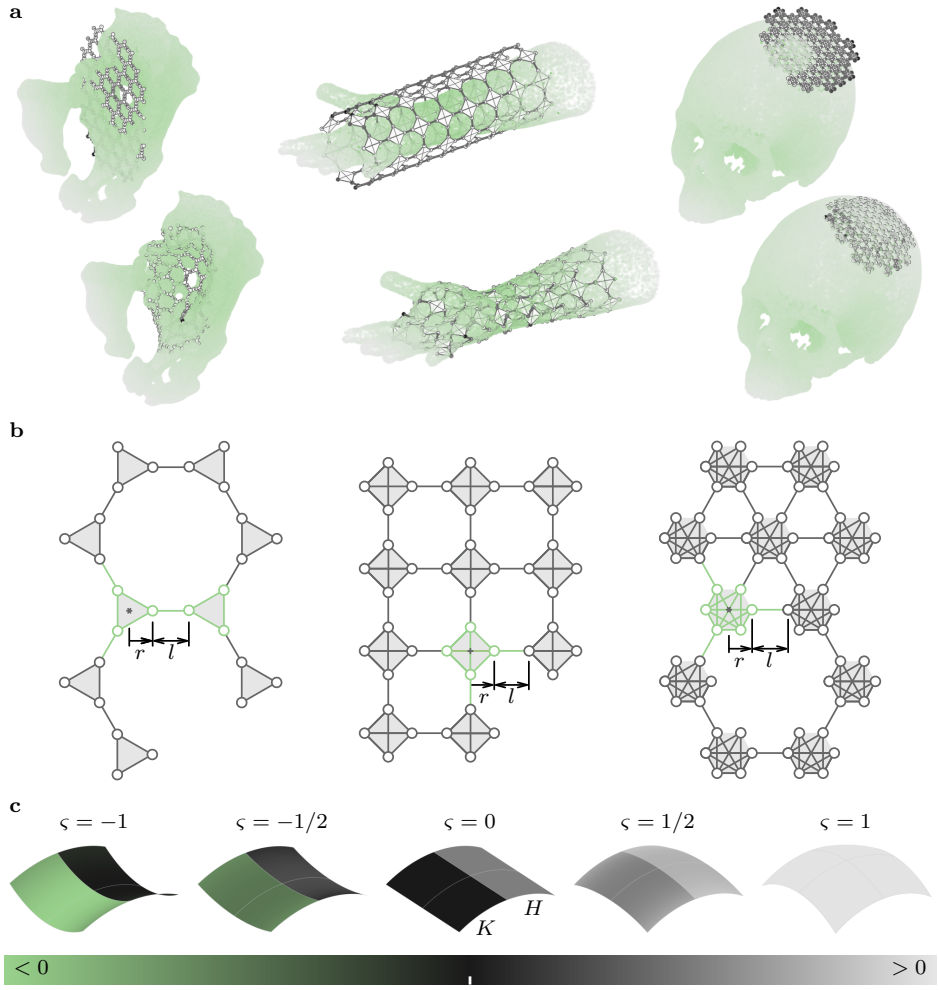

Figure 4.1: (Caption on next page.)

Figure 4.1: Illustrations of the considered lattice structures and the shapes they conform to. a) Three possible applications where a lattice structure takes the shape of shapes with a variety of curvatures; an acetabulum, lower arm, and skull. b) Three in-plane layouts of the lattice maille-like regular tiling structures: triangles (trigons), squares (tetragons), and hexagons. The body shape of the lattice structure was fully defined by a "radius" r and a link length l, modeled as a system of nodes (circles) and constraints (lines). c) The surfaces were created from the "toroidal" expression $(x,\, y,\, z) = (\rho \cos v,\, a \sin u,\, \rho \sin v)$, with $\rho = a(\varsigma \cos u - \varsigma + 1)$, where $-\pi/2 < u < \pi/2$, a is the length of one semi-axis ($\{a\} = 1$ in figure examples), and ς is a factor that relates the second semi-axis to the first.

form once placed. Such shape-morphing behavior introduces the potential for "collectivized" implants, standardized medical devices that can still adapt to diverse anatomies. We could have a single implant design taken off the shelf and applied to various medical cases at hand. Thereby, it could extend the benefits of anatomy-matching to a broader patient population while reducing lead times and enabling their use in urgent interventions. The concept of metallic clay, however, is still in its infancy. While we have previously proposed a framework for the design of shape-morphing orthopedic implants [14], it has not yet been applied to complex geometrical challenges commonly encountered in actual surgical scenarios.

We define the principles of shape-morphing and possible locking of a structure as, respectively, the ability of the structure to take a specific shape and to maintain that shape due to constraints that remove degrees of freedom once a specific shape is achieved [13]. The morphing and locking can be activated through different methods [15]. In studying how well different designs can adapt to various curvatures, the kinematics of shape-morphing behavior is more important than the exact shape-morphing mechanism. As for the locking mechanism, we use an irreversible method appropriate for orthopedic implants [128, 129]. Here, we investigate a pattern-to-pattern shape morphing [130] where the structure is shaped over a substrate through external influences, resulting in a "molded" structure. The locking process occurs by applying an external cement that irreversibly secures the structure over time.

Our previous studies explored the broad concept of "metallic clay" [13, 14] and here we will investigate the characteristics of one implementation of the concept, namely a lattice structure that is inspired by chain mail (Figure 4.1a–b). Traditional chain mail structures [131] are defined

as a 2D sheet but can change shape to become 3D. The structure's nature also dictates a regular pattern in the connected moving parts. This network can be altered nonetheless, both in terms of pattern and in geometry. Hence, they are relatively simple structures that allow for experimenting with the effects of a comprehensible set of different parameters. Moreover, these structures combine the flexibility of shape adaptation with the structural strength required for load-bearing. This combination is particularly valuable for applications that require support around curved or irregular objects, such as covering cavities on curved surfaces or immobilizing joints on the human body. In the search for "metallic clay" lattice structures, we explored chain mail-like structures as a promising design principle, merging adaptability with mechanical strength. In particular, it is not yet clear how well various designs of shape-morphing implants can conform to complex curved surfaces, which are common in orthopedic applications. Here, we study how different designs of shape-morphing 3D printed metallic structures adapt to complex geometries, focusing on the specific cases of curved surfaces. Curvature is one of the most important geometrical features in 3D shapes [132–134]. Therefore, we explored how various design parameters, such as the configuration of the network connections and the length of structural struts, influence the ability of metallic lattices to conform to single- and doubly-curved surfaces.

The principles of traditional chain mail are replicated, but its design is adapted to gain new multibody structures. As also shown in another study [129], ball-and-socket joints replace loosely attached chain links to connect the rigid parts. This replacement allowed for better control over the deformation of the structure and increased strength. The small hinges between rigid components supplied the numerous degrees of freedom (DoF) required for the structures to achieve the necessary flexibility for conforming to diverse shapes. On this scale, powder bed fusion is an ideal, if not the only, manufacturing technique capable of creating such complex structures in a single, non-assembled process. However, designing these mechanisms to be fully printable presents significant challenges, requiring careful consideration of the limitations of current 3D printing technology.

Both simulations and experiments were conducted to evaluate how various design parameters influence the performance of the structures. To this end, the structures were parametrized (Figure 4.1b). Target shapes

were varied according to one shape parameter (Figure 4.1c). The simulations focused on modeling the kinematic behavior of the system, while the experiments assessed both the shape-matching capabilities and the mechanical properties of the 3D printed structures. The shape-matching performance of the structures was assessed by measuring how well the structures conformed to the contours of curved surfaces, with deviations quantified to assess the accuracy. In addition to shape adaptability, we also investigated the load-bearing capacity of the additively manufactured metallic structures to ensure mechanical reliability.

For mechanical testing, digital image correlation (DIC) was used to capture the full-field strain data during uni-axial tensile tests conducted using custom-designed fixtures. The results from simulations and experiments were analyzed qualitatively and quantitatively to evaluate the kinematic and load-bearing performance of the proposed designs. Through this study, we aim to demonstrate the potential of shape-morphing metallic structures as adaptable, load-bearing medical devices capable of conforming to complex anatomical shapes, offering a promising alternative to fully customized implants.

4.2 Materials and methods

4.2.1 Structure lay-out

A sheet-like structure can be used to achieve surface conformity through kinematic deformation. The different components of this structure were arranged in a tiling, or tessellation fashion, to create a regular pattern and reduce the number of variables involved in the design process. Moreover, in this study, we restricted our focus on the periodic tilings with a rotational symmetry, based on regular polygons [135–137], to simplify the design of bodies connected through linkages and spherical joints. This periodicity enabled us with three possible body shapes constrained by crystallographic restriction, including equilateral triangles with three planes of symmetry, squares with four, and hexagons with six.

Two parameters fully defined each shape: the body "radius" r and the link length l (Figure 4.1b). The total length $h = 2r + l$ was kept constant at 11.5 mm across all experiments. Also, all shapes were arranged on a

grid that fits within a square, with the distance from the center to the corner set at $(75/\sqrt{2})$ mm.

4.2.2 Definitions of shapes and curvatures

The shapes to which the structures conform were selected to reflect different signs of Gaussian curvatures. To come to a variety of curvatures in the selected surfaces for experimenting, we turned to surfaces of revolution [138]. The following parametric equations described these surfaces:

$$(x,\, y,\, z) = (\rho(u)\cos v,\; y(u),\; \rho(u)\sin v)\,, \tag{4.1}$$

where ρ is the varying radius along y. Different equations for ρ and y give different sets of surfaces as depicted in Table 4.2 and Figure 4.2.

The definite set of surfaces for experimenting includes curvatures of all signs and allows one to change curvature by adjusting one parameter. This set is shown in Figure 4.1c. It has

$$\rho = a(\varsigma\cos u - \varsigma + 1), \qquad y = a\sin u, \tag{4.2}$$

where $-\pi/2 < u < \pi/2$, a is the length of one semi-axis, and ς is a factor that relates the second semi-axis to the first (Figure 4.1c). The Gaussian K and mean curvature H of these surfaces are given by:

$$K = \frac{\varsigma\cos u}{a^2(\varsigma^2 - \varsigma^2\cos^2 u + \cos^2 u)^2(\varsigma\cos u - \varsigma + 1)}, \tag{4.3}$$

$$H = \frac{\varsigma + 2\varsigma^2\cos u + \cos^3 u - \varsigma^2\cos^3 u - \varsigma^2}{2a\,|\varsigma\cos u - \varsigma + 1|\,(\varsigma^2 + \cos^2 u - \varsigma^2\cos^2 u)^{3/2}}. \tag{4.4}$$

Note that this sign from the mean curvature comes from the (arbitrary) definition of the surface normal that is positive when pointing "away from" the axis of revolution. For certain values of ς when $-\pi/2 < u < \pi/2$, we obtain

$$\varsigma = -1 \quad \Rightarrow \quad K = \frac{\cos u}{a^2(\cos u - 2)}, \qquad H = -\frac{\cos u - 1}{a(\cos u - 2)}, \tag{4.5}$$

$$\varsigma = 0 \quad \Rightarrow \quad K = 0, \qquad H = \frac{1}{2a}, \tag{4.6}$$

$$\varsigma = 1 \quad \Rightarrow \quad K = \frac{1}{a^2}, \qquad H = \frac{1}{a}. \tag{4.7}$$

For our experiments, we set $a = 10(\frac{1}{2} + \frac{1}{2}\sqrt{5})^{-1}h$.

4.2.3 Experimental morphing, locking, and testing

The morphing and locking process was conducted by combining the structures with shape substrates (Figure 4.3). After manufacturing, the structures were morphed into the target shapes to verify their shape-morphing capabilities as predicted by the simulations. Once the structures were morphed into desired shapes, they were locked for further analysis.

A specific manufacturing technique with its corresponding design principles was chosen to achieve the desired behavior. We manufactured the structures through laser-based powder bed fusion of medical-grade Ti6Al4V ELI (PBF-LB/M/Ti6Al4V; SLM125, ReaLizer GmbH, Germany, Table 4.1). Design principles followed those required for non-assembly AM with this technique [13, 93], taking into account tolerances and overhang angles (Figure 4.3a–b). For example, the structures were designed so that individual kinematic components were self-supporting, allowing joint clearance to be created without the need for powder support, making the structures functional immediately after removal from the building plate and powder. For printing with powder as support and removal afterwards, the spherical joints needed an open side (Figure 4.3a). These open sides also resulted in a wider range of motion for the joints on two sides (Figure 4.3b). The struts being positioned with a diamond-shaped cross-section during manufacturing are also a result of efficient use of the powder as support. Making the struts as thin as possible gives a wider range of motion and decreases the chances of long struts touching a curved substrate. Furthermore, with an elastic modulus of about 110 GPa, the alloy ensured that the deformation is purely kinematic in an unlocked state. Moreover, the material was medical grade, demonstrating the potential for future medical applications.

Table 4.1: Manufacturing parameters used for the laser-based powder bed fusion.

	contour	hatch
slice height	50 μm	50 μm
laser power	88 W	88 W
exposure time	20 μs	5 μs
point distance	10 μm	10 μm
scanning strategy	–	90° alternating
hatch distance	–	150 μm
hatch offset	–	80 μm

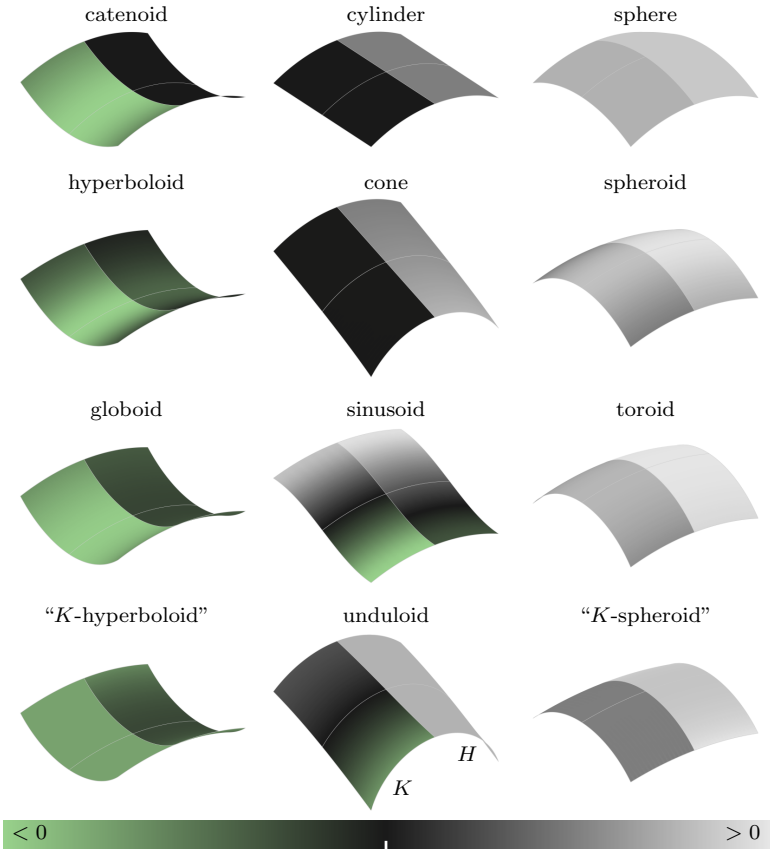

Figure 4.2: (Caption on next page.)

Figure 4.2: Different extracts of surfaces of revolution with Gaussian curvature K and mean curvature H. One can see how the curvature develops over the length of the surface, with on one half (left) the colors associated with Gaussian curvature and on the other half (right) the mean curvature. Constant curvatures over the surface are identified by constant colors; no gradient. Note that the direction of the surface normal is defined positive when pointing "away from" the axis of revolution, such that the color shading is the most convenient to interpret.

Table 4.2: Different surfaces of revolution with their radius and longitudinal coordinates. The full set of 3D coordinates is obtained by revolving a curve around the y-axis with $(x,\, y,\, z) = (\rho(u)\cos(v),\, y(u),\, \rho(u)\sin(v))$. Some equations require conditions on the parameters to ensure the shape has a correctly associated name. Note that the non-listed plane is the only surface with $K = 0$ and $H = 0$.

	radius	longitude	notes
cylinder	$\rho = a$	$y = u$	$K = 0$, $H =$ constant
cone	$\rho = au$	$y = u$	$K = 0$
sinusoid	$\rho = a\cos(u\pi) + b$	$y = u$	$b \geq a$
catenoid	$\rho = a\cosh(u/a)$	$y = u$	$H = 0$
globoid	$\rho = -a\cos(u) + b$	$y = a\sin(u)$	$-\frac{\pi}{2} \geq u \geq \frac{\pi}{2}$, $b \geq a$, [138]
toroid	$\rho = a\cos(u) + b$	$y = a\sin(u)$	$-\frac{\pi}{2} \geq u \geq \frac{\pi}{2}$, $b \geq a$
sphere	$\rho = a\cos(u)$	$y = a\sin(u)$	
spheroid	$\rho = a\cos(u)$	$y = b\sin(u)$	
hyperboloid	$\rho = a\cosh(u)$	$y = b\sinh(u)$	
"K-spheroid"	$\rho = ab\cos(u)$	$y = a\int_0^u \sqrt{1 - b^2\sin^2(\varepsilon)}\,\mathrm{d}\varepsilon$	$b > 1$, $K =$ constant, [139, 140]
"K-hyperboloid"	$\rho = ab\cosh(u)$	$y = a\int_0^u \sqrt{1 - b^2\sinh^2(\varepsilon)}\,\mathrm{d}\varepsilon$	$K =$ constant, [139, 140]
unduloid	$\rho = \sqrt{\frac{b^2-a^2}{2}\sin\left(\frac{2u}{a+b}\right) + \frac{b^2+a^2}{2}}$	$y = a\int_0^{\frac{u}{a+b}-\frac{\pi}{4}} \sqrt{\left(1 - \frac{b^2-a^2}{b^2}\sin^2(\varepsilon)\right)^{-1}}\,\mathrm{d}\varepsilon + b\int_0^{\frac{u}{a+b}-\frac{\pi}{4}} \sqrt{1 - \frac{b^2-a^2}{b^2}\sin^2(\varepsilon)}\,\mathrm{d}\varepsilon$	$b \geq a$, $H =$ constant, [141]

This method included custom molding and mechanical testing fixation. Substrate shapes were fabricated beforehand from silicone cast rubber (Poly-Sil PS 8520, Poly-Service, The Netherlands). The negative of the desired shape was printed with polylactic acid (PLA) using material extrusion (MEX-TRB/P/PLA). This negative was then used to pour the silicone rubber on, and in an overpressure, it was left to dry for a day. The result was a rubber substrate representing a desired shape on

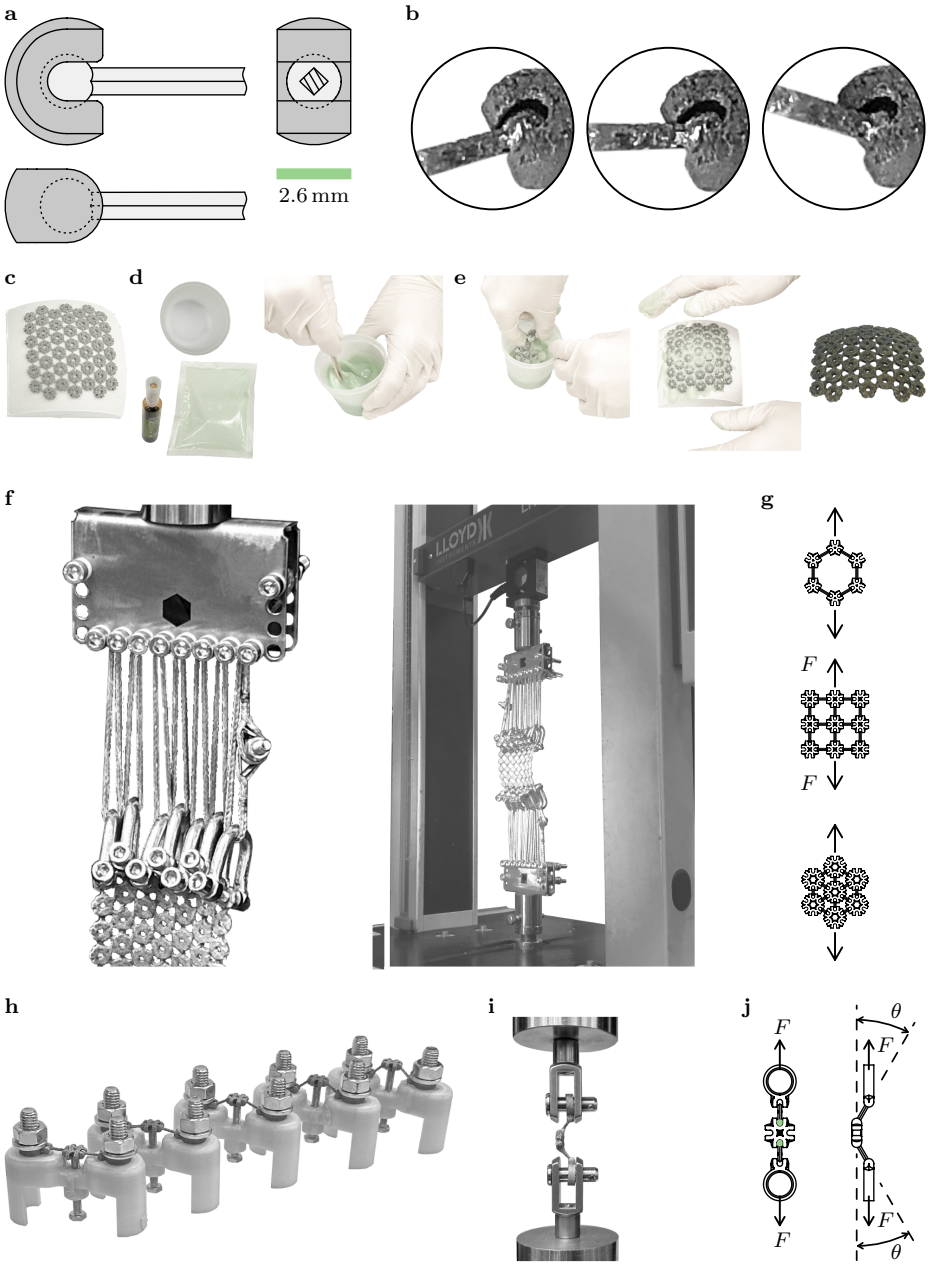

Figure 4.3: (Caption on next page.)

Figure 4.3: Design, molding, fixation, and mechanical testing of the samples. a) Schematic of a single spherical joint with dark grey socket and light grey a strut part with ball. b) Close-ups of a single spherical joint with different configurations. c) A silicone rubber substrate shape (sphere in this example) with a structure laying on top of it. d) The molding process with mixing the components, e) submerging the structure in the cement, and molding it manually on the substrate (a sphere in this example). f) The samples in the test setup. A detail of the custom fixture for a structure sample (saddle in this example) suspended in the testing machine and an overview of the testing rig with a structure and a DIC setup illuminating it. g) A schematic drawing of the loading directions for the different body shapes, showing applied (resultant) force F. h) The holders for setting individual bodies with different link angles during molding. Cement was applied to the angled joints through a syringe. i) A sample mounted in the test setup. j) A schematic drawing of the setup, showing the applied force F and set angle θ. Green dots indicate the locked spherical joints.

which the structures could be positioned Figure 4.3c). A low-viscosity two-component bone cement (PALACOS® LV, Heraeus Medical GmbH, Germany) was prepared according to the manufacturer's instructions (Figure 4.3d). Within two minutes of preparation, the structure was submerged in the cement and was crumpled twice (Figure 4.3e). Subsequently, redundant cement was percolated out, and the structure was folded and smoothed on the substrate. Finally, the cement was allowed to cure under an overpressure of 2 bar for ten minutes, after which the structures were removed from the substrate. The whole molding process is demonstrated in Supplementary Video 1 of [16].

A custom fixture was designed to suspend the samples in the mechanical testing bench (Figure 4.3f). The main idea behind this testing was to investigate the degree to which the samples were locked, *i.e.*, to investigate their deformation resistance after the cement was applied. For comparison purposes, the testing method should apply similar loading conditions to all structures in all shapes to look at shape effects solely. Therefore, we chose to take the morphed and locked structures and apply loads that attempt to pull them back into their neutral, straightened configuration. The shape-morphing structures underwent uni-axial tensile testing until failure, where the fixture ensured that forces remained in the plane at each point, minimizing any additional bending on the structure. The applied force is distributed equally over the bodies on an edge. Harp closures were modified to tighten them on individual bodies by screwing. On either side of the sample, one wire (Dyneema, Avient Corporation, USA) is laced be-

tween these harps and a "block" at the testing rig side in a zigzag manner. The structures were oriented under the load F as depicted in Figure 4.3g.

Separate body elements were also manufactured to test the effects of link angles θ on the strength under a load F (Figure 4.3h–j). The separate body elements were subjected to uni-axial tensile tests at different linkage angles θ, while the spherical joints were fixed using bone cement. The molding of the individual bodies was done by first setting the angles of the links in custom-made holders that allowed setting the angle by adjusting a screw (Figure 4.3h). The cement was then prepared, as previously mentioned, but this time was applied through a syringe. The individual bodies with different angles had rings (with unlocked spherical joints) that could be fixated as shown in Figure 4.3i and pulled straight. The uni-axial load F and link angle θ are oriented as shown in Figure 4.3j.

4.2.4 Simulation of the morphing process

To predict the shape-morphing qualities of the structures with respect to these shapes, we used a kinematic multibody approach developed in our previous study [14]. The structures were modeled as systems of nodes and constraints. The nodes defined the corners of the bodies and represented the center of spherical joints, while distance constraints (*i.e.*, links) connected the nodes of adjacent bodies. The different structures were lattices with 28 triangular, 49 square, and 45 hexagonal bodies (Figure 4.4a). All simulated lattices had $h = 2r + l = 11.5\,\mathrm{mm}$ with varying link length over body radius ratio l/r.

The morphing algorithm adjusts the positions of all nodes $\boldsymbol{x}$ to make the structure conform as closely as possible to a target shape. All possible linear motions $\mathbf{U}$, subject to constraints, were computed by solving $\mathbf{JU} = \mathbf{0}$, where $\mathbf{J}$ is the Jacobian of the constraint vector. Subsequently, the nodes were moved toward their target positions on the surface $\boldsymbol{x}_\mathrm{g}$ to obtain a new set of coordinates as $\boldsymbol{x}_* = \boldsymbol{x} + \mathbf{U}((\mathbf{U}^\mathrm{T}\mathbf{U})^{-1}\mathbf{U}^\mathrm{T}(\boldsymbol{x}_\mathrm{g} - \boldsymbol{x}))$. Due to the linear nature of the motions, this process requires several iterative steps. Note that the target positions $\boldsymbol{x}_\mathrm{g}$ were determined by minimizing the Euclidean distance between the current node positions and the parametric surface described by (4.1). The residual distance error is

$$\mathcal{E} = h^{-1}\sqrt{n^{-1}(\boldsymbol{x}_\mathrm{g} - \boldsymbol{x}) \cdot (\boldsymbol{x}_\mathrm{g} - \boldsymbol{x})}, \tag{4.8}$$

with the total number of nodes n, and the constant characteristic length $h = 2r + l$. This error serves as a metric for how well the structure is able to replicate the shape, with a smaller error indicating a better fit. When the distance error stopped to decrease between iterations (with a tolerance of $1 \cdot 10^{-6}$), the minimum was reached.

We varied three parameters, including body shape, the ratio of link length to body radius l/r, and the rotational placement angle φ about the vertical axis relative to the substrate (Figure 4.4). Structures with different body shapes were initially created in a flat configuration that fits within the defined total grid radius with $h = 11.5\,\text{mm}$ (Figure 4.4a). The ratio l/r was varied from 0.2 to 5 for all three body shapes, as illustrated in Figure 4.4b. For the rotational angle φ, we chose three different orientations, including i) alignment with a symmetry plane of the substrate, ii) no alignment with any substrate plane, and iii) alignment with a plane rotated by $\pi/4$ about the vertical axis with respect to a symmetry plane (Figure 4.4b–c).

4.2.5 Structure and substrate selection

Three structures were designed to represent the simulated grids of nodes and links (Figure 4.5a). The different designs of the structures were lattices with 45 triangular, 49 square, and 45 hexagonal bodies (note that these numbers are different from the simulations because of structural integrity). All lattices had a thickness of 2.6 mm and $h = 2r + l = 11.5\,\text{mm}$ with varying l/r (link length over body radius) depending on the body shape. The l/r values were chosen based on physical design limitations. For instance, the sockets of the spherical joints must touch each other to form a complete body. Consequently, the triangular bodies have the smallest radius, followed by the squares and then hexagons. Nine different locked structures, corresponding to different shapes, were created and compared with the simulations. Furthermore, three different substrate shapes were created to morph the structures into distinct shapes: saddle, cylinder, and spheroid (Figure 4.5b). Each combination of structure and shape was repeated three times, resulting in 27 specimens totally.

The shapes of the morphed structures were captured by 3D-scanning (Scan-in-a-Box-FX, Open Technologies S.r.l., Italy) (Figure 4.5b). Subsequently, the point clouds resulting from these scans were fitted on the

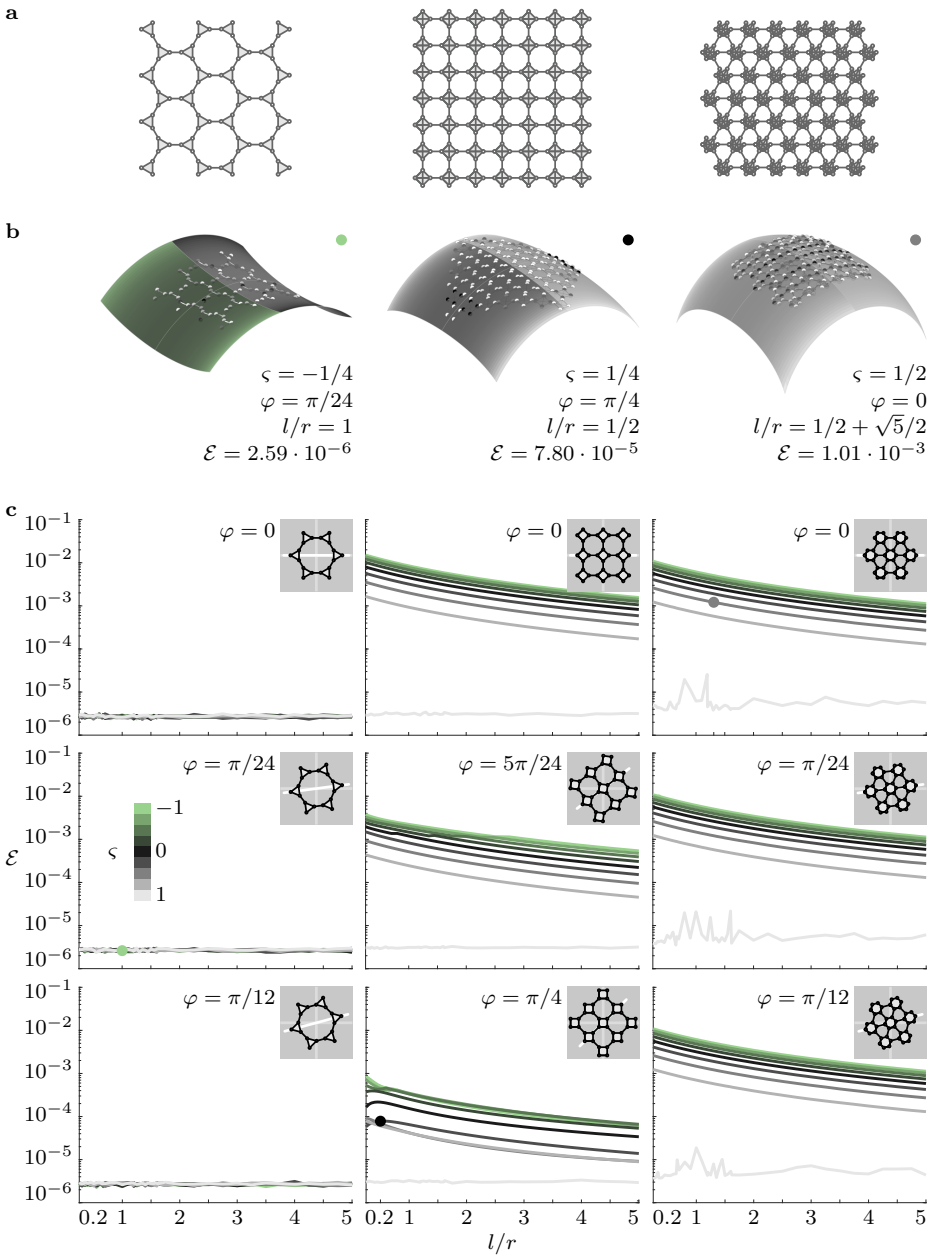

Figure 4.4: (Caption on next page.)

Figure 4.4: Shape-morphing simulations of the three structures into different surfaces of revolution. a) The different structures were lattices with a specific number of bodies and l/r (link length over body radius) ratio per body shape. b) Three examples of shape-morphing simulations for surfaces with a semi-axis radius $a = 10(\frac{1}{2} + \frac{1}{2}\sqrt{5})^{-1}h$, with $h = 11.5\,\mathrm{mm}$. The shape variable ς determined whether the surface was a saddle, cylinder, or ellipsoid (*i.e.*, has negative, zero, or positive Gaussian curvature). Rotation angle φ described the orientation of the structure with respect to the surface about a radial axis. The cumulative error $\mathcal{E}$ quantified how well the structure conformed to the surface. The shading of individual nodes depicts the local error at the node location, with a darker shading indicating a larger error. c) Graphs showing cumulative error values $\mathcal{E}$ for all simulations, varying ς, l/r, and φ. Note that the curvature shade values were normalized as $\hat{K} = a^2K$ and $\hat{H} = aH$ for more contrast.

surfaces' parametric description (4.1). The fitting algorithm considered all points of the cloud of one scan and minimized the cumulative distance to the surface. Finally, with every point considered as a node, the error metric (4.8) accompanying this fit quantified how closely the structures conformed to the target shapes.

Mechanical tests were performed to investigate how body and substrate shape affect the structures' strength. The mechanical testing included uniaxial tensile tests to assess the structures' resistance to returning back to their initial, flat configurations after being morphed to a desired shape. This analysis provided insight into the structure's joint strength and overall structural resilience. Individual body elements with five different link angles ranging from 0° to 60° were tested separately to get insight into the angle effect. These as well as all the shape-morphing structures were tested using a mechanical testing bench (LLOYD instrument LR5K, Hampshire, United Kingdom, 5000 N load cell) at a rate of $2\,\mathrm{mm\,min^{-1}}$ until failure. A specific specimen's weight normalizes the structures' reported load as $\hat{F} = (mg)^{-1}F$, with a specimen's mass m and $g = 9.81\,\mathrm{m\,s^{-2}}$.

In total, 27 locked shape-morphing specimens (three design groups times three shapes per three replicates) were experimentally tested. The mechanical testing machine recorded load and displacement data. We captured the true strain τ maps (the equivalent von Mises strains) at a frequency of 1 Hz using a 3D digital image correlation (DIC) system (Q-400, two cameras 12 megapixel each, LIMESS GmbH, Krefeld, Germany) and its associated software (Instra 4D v4.6, Danted Dynamics A/S, Skovunde, Denmark). For this purpose, we painted all the specimens white, followed by the application of a black dot speckle pattern.

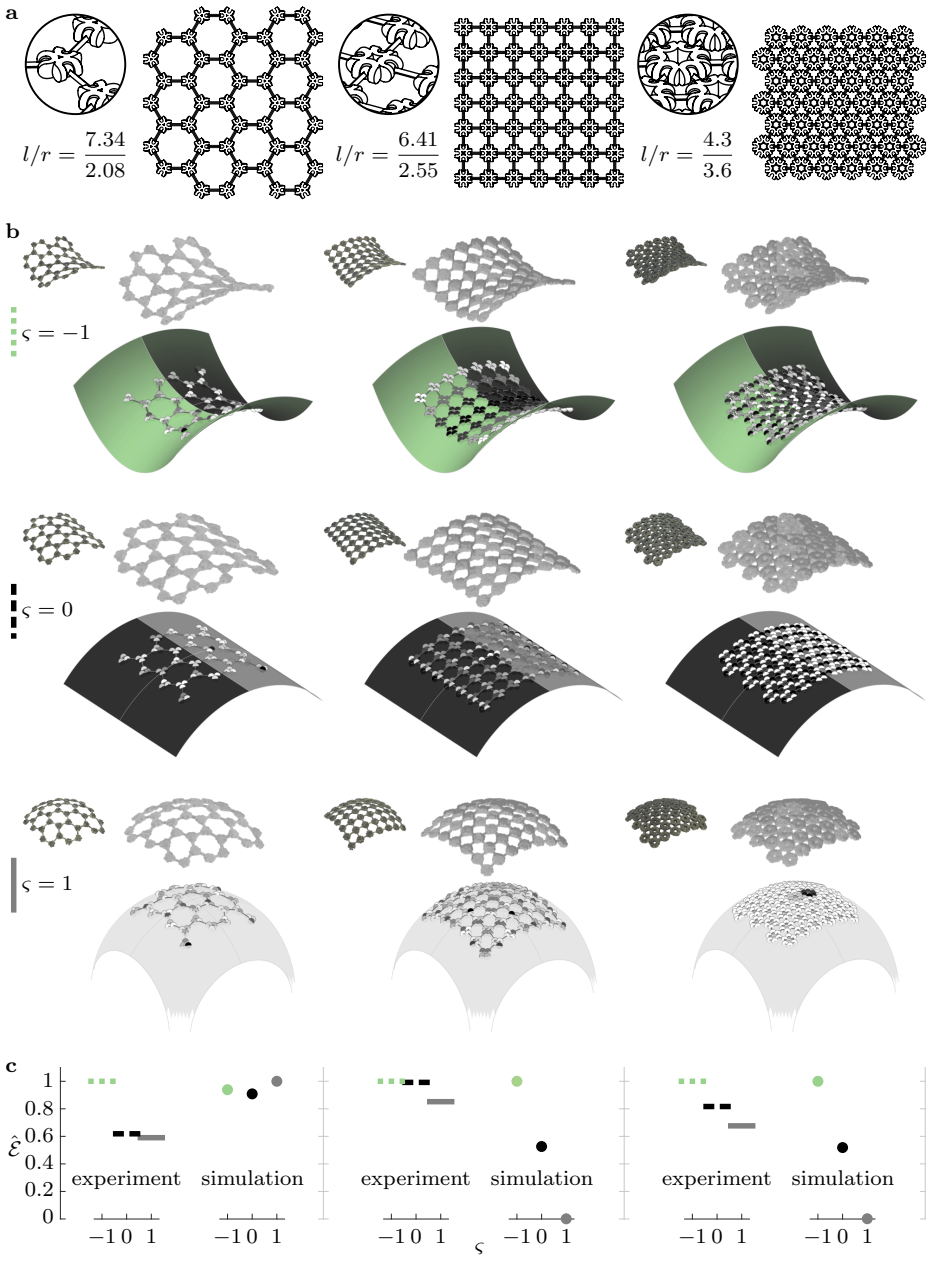

Figure 4.5: (Caption on next page.)

Figure 4.5: Shape-morphing experiments of three structures onto three surfaces. a) The different structures with a specific number of bodies and l/r (link length over body radius) per body shape. b) Visual comparison of the experiments by photographed, 3D-scanned, and simulated images. Structures were additively manufactured (PBF-LB/M/Ti6Al4V) and shaped into molds representing the respective surfaces of revolution with $a = 10(\frac{1}{2} + \frac{1}{2}\sqrt{5})^{-1}h$, $h = 11.5\,\text{mm}$, and three ς values. Bone cement locked them into shape. 3D-scans show how the experimental shapes compared to the simulated structures. c) The 3D-scans (experiments) were compared to the surfaces by calculating the normalized errors $\hat{\mathcal{E}}$. For each of the six data sets (three experimental and three simulated), the errors were respectively normalized with respect to the largest error found in the set. Note that the curvature shade values were normalized as $\hat{K} = a^2K$ and $\hat{H} = aH$ for more contrast.

4.3 Results and Discussion

4.3.1 Simulation results of the shape-morphing process

The shape-morphing simulation results showed how the design parameters influenced the quality of the shape fitting (Figure 4.4b–c). Overall, the shape-fitting error decreased (*i.e.*, the fit improved) with a reduction in the number of body vertices for the tested l/r with $\mathcal{E}$ around the order of 10^{-2} to 10^{-3} for hexagons, around the order of 10^{-3} to 10^{-4} for squares, and around the order of 10^{-6} for triangles. A decrease of about one order of magnitude (10^1) can be seen for an increase in l/r in the selected range from 0.2 to 5. Moreover, the error decreased as we moved from saddle to cylinder to spheroid surfaces with also approximately one order of magnitude (10^1) for all structure types at specific l/r. For triangular body shapes, in particular, the error remained consistently small, and neither l/r nor the substrate shape significantly affected the fit (Figure 4.4c). In contrast, the error decreased with l/r for square bodies, and the fit improved as we moved from saddle to cylinder to spheroid surfaces. Moreover, for the square bodies, the rotational orientation of the structure φ relative to the substrate influenced the error, with smaller errors occurring when linkages were less aligned with the symmetry planes of the substrate. Here, the error decreased from the 10^{-2} to 10^{-4} range to the 10^{-3} to 10^{-5} range. The error similarly decreased for hexagonal bodies with l/r and as we moved from saddle to cylinder to spheroid surfaces. However, unlike square bodies, the rotational orientation φ has negligible impact on the error for hexagons. By comparing all simulations per body

shape (*i.e.*, adding the errors per body shape for all respective orientations), we can conclude that the triangular shapes consistently provided the best fit, followed by square and hexagonal bodies.

The observed effects of design parameters on the shape-matching error can be explained by considering the geometry of the bodies. Triangular bodies, with three vertices, behave like a three-legged stool. All three vertices can easily contact the substrate surface on surfaces with reasonably small curvature, regardless of the curvature's sign or orientation. Square bodies exhibited larger errors overall, and their orientation plays a key role in whether all four vertices can contact the surface. When square bodies were aligned with the principal curvature lines of the substrate, the error was largest, while increasing the angular diversion from these principal curvature lines reduced the error. Another significant factor for square bodies was the l/r. Larger l/r values led to better fits, as smaller bodies with more than three vertices positioned closer to the surface improved shape conformity. Similarly, the error was smaller for larger values of the Gaussian curvature. Hexagonal bodies showed similar trends to square ones, but their circle-like symmetry with multiple symmetry axes minimized orientation effects.

4.3.2 Experimental results

The 3D printed structures made from different unit cell designs were able to morph into various shapes with different curvature values (Figure 4.5). The structure designs, including the maximum manufacturing area, were adjusted to meet the printer's constraints (Figure 4.5a). On the shape-morphed structures, we performed a qualitative analysis based on the results of the 3D-scans (Figure 4.5b) and compared these results with those of the simulations (Figure 4.5c. For all three body shapes and their respective experimental and simulated values (six data sets), we normalized the per-set error with the maximum error of each set. The earlier noted simulation trend, where the saddle shape shows the most error, followed by the cylinder and the sphere, is also noticeable in the experimental findings. In other words, the trends are qualitatively the same for each body shape. However, for the same body shape, the differences between some substrate shapes are so minor in some instances that we cannot draw definite conclusions. Quantitatively comparing shape morphing among experiments

and simulations is affected by the uncertainties in the manual molding procedure. Absolute values were not presented because these vary among the physical structures having finite thickness, and the model assumes zero thickness. In the experimental structures, the finite strut thickness means that not only the bodies but also the struts may touch the substrate if they are long enough or if the substrate convex curvature is high. To avoid this affecting the comparison, we ensured the struts were sufficiently thin and short for the curvatures considered.

The experimental results partially validated the simulations. We confirmed that spherical shapes were easier to conform to than saddle shapes. The fitting errors for the cylindrical shapes were between those of the spherical and saddle ones. This might be a surprising result, since the spherical and saddle (hyperbolic) shapes are doubly curved or non-Euclidean, compared to the single curved or Euclidean cylinder shape [132, 133]. A paper sheet cannot be bent into a doubly curved surface without being stretched in its plane. However, the structures presented here allow in-plane motions. The individual bodies in the structure can reorient with respect to each other under bending. Consequently, spherical shapes can be replicated better than cylindrical shapes. The differences between individual body shapes were not evident from the raw measurements before the normalization. Qualitatively, triangular structures morphed more easily across substrates, consistent with simulations showing they provide the best fit among the three body shapes.

4.3.3 Load-bearing capabilities

The load-bearing performance of each individual linkage was assessed through mechanical tests at various angles of positioning (Figure 4.6 and Table 4.3). The average maximum force at fracture showed that a larger linkage angle θ relative to the neutral position resulted in lower resistance to loads F. The increased linkage angle enlarges the moment arm of the applied force, and, thus, the same (bending) moment on the linkage and joint is reached with a lower F. Given that the locking was performed using bone cement, failures could theoretically occur either by fracture in the struts of the lattice structure or by detachment of the bone cement at the ball-and-socket joints. However, in our tests, all specimens exhibited failure through fracture in the struts, with no detachment at the joints.

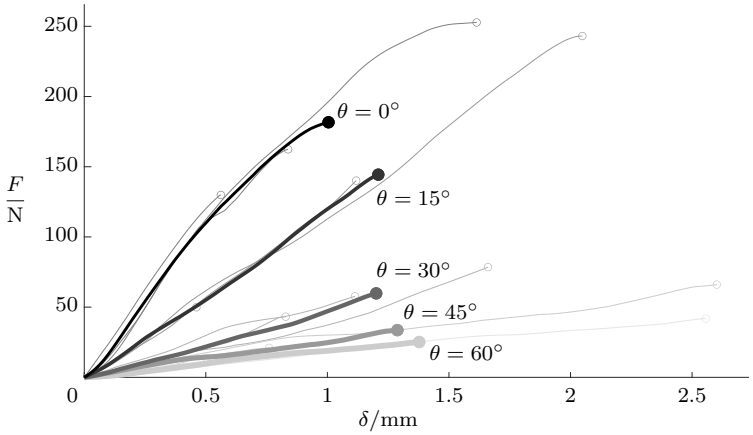

Figure 4.6: (Caption on next page.)

Figure 4.6: Mechanical test results of individual bodies with struts fixated at different angles. A plot of the applied force F *vs.* the displacement in the force direction δ for different angles θ. Bold lines represent the average of three specimens for each angle (thin lines with open circles show individual specimens).

Table 4.3: Mechanical test loads at fracture F_{f} of individual bodies with struts fixated at different angles θ. The load is the average of three specimens for each angle.

$\theta/\circ$	F_{f}/kN
0	0.18 ± 0.06
15	0.14 ± 0.10
30	0.06 ± 0.02
45	0.03 ± 0.03
60	0.03 ± 0.01

The absolute strains before failure over the structures during mechanical loading show similarities as well as differences for the different structures and shapes (Figure 4.7a). For all structures, the highest strains were found at the struts with values around 2%. The strains in the individual bodies in structures differ among body and structure shapes. Triangular bodies overall experienced the least absolute strain ($0 - 1\%$), followed by square ($0 - 1.5\%$) and then hexagonal bodies ($0 - 2\%$). The substrate shapes also influenced the strain distribution with analogies to thin plate theories. We found no clear distribution for the saddle, the cylinder has the least strain ($0 - 0.5\%$) along the "peak ridge", the spheroid has the least strain concentrated around the "peak" of the dome ($0 - 0.5\%$). The mechanical tests reveal that their geometry and the applied loading direction influence fracture and strain patterns in each structure. In the saddle configuration, fractures occurred along axes deviating 45 degrees from the loading direction, where the interaction of the concave and convex curvatures creates high bending strains. In the cylindrical shapes, strain was concentrated along the central axis perpendicular to the load, while in spheroidal shapes, strain was localized at the edges, where strain concentrations formed due to curvature uniformity disruption. Additionally, cylindrical structures exhibited the highest fracture load, followed by spheroids and then saddles (Figure 4.7b). Fracture loads increased on average from triangular to square to hexagonal bodies respectively (Table 4.4). Strain values were not normalized by applied load, so larger strain values may reflect higher applied loads rather than structural behavior.

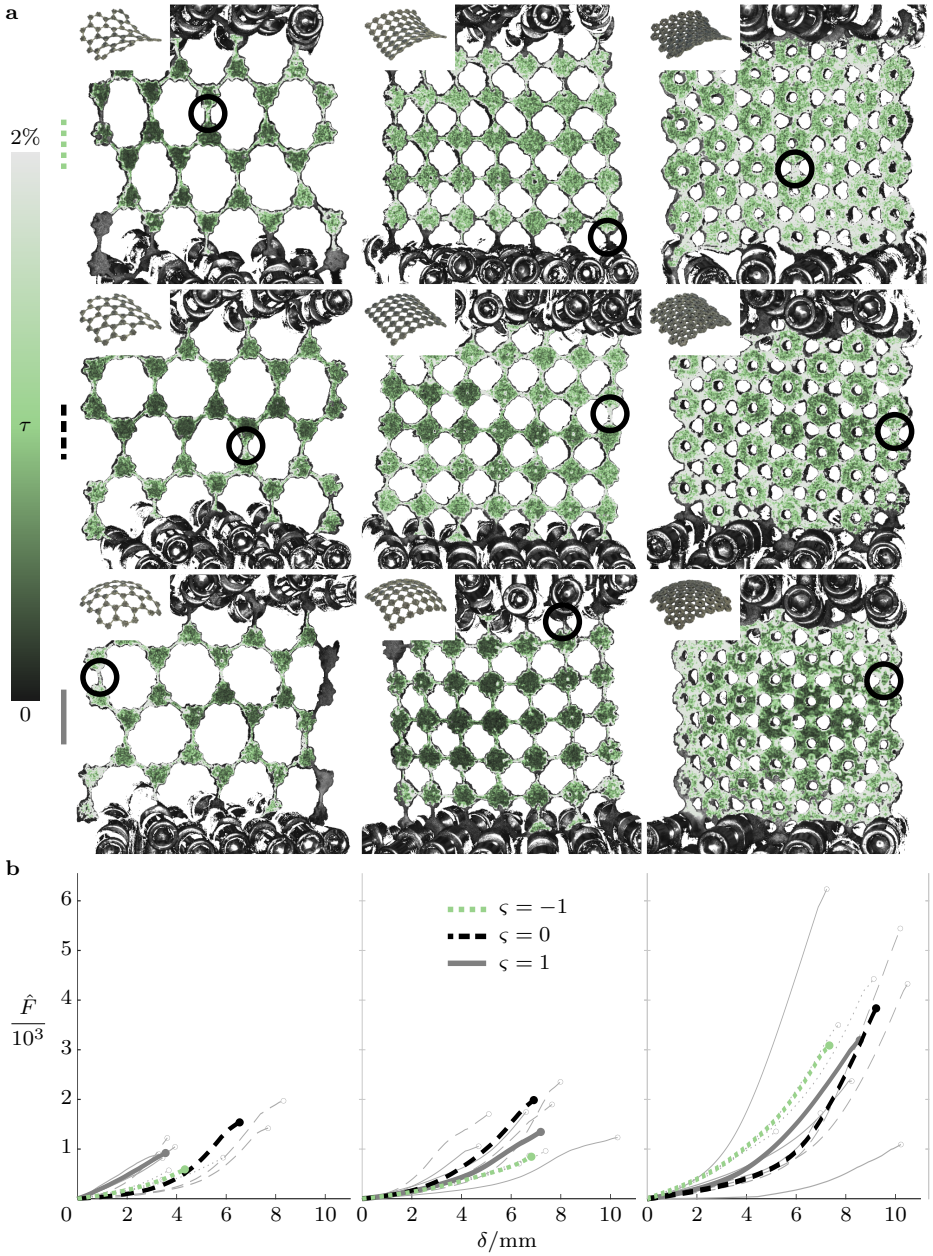

Figure 4.7: (Caption on next page.)

Figure 4.7: Mechanical testing of the different designs locked in the three different shapes, namely saddle, cylinder, and sphere. a) The structures were clamped at all bodies on two opposing edges to evenly distribute the applied force. The shading shows the true strain τ distribution obtained with digital image correlation (DIC) right before appearance of the first fracture as indicated by circles. b) Applied load F *vs.* the average displacement δ for the different shapes defined by ς. The force is normalized with respect to the weight ($\hat{F} = (mg)^{-1}F$, with mass m and $g = 9.81\,\mathrm{m\,s^{-2}}$) of the specific specimen.

Table 4.4: Mechanical test normalized loads at fracture for the different designs locked in the three different shapes. $\hat{F}_\mathrm{f} = (mg)^{-1}F_\mathrm{f}$, where F_f is the applied load at fracture, m is mass of the specific specimen, and $g = 9.81\,\mathrm{m\,s^{-2}}$.

$\hat{F}_\mathrm{f}/10^3$	triangular	square	hexagonal
saddle	0.59 ± 0.20	0.85 ± 0.13	3.09 ± 1.56
cylinder	1.54 ± 0.38	1.99 ± 0.34	3.83 ± 1.91
sphere	0.92 ± 0.13	1.35 ± 0.36	3.19 ± 2.58

4.3.4 General discussion

In evaluating the performance of the structures, we observe a trade-off between shape-matching ability and locking strength. Structures with fewer vertices and smaller body sizes exhibited better shape conformity, but this comes at the cost of reduced locking strength when subjected to loads that attempt to return the structure to its original flat configuration. The triangular and hexagonal bodies represented two extremes: triangular bodies, with fewer interconnections, deformed more freely and were easier to crumple randomly, but also exhibited weaker resistance to deformation once locked.

With these insights on the principles of one-size-fits-all structures in hand, we can work more toward applications. One example is fixing defects in the human acetabular bone. A study on this led to the development of a novel implant [129]. The structure, featuring hexagonally shaped bodies, serves as the base for developing the implant, as it offers the highest mechanical strength while still exhibiting sufficient flexibility to conform to the most pronounced acetabular curvatures.

Another option for further research is the design and creation of specific sheet layouts. The structure is then specific to anatomical sites, but not to individual patients. It could be possible to introduce different body shapes in one sheet, to have some parts deform easier, while other parts

are stronger. Methods like machine learning can aid in finding appropriate designs. In this light of versatility, sheets like the ones presented in this study are also of interest for fields like soft robotics. They can possibly be manufactured from different materials and with no or an alternative locking system. Design parameters of the structures could be optimized by simulation in such a way that the structure fits on the surface. Then, either different optimal structures for different surface curvatures are obtained, or one general structure can be designed that fits best on average on all possible curvatures. Optimized structures for different surface curvatures can be obtained to result in a one-fit-all structure that fits best on average on all possible curvatures and serves a wide variety of cases.

The mechanical properties were investigated from a geometric rather than a material perspective. We were only interested in the structural effects of the designs and considered only a single production method for the structures. Hence, the limits of the AM method dictated the envelope of possible structural designs. The ball-and-socket joint design allowed the balls to rotate freely within the sockets without requiring support during manufacturing. The struts had a diamond-shaped cross-section for the same reason: they did not require production support. These key elements of joints and struts were kept equal among all designs to ensure comparability. When changing joint and strut designs, the absolute load values that the structures can withstand change, but the trends observed between the structures with different layout designs and shapes remain relatively similar. Moreover, we used the same material to manufacture all the specimens. A different choice of material with similar stiffness and a similar layer-by-layer production method is expected to result in similar morphing behavior. Moreover, the relative performance of different designs in terms of the mechanical loads they can bear is expected to remain similar, regardless of the exact underlying material, as the structural design is the most dominant factor in determining the loading regime, stress concentrations, and even fracture sites. If the used material and manufacturing method produce more compliant parts, the shape-matching abilities may increase somewhat.

A better shape fit is expected to result in more uniform force distribution and is partially responsible for smaller stress concentrations. A larger contact area distributes the forces over a larger contact surface. If

the structure is perfectly rigid and has equal infinite stiffness throughout the whole structure, the peak stresses on the substrate would be smaller. However, the forces are not distributed equally over the contacts in physical representations with varying stiffness over the geometry, like the one presented in this study. More compliant regions can undergo lower contact forces than stiffer regions. As said before, geometry determines material behavior, with the thinner parts being more compliant than the thicker parts.

Shape morphing in this study is performed while the cement is already applied to the joints, which might thus affect the morphing. The viscosity of the cement is comparable to that of dish soap in its initial state. The manufacturer reports a preparation and application time of approximately 9 minutes at a room temperature of 20 °C for this cement. It was ensured that morphing was completed within the specified time frame for all experiments by applying the systematic approach depicted in Figure 4.3d–e and Supplementary Supplementary Video 1 of [16]. Since we were working in a quasi-static manner where the dynamics was unimportant, the cement is not expected to have affected the outcome of the morph. When considering dynamics, one should consider that viscosity influences the rotation rate of the joints.

The mechanical testing method with a custom fixture was designed to test the relative strength of structures that are initially 2D and deform to adapt to different 3D curvatures. The same loading conditions were applied to the different shapes to facilitate comparison. An out-of-plane compression test between two plates [137] does not ensure the same number of contact points between the structure and the plate. For example, a spherical surface has only one contact point with a flat plate, whereas a cylindrical surface has a contact line. This type of loading alters the conditions on a case-by-case basis, depending on the shape. The fixture used in this study aims to mitigate the consequences of this issue by distributing the load evenly across different shapes. The number of contact points remains equal for the same structure in different shapes, and the load is distributed in parallel across these contact points. The zigzagging of the low-friction wire ensures this load distribution. Once a fracture arises in the structure, the load conditions alter, and the measured load values lose significance.

4.4 Conclusions

This study investigated the kinematic deformation of additively manufactured chain mail-like structures made from a medical-grade titanium alloy regarding their shape-matching and locking capabilities. These structures, composed of rigid parts connected by ball-and-socket joints, could reinforce curved surfaces by forming a mesh and locking the joints once the desired shape was achieved.

A discrete multibody modeling approach was used to predict the kinematic behavior. Simulations identified three key parameters affecting shape conformity: the network pattern (*i.e.*, body shape), the ratio of body size to strut length, and the rotational orientation of the structure relative to the surface. Among the three patterns studied, triangular bodies provided the best shape-matching results, followed by square and hexagonal bodies. Increasing the strut-to-body size ratio improved shape conformity overall. At the same time, rotational orientation, *i.e.*, how the structure's pattern aligns with the shape's curvature pattern, only played a role for the square bodies.

Experiments were performed to validate the simulations. The designs were manufactured from medical grade Ti6Al4V ELI metal using PBF-LB. The specimens were placed in three generic shapes: saddle, cylinder, and spheroid. 3D-scanning the configuration showed that the employed multibody model can predict the shape-matching qualities of the specimens. Subsequent mechanical tests showed the locking strength of the designs. In terms of shape-morphing quality, the tiling pattern ranks in ascending order from triangle to square to hexagon, with the triangle performing about two orders (10^2) better than square and four orders (10^4) better than hexagon in terms of fitting error. This behavior is the opposite in terms of mechanical performance, with a hexagon resisting an approximately two times higher load before fracture than a square and about three times higher load before fracture than a triangle.

Acknowledgments

Color maps are created according to (hopefully correctly interpreted) theories of Crameri *et al.* [142]. P.H.dJ. would like to thank Ludovica Maga for demonstrating heart and contributing to the viability of this study.

Chapter 5

Discussion

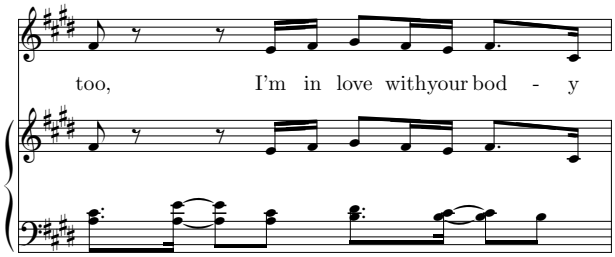

Ed Sheeran, Steve Mac and John McDaid,
fourth chorus bar from *Shape of You* (2017)

This work studied the shape-morphing and shape-locking of kinematic (discrete) structures through modeling and physical realizations. The kinematic nature of such freely deforming structures with their many DoF opened a direction of research that was not explored before. We needed to explore such structures' theory and real-world realization for further application. While specific biomedical, aviation and soft robotics applications were not extensively addressed, some more general conclusions regarding potential applications were drawn from the work presented here. Although directly deployable for some applications, the presented designs and solutions are mere examples of how some challenges can be addressed. The core finding of this study is the demonstration of the viability of the principle of morphing and locking mechanisms. In that sense, the current

work has sculpted the basis for further investigation and implementation and serves as a foundation for shape-morphing and -locking structures.

The presented modeling approach constitutes a systematic way to efficiently simulate the morphing behavior of shape-morphing kinematic structures. Since kinematic shape-morphing leads to structures with a discrete nature —where we are interested only in the position of specific points— we could reduce the model to a collection of nodes and constraints. This resulting modeling algorithm facilitated the analysis of the quality of the shape-morphing behavior and enabled a comparison between the different shapes achieved by the kinematic structures. It can be considered a tool for the design of kinematic structures. Especially since the simulations were successfully validated for their representation of reality by manufacturing and measuring physical structures.

The shape-locking of the designed structures brought its challenges. Having an initially flexible shape-morphing structure that turns into a stiff structure after shape-locking represents a set of inherently contradictory design requirements. We uncovered some of the important principles behind shape-locking through a case study. In this sense, the designed structures show a subgroup of infinitely many possibilities of locking structures. For example, we used magnetic fields for shape locking, but many other types of stimuli could be used for the same purpose. Although being a subgroup, this design still successfully revealed some of the widely applicable considerations in shape-locking. Interestingly, for example, it is not necessarily required to lock all joints to remove all kinematic DoF of a structure.

We also used another case study of structures with regular tiling to investigate design considerations for shape-morphing and mechanical performance within the context of curvature. Curvature was selected for this purpose because it is one of the most important geometry-determining properties. The effects of curvature on the morphing capabilities of the structures were clear as the structures fit better on spherical shapes than on hyperbolic ones. Varying structure design parameters, such as the body shape (*i.e.*, triangular, square, and hexagonal) and length ratios (*i.e.*, body radius over strut length), influenced the morphing capabilities of kinematic structures as well. Triangular bodies had better fitting capacities, followed by squares and hexagonals. Longer struts with smaller body

ratios fitted better as well. Hexagonal body shapes resulted in structures that could withstand the largest normalized loads aimed at unlocking the attained shape.

In the process of proving the viability of the concept and laying a base for further work, several recurring topics within the several chapters occured. These topics turned out to be constant considerations within the scope of shape-morphing and -locking of kinematic structures. In what follows, these topics are gathered from the relevant chapters in three categories and discussed further.

5.1 Multibody kinematic modeling

The model presented in Chapter 2 enabled a multibody description to be used within the context of kinematic shape-morphing. An analysis of the kinematics of structures with many DoF requires only a specific area of multibody dynamics to be applied. This stripped-down version of multibody dynamics used in the current thesis only utilizes nodes and constraints. The constraints must be carefully defined to make this relatively simple approach work for the shape-morphing under consideration. Chapter 3 added the implementation of toggling constraints on and off to lock and release a structure.

The method in which we find the kinematic motion modes and superimpose those to morph the system requires careful definitions of the constraints to avoid the occurrence of singularities. A node should not be constrained in a direction by a perpendicularly defined constraint, which can be understood in the context of a tightrope. Such a tightrope, in theory, constrains movement perpendicular to its length, but there is always some movement in practice; a force has no way to resist a perpendicular force, which can be extended to a constraint not able to resist perpendicular motion. In a mathematical representation, this results in singularities. Instead, the movement of a point is better restricted by a constraint drafted more parallel to the to-be-prevented movement.

Constraints continued. Although the presented model can be used as-is, we can still extend it to consider additional aspects (Figure 5.1). The presented constraints are not an exclusive list. The aim was to present constraint expressions that are differentiable and are computationally ef-

ficient. Elegance is found through simplicity. More types of joints can be conceived, but their implementation might be less elegant.

One should take care when drafting constraints and respect some guidelines. Every constraint should be unique, meaning that the same DoF should not be constrained by multiple constraints to prevent overconstraining and forgetting to constrain DoF that should be constrained. It can be such that the results of the morphing simulation are identical between a system that is just sufficiently constrained and several cases of overconstraining (Section 3.2.2). In drafting constraints, we also need to consider using vectors that can turn into zero vectors by system movement. Constraints relying on such vectors might give singularity issues in the analysis. Similarly, normalization or other dependencies containing divisions can result in division-by-zero errors.

An illustration of a common constraint that subjectively misses some of the aforementioned simplicity is the screw/thread joint. In that case, a rotational motion is associated with a translational motion. The thread's lead relates to a factor p and determines the translational movement associated with a specific angular rotation. Figure 5.1 shows an implementation that attempts to consider the guidelines, but more elegant or robust solutions might also be available. It was not tested, but for example, using atan2 available in most programming languages might be more robust to cover a 2π rotation fully.

Forces foreseen. Simulation of forces was not done in the scope of these studies but could be an extension of the already implemented multibody methods. The forces to dynamically steer the structures into a certain shape may be investigated by assigning mass and, in effect, inertia to the nodes. Even in the static domain, stiffness could be added to the joints to analyze flexure joints that more or less act as kinematic joints.

One of the model's extensions regarding locking could be analyzing forces in the system. Since locking is incorporated by adding constraints that remove DoF, we could extract constraint forces, for example, through Lagrange multipliers. Another route to locking is the implementation of a stiffness at the joints. Adding stiffness does not remove DoF, but with a high enough stiffness, we essentially lock a structure for all practical intents and purposes. Having stiffnesses would allow the extraction of forces associated with the deformation at the joints.

Metrics revolutions. We chose to quantify the shape-morphing here by defining a matching error and a shape factor. The error portrays the Euclidean distance among points of interest in the structures and the to-be-acquired shape, drafted as a standard deviation. This distance was the main shape-morphing performance metric used throughout this study. Similarly to the error, the shape factor is a metric for the distance of the structure's nodes from the centroid of the structure, indicating the shape of the structure. In its presented form, it is a basic number that is not necessarily exclusive to different shapes, but it gives a rough indication, which was sufficient for this study.

Both error and shape factor definitions could be modified to present more information. One could think of metrics such as other distances than the Euclidean, *e.g.*, the bottleneck or Hausdorff distance, or other metrics such as curvatures [44]. Exploring other metrics was not part of this study, but the presented modeling method allows experimenting with these metrics in shape-morphing structures.

5.2 Model-design interactions

The designs of shape-morphing structures can be investigated by simulation and realization. Chapter 3 showed how simulation could be employed to predict to what extent a structure is locked, and designs can be adjusted accordingly. Chapter 4 contributed to analyzing altering parameters systematically and how such changes impact the shape-morphing behavior of kinetic structures and their mechanical properties. More automation can be implemented in all these cases to obtain better designs.

The current modeling representation of the structures has simplifications regarding the actual physical design that one might want to address, where needed. Two examples of simplifications the model incorporates are the lack of finite dimensions to the nodes themselves and the lack of play in the joints. Here, the nodes represented joint geometrical centers without having any dimensions themselves. Hence, they can reach a surface closer than a physical design manifestation. Moreover, bodies and struts are represented by constraints that represent no finite thickness themselves. A lack of dimension that allows for penetration of substrates by the bodies and struts that real designs could not achieve. In physical designs that

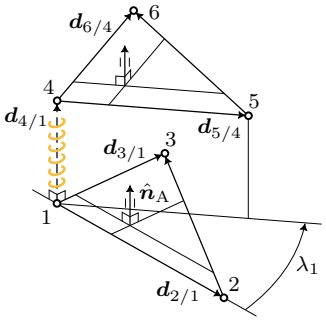

$$\boldsymbol{c} = \begin{pmatrix} \boldsymbol{d}_{5/4} \cdot \boldsymbol{n}_{\mathrm{A}} \\ \boldsymbol{d}_{6/4} \cdot \boldsymbol{n}_{\mathrm{A}} \\ \boldsymbol{d}_{2/1} \cdot \boldsymbol{d}_{4/1} \\ \boldsymbol{d}_{3/1} \cdot \boldsymbol{d}_{4/1} \\ \boldsymbol{d}_{4/1} \cdot \hat{\boldsymbol{n}}_{\mathrm{A}} - d_1 - \lambda_1 p \\ \boldsymbol{d}_{2/1} \cdot \boldsymbol{d}_{5/4} - \sqrt{\boldsymbol{d}_{2/1} \cdot \boldsymbol{d}_{5/4}} \cos \lambda_1 \end{pmatrix}$$

Figure 5.1: (Caption on next page.)

Figure 5.1: Illustration of the description of a two-body system with a thread connection that allows one DoF between the bodies. Six nodes together with (not shown) constraints define the two bodies with twelve DoF in total. The movement between the two bodies is constrained by the six shown constraints $\boldsymbol{c}$ drafted with position vectors $\boldsymbol{d}$. We use $\boldsymbol{n}_\mathrm{A} = \boldsymbol{d}_{2/1} \times \boldsymbol{d}_{3/1}$ and $\hat{\boldsymbol{n}}_\mathrm{A} = \boldsymbol{n}_\mathrm{A}/|\boldsymbol{n}_\mathrm{A}|$, and λ_1 is introduced as extra DoF to describe angles of any value and relate them through factor p to the translational position. In the presented form, the bodies are d_1 apart for $\lambda_1 = 0$, and p is positive for a right-handed and negative for a left-handed thread. For example, a thread resulting in 3 mm translational movement with one rotation has $p = 3/(2\pi)$ mm. The extra introduced DoF needs an extra constraint to leave the desired seven DoF of the complete system ($12 + 1 - 6 = 7$). Note that the system could be "locked" by adding one more constraint that dictates the angle, *e.g.*, $c = \lambda_1 - 5\pi$.

use non-assembly additive manufacturing, like the ones in Chapter 4, it is practically inevitable to have some clearance in the joints. These differences in mobility between the model and real-life design are expected to change the morphing capabilities of a structure. Therefore, care should be taken when using the model as-is. Nevertheless, simulation and validation throughout the chapters showed that the model, in its current elementary state, at least predicts the qualitative morphing capacities of the designs in accordance with real-life performance.

Optimizing options. By parameterizing the structures, optimizing the presented kinematic structures for specific applications is within reach. For example, it could be appropriate only to lock certain joints while still having a locked structure that supports loads sufficiently. Alternatively, shape-matching may be improved by implementing different joint types at different locations in a structure for a specific subclass of curvatures (Figure 5.2a). Further investigating the effects of parameters like shape and dimensions on the morphing and strength properties, as done in a first attempt in Chapter 4, has also relevance for further applications.

Again, because of the kinematically deforming structures' large number of movable joints and the considerable amount of accompanying options, a trial-and-error approach is unlikely to lead to (near)optimal results. The provided multibody modeling can provide a database of options, and subsequently, machine learning algorithms could be applied for a more systematic design optimization. In that regard, the multibody modeling might even be useful in ways that do not initially look like multibody problems, *e.g.* in optimization of guiding channels trajectories (Figure 5.2b).

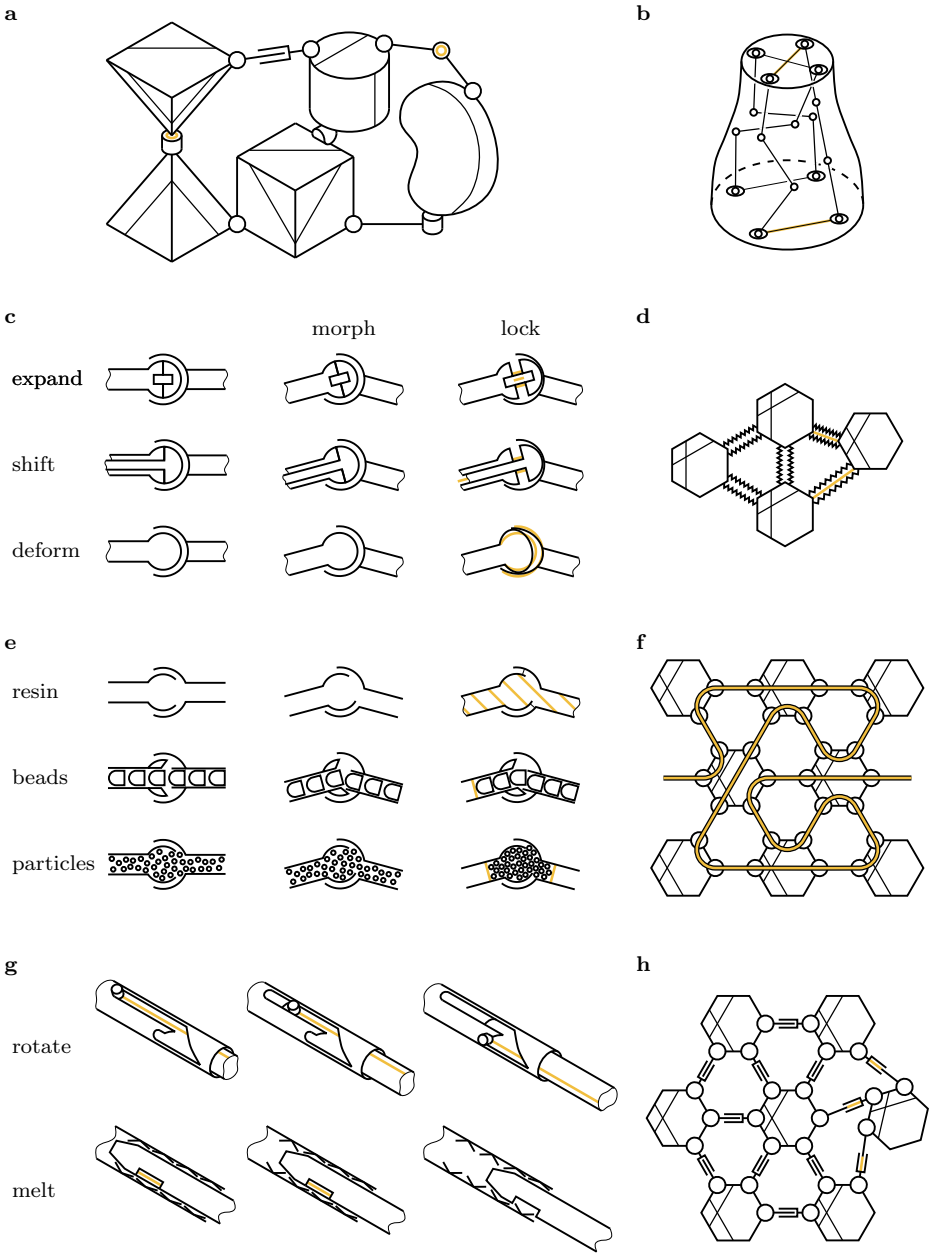

Figure 5.2: (Caption on next page.)

Figure 5.2: Possible future shape-morphing and -locking implementations and principles. a) We might apply assigning algorithms to systems of bodies to determine the optimal distribution of kinematic joint types. Machine learning could be used to assign the joint types and determine whether they should be lockable for specific applications. b) An unsolved optimization where two pairs of channels need to be connected such that on one side, one pair's channels are next to each other, and on the other side, they are opposing each other [143]. Under no circumstance can the channels intersect each other. The multibody modeling approach can be applied when we require properties such as equal length or curvature among the channels. c) Locking by dislocation per, for example, changing the spherical shape by expanding an element by magnetism, shifting an element mechanically from outside of the joint, or deforming the whole joint by using materials that exhibit memory behavior activated by temperature d) The joints in a multibody system can also be (hollow) flexures. For example, connections resembling the bellows used in early mechanical ventilators. e) Locking by jamming a channel in the joints, for example, by inserting a hardening resin, pushing together beads in the channels, or using particle jamming by applying pressure at the end of the channel. f) Using channels in the structure can introduce the question of how the channels should be connected. For example, a specific layout may be required to reach all joints in a structure by one channel. Finding this layout could be another optimization problem. g) Locking can also be done in prismatic and cylindrical joints, for example, by a pen(cil)-like or ratchet-like rotating mechanism that locks upon reaching a particular translation, or a mechanism that initially can move with covered obstructions and is locked into place by removing specific material through melting or dissolving. h) Translational joints introduce more manners of morphing and locking a structure. For example, in an in-plane structure, bodies can individually rotate in the plane or move out of the plane and lock degrees of freedom in the process.

5.3 Physical design considerations

The type of shape-morphing mechanisms presented in the study also give rise to specific design considerations. A vast number of joints can render any design too complex to analyze. Generally, better shape-matching behavior is obtained by a structure with smaller individual parts because smaller parts can better follow irregularities. The smaller the parts, the more "continuous" the structure and the more clay-like properties are obtained. However, manufacturing on a smaller scale presents a separate set of challenges.

Manufacturing additions. In terms of manufacturing possibilities, additive manufacturing is the most promising method. Structures can be produced in a single step, partially demonstrated in Chapter 3 and fully in Chapter 4. However, if assembly is required, the efficiency of manufacturing is compromised. In addition to that, some locking methods inherently

require the addition of another material in the locking step. The application and the design often dictate the choice of material. Fortunately, additive manufacturing allows for a great variety in materials and designs.

3D-signed. The primary challenge in effectively designing shape-morphing structures, *i.e.*, without an assembly step, seems to lie in the creation of fully 3D structures. Additive manufacturing requires support structures during the manufacturing process when not carefully designed. We demonstrated that structures can be designed in a sheet fashion without requiring an assembly step. These structures can then deform in and out of the plane to take a 3D shape. The next step is to create a non-assembly structure that has many DoF and is fully 3D to start with, is the next step. Support structures that can dissolve are promising, but this currently restricts the choice of material to polymers and biodegradable metals.

Future refurbished. Some ideas for designs were never fully developed in working prototypes. There is no claim that these ideas are new or original if even such ideas exist. They popped up and were shaped during many conversations and trials in the research process and are, by all means, a joint effort. A selection is gathered here out of gratitude and to illustrate and hopefully inspire future research and development on shape-morphing and -locking (Figure 5.2). These research directions' main principles and ideas can be combined and mixed for even more advanced and multi-faceted designs and analyses.

Credits

Arguably the most substantial part of this thesis. Not knowing where to start acknowledging the people in my surroundings, let alone know where to end ...

Thank you ...

fishtank
Anneke
Bogdan
Chun-Feng
Eric
Erica
Flavia
Georgios
Γιάννης
Gino
Jamie
Janne
Jonathan
Judith
Katerina
Kenko
Koen
Lars
Lena
Leo
Linda
Mark
Matthew
Mauricio
Michael Ray
Natália
Natasha
Nianlei
Pavlo
Ragnhild
Rawdha
Rick
Teddy
Vikash
Ylenia
Zhen

fancy dining
Costanza
Kirsten
Niko

appreciator
Gavin

art director
Monika

articulator
Christoph

believer
Beatrice

booker
Mauricio

candid
Alessia

chief trickster
Daniel

creative director
Anneke

daily chef
Gabriele

developer
Ebrahim

enthusiast
Giacomo

factotum
Judith

fishtank music
Dr. Jei [144]

good egg
Rogier

ground control
Vahid

guardian
Costanza

hearer
Sabrina

keen eye
Sara

philosopher
Lennart

power(&)plant
Niko

producer
Ylenia

reason's voice
Γιάννης (Giannis)

resonator
Ludovica

rosewater
Mohammad

sage
Chun-Feng

scholar
Hassan

sibyl
Katerina

sleuth

Vikash

slick

Rick

spark

Matthew

stealthy wit

Federica

tough cookie

Kasra

vibes

Edwin

weaver

Kirsten

zest

Konstantinos

shelter

Alessia
Beatrice
Daniel
Federica
Gavin
Hamed
Kasra
Luca
Ludovica
Marin
Rogier
Sabrina
Sara

ventilation

Amir
Mauricio
Mohammad
Sander
Teunis
Yageng

quality of life

Corrina
Imas
Mounir
Zoubir

custodians

Amanda
Angelique
Mariska
Marjolijn
Merel
Sabrina

eclectic

Andrew
Anna
Anton
Bart
Bastiaan
Benjamin
Benjamin
Bob
Bram
Bram
Carlos
Christoph
Daniel
Daniel
Dirk
Ebrahim
Edwin
Elías
Eline
Eline
Emanuele
Esther
Fabian
Françoise
Frédérique
Giacomo
Hassan
Helda

Indra
Ingmar
Ingrid
Jan-Willem
Jelle
Jenna
Jette
Jiahui
Jianxing
Jinlai
Jinne
Jonathan
Juan
Jules
Karen
Karien
Karin
Keyu
Khashayar
Kim
Karl
Konstantinos
Léo
Lorenzo
Lucy
Mahdiyeh
Mahya
Mana
Marco
Maria
Marit
Marta
Martijn
Merle
Michelle
Morteza
Nasim
Nick
Nynke
Pascal
Patricia
Pedro
Peter
Robin
Ronald
Rosanne
Saher
Sara
Sebastien
Shahram
Shibo
Suzanne
Teun
Thomas
Tom
Tomas
Vera
Viola

inspiration

Arend

ip man

Anna
Arjen
Remco

home

Bertus
Femia
Jan
Jeannet
Harry
Tineke
Erik
Kirsten
Wilma
Frank
Wilke
Cornelis (papa)
Jeltje (mama)
Willemke (oma)

Curriculum Vitae

1990 January 23 Born in Sneek, The Netherlands.

2002–2008 Preparatory scientific education at Regionale Scholengemeenschap Magister Alvinus Sneek.

2008–2012 BSc study in Mechanical Engineering at Delft University of Technology.

2012–2017 MSc study in Mechanical Engineering at Delft University of Technology. Graduated at the department of BioMechanical Engineering, Bicycle Laboratory, under the supervision of dr. ir. Arend L. Schwab. Thesis: "Rear Wheel Steer Bikes".

2017–2018 Teaching assistant at Delft University of Technology. Worked on multiple engineering mechanics courses and the book "Advanced Dynamics" by prof Dr.-Ing. Heike Vallery and dr. ir. Arend L. Schwab.

2018–2023 PhD-candidate at Delft University of Technology, department of BioMechanical Engineering, Biomaterials & Tissue Biomechanics, under direction of prof. dr. Amir A. Zadpoor.

2023–present Teacher at Delft University of Technology, department of BioMechanical Engineering.

Publications

- Pier H. de Jong, A. L. Schwab, Mohammad J. Mirzaali, and Amir A. Zadpoor. A multibody kinematic system approach for the design of shape-morphing mechanism-based metamaterials. *Communications Materials*, 2023 [14].

- Pier H. de Jong, Y. Salvatori, F. Libonati, Mohammad J. Mirzaali, and Amir A. Zadpoor. Shape-locking in architected materials through 3D printed magnetically activated joints. *Materials & Design*, 2023 [15].

- Pier H. De Jong, Vahid Moosabeiki, Marius A. Leeflang, Mohammad J. Mirzaali, and Amir A. Zadpoor. Shape morphing of additively manufactured metallic kinematic structures to trace single- and doubly-curved surfaces. *Materials & Design*, 2025 [16].

- Vahid Moosabeiki, Marius A. Leeflang, Jasper G. Gerbers, Pier H. de Jong, Demien Broekhuis, Yash Agarwal, Jagathes N. Ganesen, Bart L. Kaptein, Rob G. H. H. Nelissen, Mohammad J. Mirzaali, and Amir A. Zadpoor. Additively manufactured shape-morphing implants for the treatment of acetabular defects. *Acta Biomaterialia*, 2025. [129].

References

[1] Emilia Irzmańska and Paulina Kropidłowska. Case Study: Fit Evaluation of Protective Gloves Made of Elastic and Non-Elastic Textile Materials. *Fibres and Textiles in Eastern Europe*, 27(5(137)):90–99, October 2019. ISSN 1230-3666. doi: 10.5604/01.3001.0013.2903. URL `https://ftee.com.pl/gicid/01.3001.0013.2903`.

[2] Petra J. Jones, Richard J. Bibb, Melanie J. Davies, Kamlesh Khunti, Matthew McCarthy, Daniel T.P. Fong, and David Webb. A fitting problem: Standardising shoe fit standards to reduce related diabetic foot ulcers. *Diabetes Research and Clinical Practice*, 154:66–74, August 2019. ISSN 01688227. doi: 10.1016/j.diabres.2019.05.017. URL `https://linkinghub.elsevier.com/retrieve/pii/S0168822719306242`.

[3] Soya Eguchi, Yukako Yazaki, Riku Kato, Yusaku Arita, Takumi Moriya, and Hiroya Tanaka. Proto-Chair: Posture-Sensing Smart Furniture with 3D-Printed Auxetics. In *Extended Abstracts of the 2020 CHI Conference on Human Factors in Computing Systems*, pages 1–7, Honolulu HI USA, April 2020. ACM. ISBN 978-1-4503-6819-3. doi: 10.1145/3334480.3383036. URL `https://dl.acm.org/doi/10.1145/3334480.3383036`.

[4] Gabriella E. Smith, Philippe A. Chouinard, and Sarah-Elizabeth Byosiere. If I fits I sits: A citizen science investigation into illusory contour susceptibility in domestic cats (Felis silvestris catus). *Applied Animal Behaviour Science*, 240:105338, July 2021. ISSN 01681591. doi: 10.1016/j.applanim.2021.105338. URL `https://linkinghub.elsevier.com/retrieve/pii/S0168159121001258`.

[5] E. M. Zullinger, R. E. Ricklefs, K. H. Redford, and G. M. Mace. Fitting Sigmoidal Equations to Mammalian Growth Curves. *Journal of Mammalogy*, 65(4):607–636, November 1984. ISSN 1545-1542, 0022-2372. doi: 10.2307/1380844. URL https://academic.oup.com/jmammal/article-lookup/doi/10.2307/1380844.

[6] Yanbin Li, Yao Zhao, Yinding Chi, Yaoye Hong, and Jie Yin. Shape-morphing materials and structures for energy-efficient building envelopes. *Materials Today Energy*, 22:100874, December 2021. ISSN 24686069. doi: 10.1016/j.mtener.2021.100874. URL https://linkinghub.elsevier.com/retrieve/pii/S2468606921002392.

[7] Jens Emil Grønbæk, Henrik Korsgaard, Marianne Graves Petersen, Morten Henriksen Birk, and Peter Gall Krogh. Proxemic Transitions: Designing Shape-Changing Furniture for Informal Meetings. In *Proceedings of the 2017 CHI Conference on Human Factors in Computing Systems*, pages 7029–7041, Denver Colorado USA, May 2017. ACM. ISBN 978-1-4503-4655-9. doi: 10.1145/3025453.3025487. URL https://dl.acm.org/doi/10.1145/3025453.3025487.

[8] S Barbarino, E I Saavedra Flores, R M Ajaj, I Dayyani, and M I Friswell. A review on shape memory alloys with applications to morphing aircraft. *Smart Materials and Structures*, 23(6):063001, June 2014. ISSN 0964-1726, 1361-665X. doi: 10.1088/0964-1726/23/6/063001. URL https://iopscience.iop.org/article/10.1088/0964-1726/23/6/063001.

[9] Luquan Ren, Bingqian Li, Guowu Wei, Kunyang Wang, Zhengyi Song, Yuyang Wei, Lei Ren, and Qingping Liu. Biology and bioinspiration of soft robotics: Actuation, sensing, and system integration. *iScience*, 24(9):103075, September 2021. ISSN 25890042. doi: 10.1016/j.isci.2021.103075. URL https://linkinghub.elsevier.com/retrieve/pii/S2589004221010439.

[10] Rohit Goyal and Santanu Mitra. A Brief Overview of Bioinspired Robust Hydrogel Based Shape Morphing Functional Structure for Biomedical Soft Robotics. *Frontiers in Materials*, 9:837923, April 2022. ISSN 2296-8016. doi: 10.3389/fmats.2022.837923. URL https://www.frontiersin.org/articles/10.3389/fmats.2022.837923/full.

[11] Srinivas Vasista, Olaf Mierheim, and Markus Kintscher. Morphing Structures, Applications of. In Holm Altenbach and Andreas Öchsner, editors, *Encyclopedia of Continuum Mechanics*, pages 1–13. Springer Berlin Heidelberg, Berlin, Heidelberg, 2019. ISBN 978-3-662-53605-6. doi: 10.1007/978-3-662-53605-6_247-1. URL http://link.springer.com/10.1007/978-3-662-53605-6_247-1.

[12] Michel Rautureau, Celso de Sousa Figueiredo Gomes, Nicole Liewig, and Mehrnaz Katouzian-Safadi. Clay and Clay Mineral Definition. In *Clays and Health*, pages 5–31. Springer International Publishing, Cham, 2017. ISBN 978-3-319-42883-3 978-3-319-42884-0. doi: 10.1007/978-3-319-42884-0_2. URL http://link.springer.com/10.1007/978-3-319-42884-0_2.

[13] Sander Leeflang, Shahram Janbaz, and Amir A. Zadpoor. Metallic clay. *Additive Manufacturing*, 28:528–534, August 2019. ISSN 22148604. doi: 10.1016/j.addma.2019.05.032. URL https://linkinghub.elsevier.com/retrieve/pii/S2214860419302027.

[14] Pier H. de Jong, A. L. Schwab, Mohammad J. Mirzaali, and Amir A. Zadpoor. A multibody kinematic system approach for the design of shape-morphing mechanism-based metamaterials. *Communications Materials*, 4(1):83, October 2023. ISSN 2662-4443. doi: 10.1038/s43246-023-00410-2. URL https://www.nature.com/articles/s43246-023-00410-2.

[15] Pier H. de Jong, Y. Salvatori, F. Libonati, Mohammad J. Mirzaali, and Amir A. Zadpoor. Shape-locking in architected materials through 3D printed magnetically activated joints. *Materials & Design*, 235:112427, 2023. ISSN 0264-1275. doi: https://doi.org/10.1016/j.matdes.2023.112427. URL https://www.sciencedirect.com/science/article/pii/S0264127523008420.

[16] Pier H. De Jong, Vahid Moosabeiki, Marius A. Leeflang, Mohammad J. Mirzaali, and Amir A. Zadpoor. Shape morphing of additively manufactured metallic kinematic structures to trace single- and doubly-curved surfaces. *Materials & Design*, 257:114471, September 2025. ISSN 02641275. doi: 10.1016/j.matdes.2025.114471. URL https://linkinghub.elsevier.com/retrieve/pii/S0264127525008913.

[17] Cecilia Laschi, Matteo Cianchetti, Barbara Mazzolai, Laura Marghe-ri, Maurizio Follador, and Paolo Dario. Soft Robot Arm Inspired by the Octopus. *Advanced Robotics*, 26(7):709–727, January 2012. ISSN 0169-1864, 1568-5535. doi: 10.1163/156855312X626343. URL https://www.tandfonline.com/doi/full/10.1163/156855312X626343.

[18] Alexander G. Volkov, editor. *Plant Electrophysiology*. Springer Berlin Heidelberg, Berlin, Heidelberg, 2012. ISBN 978-3-642-29109-8 978-3-642-29110-4. doi: 10.1007/978-3-642-29110-4. URL http://link.springer.com/10.1007/978-3-642-29110-4.

[19] André R. Studart and Randall M. Erb. Bioinspired materials that self-shape through programmed microstructures. *Soft Matter*, 10(9):1284–1294, 2014. ISSN 1744-683X, 1744-6848. doi: 10.1039/C3SM51883C. URL http://xlink.rsc.org/?DOI=C3SM51883C.

[20] Kate Oliver, Annela Seddon, and Richard S. Trask. Morphing in nature and beyond: a review of natural and synthetic shape-changing materials and mechanisms. *Journal of Materials Science*, 51(24):10663–10689, December 2016. ISSN 0022-2461, 1573-4803. doi: 10.1007/s10853-016-0295-8. URL http://link.springer.com/10.1007/s10853-016-0295-8.

[21] Julian K. A. Langowski, Dimitra Dodou, Marleen Kamperman, and Johan L. van Leeuwen. Tree frog attachment: mechanisms, challenges, and perspectives. *Frontiers in Zoology*, 15(1):32, December 2018. ISSN 1742-9994. doi: 10.1186/s12983-018-0273-x. URL https://frontiersinzoology.biomedcentral.com/articles/10.1186/s12983-018-0273-x.

[22] Simon Poppinga, David Correa, Bernd Bruchmann, Achim Menges, and Thomas Speck. Plant Movements as Concept Generators for the Development of Biomimetic Compliant Mechanisms. *Integrative and Comparative Biology*, 60(4):886–895, October 2020. ISSN 1540-7063, 1557-7023. doi: 10.1093/icb/icaa028. URL https://academic.oup.com/icb/article/60/4/886/5836308.

[23] Luquan Ren, Bingqian Li, Kunyang Wang, Xueli Zhou, Zhengyi Song, Lei Ren, and Qingping Liu. Plant-Morphing Strategies and Plant-Inspired Soft Actuators Fabricated by Biomimetic Four-Dimensional Printing: A Review. *Frontiers in Materials*, 8:651521, May 2021. ISSN 2296-8016. doi: 10.3389/fmats.2021.651521. URL https://www.frontiersin.org/articles/10.3389/fmats.2021.651521/full.

[24] Francesco Fiorito, Michele Sauchelli, Diego Arroyo, Marco Pesenti, Marco Imperadori, Gabriele Masera, and Gianluca Ranzi. Shape morphing solar shadings: A review. *Renewable and Sustainable Energy Reviews*, 55:863–884, March 2016. ISSN 13640321. doi: 10.1016/j.rser.2015.10.086. URL https://linkinghub.elsevier.com/retrieve/pii/S136403211501165X.

[25] Gyouhyung Kyung and Maury A. Nussbaum. Driver sitting comfort and discomfort (part II): Relationships with and prediction from interface pressure. *International Journal of Industrial Ergonomics*, 38(5-6):526–538, May 2008. ISSN 01698141. doi: 10.1016/j.ergon.2007.08.011. URL https://linkinghub.elsevier.com/retrieve/pii/S016981410700159X.

[26] Stephen Daynes and Paul M Weaver. Review of shape-morphing automobile structures: concepts and outlook. *Proceedings of the Institution of Mechanical Engineers, Part D: Journal of Automobile Engineering*, 227(11):1603–1622, November 2013. ISSN 0954-4070, 2041-2991. doi: 10.1177/0954407013496557. URL http://journals.sagepub.com/doi/10.1177/0954407013496557.

[27] M. J. Mirzaali, S. Janbaz, M. Strano, L. Vergani, and A. A. Zadpoor. Shape-matching soft mechanical metamaterials. *Scientific Reports*, 8(1):965, December 2018. ISSN 2045-2322. doi: 10.1038/s41598-018-19381-3. URL http://www.nature.com/articles/s41598-018-19381-3.

[28] Yanbin Li and Jie Yin. Metamorphosis of three-dimensional kirigami-inspired reconfigurable and reprogrammable architected matter. *Materials Today Physics*, 21:100511, November 2021. ISSN 25425293. doi: 10.1016/j.mtphys.2021.100511. URL https://linkinghub.elsevier.com/retrieve/pii/S2542529321001723.

[29] Ying Liu, Jan Genzer, and Michael D. Dickey. "2D or not 2D": Shape-programming polymer sheets. *Progress in Polymer Science*, 52:79–106, January 2016. ISSN 00796700. doi: 10.1016/j.progpolymsci.2015.09.001. URL https://linkinghub.elsevier.com/retrieve/pii/S0079670015001021.

[30] Jifei Ou, Zhao Ma, Jannik Peters, Sen Dai, Nikolaos Vlavianos, and Hiroshi Ishii. Kinetix - designing auxetic-inspired deformable material structures. *Computers & Graphics*, 75:72 – 81, 2018. ISSN 0097-8493. doi: https://doi.org/10.1016/j.cag.2018.06.003. URL http://www.sciencedirect.com/science/article/pii/S0097849318301006.

[31] Majid Hojjat, Electra Stavropoulou, and Kai-Uwe Bletzinger. The Vertex Morphing method for node-based shape optimization. *Computer Methods in Applied Mechanics and Engineering*, 268:494–513, January 2014. ISSN 00457825. doi: 10.1016/j.cma.2013.10.015. URL https://linkinghub.elsevier.com/retrieve/pii/S0045782513002673.

[32] Franz-Josef Ertl, Guido Dhondt, and Kai-Uwe Bletzinger. Vertex assigned morphing for parameter free shape optimization of 3-dimensional solid structures. *Computer Methods in Applied Mechanics and Engineering*, 353:86–106, August 2019. ISSN 00457825. doi: 10.1016/j.cma.2019.05.004. URL https://linkinghub.elsevier.com/retrieve/pii/S0045782519302634.

[33] N. Vu-Bac, T.X. Duong, T. Lahmer, P. Areias, R.A. Sauer, H.S. Park, and T. Rabczuk. A NURBS-based inverse analysis of thermal expansion induced morphing of thin shells. *Computer Methods in Applied Mechanics and Engineering*, 350:480–510, June 2019. ISSN 00457825. doi: 10.1016/j.cma.2019.03.011. URL https://linkinghub.elsevier.com/retrieve/pii/S0045782519301409.

[34] N. Vu-Bac, T. Rabczuk, H.S. Park, X. Fu, and X. Zhuang. A NURBS-based inverse analysis of swelling induced morphing of thin stimuli-responsive polymer gels. *Computer Methods in Applied Mechanics and Engineering*, 397:115049, July 2022. ISSN 00457825. doi: 10.1016/j.cma.2022.115049. URL https://linkinghub.elsevier.com/retrieve/pii/S004578252200264X.

[35] C M Gosselin and D Gagnon-Lachance. Expandable Polyhedral Mechanisms Based on Polygonal One-Degree-of-Freedom Faces. *Proceedings of the Institution of Mechanical Engineers, Part C: Journal of Mechanical Engineering Science*, 220(7):1011–1018, July 2006. ISSN 0954-4062, 2041-2983. doi: 10.1243/09544062JMES174. URL http://journals.sagepub.com/doi/10.1243/09544062JMES174.

[36] Tomohiro Tachi. Simulation of Rigid Origami. In *Origami4: Fourth International Meeting of Origami Science, Mathematics, and Education*, pages 175–187. A K Peters, Ltd., 2009.

[37] Gökhan Kiper and Eres Söylemez. Homothetic Jitterbug-like linkages. *Mechanism and Machine Theory*, 51:145–158, May 2012. ISSN 0094114X. doi: 10.1016/j.mechmachtheory.2011.11.014. URL https://linkinghub.elsevier.com/retrieve/pii/S0094114X11002321.

[38] Bernhard Thomaszewski, Stelian Coros, Damien Gauge, Vittorio Megaro, Eitan Grinspun, and Markus Gross. Computational design of linkage-based characters. *ACM Transactions on Graphics*, 33(4): 1–9, July 2014. ISSN 0730-0301, 1557-7368. doi: 10.1145/2601097.2601143. URL https://dl.acm.org/doi/10.1145/2601097.2601143.

[39] Ruiming Li, Yan-an Yao, and Xianwen Kong. Reconfigurable deployable polyhedral mechanism based on extended parallelogram mechanism. *Mechanism and Machine Theory*, 116:467–480, October 2017. ISSN 0094114X. doi: 10.1016/j.mechmachtheory.2017.06.014. URL https://linkinghub.elsevier.com/retrieve/pii/S0094114X17301672.

[40] Yucai Hu and Haiyi Liang. Folding simulation of rigid origami with Lagrange multiplier method. *International Journal of Solids and Structures*, 202:552–561, October 2020. ISSN 00207683. doi: 10.1016/j.ijsolstr.2020.06.016. URL https://linkinghub.elsevier.com/retrieve/pii/S0020768320302389.

[41] Ying Gao, Xingyu Wei, Xingkai Han, Zhengong Zhou, and Jian Xiong. Novel 3D auxetic lattice structures developed based on the rotating rigid mechanism. *International Journal of Solids and Structures*, 233:111232, December 2021. ISSN 00207683. doi: 10.1016/j.ijsolstr.2021.111232. URL https://linkinghub.elsevier.com/retrieve/pii/S0020768321003206.

[42] A. L. Schwab and J. P. Meijaard. How to Draw Euler Angles and Utilize Euler Parameters. In *Volume 2: 30th Annual Mechanisms and Robotics Conference, Parts A and B*, pages 259–265, Philadelphia, Pennsylvania, USA, January 2006. ASMEDC. ISBN 978-0-7918-4256-0 978-0-7918-3784-9. doi: 10.1115/DETC2006-99307. URL https://asmedigitalcollection.asme.org/IDETC-CIE/proceedings/IDETC-CIE2006/42568/259/318134.

[43] P.J. Besl and Neil D. McKay. A method for registration of 3-D shapes. *IEEE Transactions on Pattern Analysis and Machine Intelligence*, 14(2):239–256, February 1992. ISSN 0162-8828, 2160-9292. doi: 10.1109/34.121791. URL http://ieeexplore.ieee.org/document/121791/.

[44] R.C. Veltkamp. Shape matching: similarity measures and algorithms. In *Proceedings International Conference on Shape Modeling and Applications*, pages 188–197, Genova, Italy, 2001. IEEE Computer Society. ISBN 978-0-7695-0853-5. doi: 10.1109/SMA.2001.923389. URL http://ieeexplore.ieee.org/document/923389/.

[45] S. Belongie, J. Malik, and J. Puzicha. Shape matching and object recognition using shape contexts. *IEEE Transactions on Pattern Analysis and Machine Intelligence*, 24(4):509–522, April 2002. ISSN 01628828. doi: 10.1109/34.993558. URL http://ieeexplore.ieee.org/document/993558/.

[46] J. García de Jalón, J. Unda, A. Avello, and J. M. Jiménez. Dynamic Analysis of Three-Dimensional Mechanisms in "Natural" Coordinates. *Journal of Mechanisms, Transmissions, and Automation in Design*, 109(4):460–465, December 1987. ISSN 0738-0666. doi: 10.1115/1.3258818. URL https://asmedigitalcollection.asme.org/mechanicaldesign/article/109/4/460/435112/Dynamic-Analysis-of-ThreeDimensional-Mechanisms-in.

[47] Parviz E. Nikravesh and Hazem A. Affifi. Construction of the Equations of Motion for Multibody Dynamics Using Point and Joint Coordinates. In Manuel F. O. Seabra Pereira and Jorge A. C. Ambrósio, editors, *Computer-Aided Analysis of Rigid and Flexible Mechanical Systems*, pages 31–60. Springer Netherlands, Dordrecht, 1994. ISBN 978-94-010-4508-7 978-94-011-1166-9. doi: 10.1007/978-94-011-1166-9_2. URL http://link.springer.com/10.1007/978-94-011-1166-9_2.

[48] Javier García de Jalón and Eduardo Bayo. *Kinematic and Dynamic Simulation of Multibody Systems: The Real-Time Challenge*. Mechanical Engineering Series. Springer New York, New York, NY, 1994. ISBN 978-1-4612-7601-2 978-1-4612-2600-0. doi: 10.1007/978-1-4612-2600-0. URL http://link.springer.com/10.1007/978-1-4612-2600-0.

[49] Hazem Ali Attia. Dynamic modelling of planar mechanisms using point coordinates. *KSME International Journal*, 17(12):1977–1985, December 2003. ISSN 1226-4865. doi: 10.1007/BF02982437. URL http://link.springer.com/10.1007/BF02982437.

[50] P. E. Nikravesh. An Overview of Several Formulations for Multibody Dynamics. In Doru Talabă and Thomas Roche, editors, *Product Engineering*, pages 189–226. Kluwer Academic Publishers, Dordrecht, 2005. ISBN 978-1-4020-2932-5. doi: 10.1007/1-4020-2933-0_13. URL http://link.springer.com/10.1007/1-4020-2933-0_13.

[51] ISO and ASTM. 52900 Additive manufacturing - General principles - Fundamentals and vocabulary, November 2021.

[52] Daniel Melanz, Luning Fang, Paramsothy Jayakumar, and Dan Negrut. A comparison of numerical methods for solving multibody dynamics problems with frictional contact modeled via differential variational inequalities. *Computer Methods in Applied Mechanics and Engineering*, 320:668–693, June 2017. ISSN 00457825. doi: 10.1016/j.cma.2017.03.010. URL https://linkinghub.elsevier.com/retrieve/pii/S0045782516317005.

[53] Alfredo Gay Neto. Framework for automatic contact detection in a multibody system. *Computer Methods in Applied Mechanics and Engineering*, 403:115703, January 2023. ISSN 00457825. doi: 10.1016/j.cma.2022.115703. URL https://linkinghub.elsevier.com/retrieve/pii/S0045782522006582.

[54] Lucas A. Shaw and Jonathan B. Hopkins. An actively controlled shape-morphing compliant microarchitectured material. *Journal of Mechanisms and Robotics*, 8(2):021019–1–021019–10, 11 2015. doi: 10.1115/1.4031168. URL http://dx.doi.org/10.1115/1.4031168.

[55] D.P. Huttenlocher, G.A. Klanderman, and W.J. Rucklidge. Comparing images using the Hausdorff distance. *IEEE Transactions on Pattern Analysis and Machine Intelligence*, 15(9):850–863, September 1993. ISSN 01628828. doi: 10.1109/34.232073. URL http://ieeexplore.ieee.org/document/232073/.

[56] Henri Poincaré. Sur les courbes définies par les équations différentielles. (III). *Journal de mathématiques pures et appliquées*, 1(4):167–244, 1885. URL http://sites.mathdoc.fr/JMPA/PDF/JMPA_1885_4_1_A6_0.pdf.

[57] Helena M. A. Kolken, Shahram Janbaz, Sander M. A. Leeflang, Karel Lietaert, Harrie H. Weinans, and Amir A. Zadpoor. Rationally designed meta-implants: a combination of auxetic and conventional meta-biomaterials. *Materials Horizons*, 5(1):28–35, 2018. ISSN 2051-6347, 2051-6355. doi: 10.1039/C7MH00699C. URL http://xlink.rsc.org/?DOI=C7MH00699C.

[58] Alan Francisco Pérez Vidal, Jesse Yoe Rumbo Morales, Gerardo Ortiz Torres, Felipe de Jesús Sorcia Vázquez, Alan Cruz Rojas, Jorge Aurelio Brizuela Mendoza, and Julio César Rodríguez Cerda. Soft Exoskeletons: Development, Requirements, and Challenges of the Last Decade. *Actuators*, 10(7):166, July 2021. ISSN 2076-0825. doi: 10.3390/act10070166. URL https://www.mdpi.com/2076-0825/10/7/166.

[59] Jun Shintake, Vito Cacucciolo, Dario Floreano, and Herbert Shea. Soft Robotic Grippers. *Advanced Materials*, 30(29):1707035, July 2018. ISSN 09359648. doi: 10.1002/adma.201707035. URL https://onlinelibrary.wiley.com/doi/10.1002/adma.201707035.

[60] T. Ashuri, A. Armani, R. Jalilzadeh Hamidi, T. Reasnor, S. Ahmadi, and K. Iqbal. Biomedical soft robots: current status and perspective. *Biomedical Engineering Letters*, 10(3):369–385, August 2020. ISSN 2093-9868, 2093-985X. doi: 10.1007/s13534-020-00157-6. URL https://link.springer.com/10.1007/s13534-020-00157-6.

[61] Nazek El-Atab, Rishabh B. Mishra, Fhad Al-Modaf, Lana Joharji, Aljohara A. Alsharif, Haneen Alamoudi, Marlon Diaz, Nadeem Qaiser, and Muhammad Mustafa Hussain. Soft Actuators for Soft Robotic Applications: A Review. *Advanced Intelligent Systems*, 2(10):2000128, October 2020. ISSN 2640-4567, 2640-4567. doi: 10.1002/aisy.202000128. URL https://onlinelibrary.wiley.com/doi/10.1002/aisy.202000128.

[62] Faheem Ahmed, Muhammad Waqas, Bushra Jawed, Afaque Manzoor Soomro, Suresh Kumar, Ashraf Hina, Umair Khan, Kyung Hwan Kim, and Kyung Hyun Choi. Decade of bio-inspired soft robots: a review. *Smart Materials and Structures*, 31(7):073002, July 2022. ISSN 0964-1726, 1361-665X. doi: 10.1088/1361-665X/ac6e15. URL https://iopscience.iop.org/article/10.1088/1361-665X/ac6e15.

[63] Soroush Kamrava, Davood Mousanezhad, Hamid Ebrahimi, Ranajay Ghosh, and Ashkan Vaziri. Origami-based cellular metamaterial with auxetic, bistable, and self-locking properties. *Scientific Reports*, 7(1):46046, April 2017. ISSN 2045-2322. doi: 10.1038/srep46046. URL https://www.nature.com/articles/srep46046.

[64] Jason Troutner, Ashley Sue Moy, Andrew Steveson, Abhliash Seshadri, Ethan Wisniewski, Brittany Lung, Kendall Furbee, and Veronica Andrea Hogg-Cornejo. Orthopedic support apparatus and method of use, June 2018. URL https://patents.google.com/patent/US20180153745A1/en.

[65] Randall M. Erb, Jonathan S. Sander, Roman Grisch, and André R. Studart. Self-shaping composites with programmable bioinspired microstructures. *Nature Communications*, 4(1):1712, June 2013. ISSN 2041-1723. doi: 10.1038/ncomms2666. URL http://www.nature.com/articles/ncomms2666.

[66] Marc Behl, Karl Kratz, Jörg Zotzmann, Ulrich Nöchel, and Andreas Lendlein. Reversible Bidirectional Shape-Memory Polymers. *Advanced Materials*, 25(32):4466–4469, August 2013. ISSN 09359648. doi: 10.1002/adma.201300880. URL https://onlinelibrary.wiley.com/doi/10.1002/adma.201300880.

[67] Jiangtao Wu, Chao Yuan, Zhen Ding, Michael Isakov, Yiqi Mao, Tiejun Wang, Martin L. Dunn, and H. Jerry Qi. Multi-shape active composites by 3D printing of digital shape memory polymers. *Scientific Reports*, 6(1):24224, July 2016. ISSN 2045-2322. doi: 10.1038/srep24224. URL http://www.nature.com/articles/srep24224.

[68] Hongqiu Wei, Qiwei Zhang, Yongtao Yao, Liwu Liu, Yanju Liu, and Jinsong Leng. Direct-Write Fabrication of 4D Active Shape-Changing Structures Based on a Shape Memory Polymer and Its Nanocomposite. *ACS Applied Materials & Interfaces*, 9(1):876–883, January 2017. ISSN 1944-8244, 1944-8252. doi: 10.1021/acsami.6b12824. URL https://pubs.acs.org/doi/10.1021/acsami.6b12824.

[69] Teunis van Manen, Shahram Janbaz, and Amir A. Zadpoor. Programming 2D/3D shape-shifting with hobbyist 3D printers. *Materials Horizons*, 4(6):1064–1069, 2017. ISSN 2051-6347, 2051-6355. doi: 10.1039/C7MH00269F. URL http://xlink.rsc.org/?DOI=C7MH00269F.

[70] Xiaolong Chen, Xinhua Liu, Mengzheng Ouyang, Jingyi Chen, Oluwadamilola Taiwo, Yuhua Xia, Peter R. N. Childs, Nigel P. Brandon, and Billy Wu. Multi-metal 4D printing with a desktop electrochemical 3D printer. *Scientific Reports*, 9(1):3973, March 2019. ISSN 2045-2322. doi: 10.1038/s41598-019-40774-5. URL https://www.nature.com/articles/s41598-019-40774-5.

[71] Mehrshad Mehrpouya, Henri Vahabi, Shahram Janbaz, Arash Darafsheh, Thomas R. Mazur, and Seeram Ramakrishna. 4D printing of shape memory polylactic acid (PLA). *Polymer*, 230:124080, September 2021. ISSN 00323861. doi: 10.1016/j.polymer.2021.124080. URL https://linkinghub.elsevier.com/retrieve/pii/S0032386121007035.

[72] Teunis van Manen, Shahram Janbaz, Kaspar M. B. Jansen, and Amir A. Zadpoor. 4D printing of reconfigurable metamaterials and devices. *Communications Materials*, 2(1):56, June 2021. ISSN 2662-4443. doi: 10.1038/s43246-021-00165-8. URL https://www.nature.com/articles/s43246-021-00165-8.

[73] Benjamin Gorissen, Dominiek Reynaerts, Satoshi Konishi, Kazuhiro Yoshida, Joon-Wan Kim, and Michael De Volder. Elastic Inflatable Actuators for Soft Robotic Applications. *Advanced Materials*, 29 (43):1604977, November 2017. ISSN 09359648. doi: 10.1002/adma.201604977. URL https://onlinelibrary.wiley.com/doi/10.1002/adma.201604977.

[74] Eric Diller, Jiang Zhuang, Guo Zhan Lum, Matthew R. Edwards, and Metin Sitti. Continuously distributed magnetization profile for millimeter-scale elastomeric undulatory swimming. *Applied Physics Letters*, 104(17):174101, April 2014. ISSN 0003-6951, 1077-3118. doi: 10.1063/1.4874306. URL http://aip.scitation.org/doi/10.1063/1.4874306.

[75] Guo Zhan Lum, Zhou Ye, Xiaoguang Dong, Hamid Marvi, Onder Erin, Wenqi Hu, and Metin Sitti. Shape-programmable magnetic soft matter. *Proceedings of the National Academy of Sciences*, 113 (41), October 2016. ISSN 0027-8424, 1091-6490. doi: 10.1073/pnas.1608193113. URL https://pnas.org/doi/full/10.1073/pnas.1608193113.

[76] Yoonho Kim, Hyunwoo Yuk, Ruike Zhao, Shawn A. Chester, and Xuanhe Zhao. Printing ferromagnetic domains for untethered fast-transforming soft materials. *Nature*, 558(7709):274–279, June 2018. ISSN 0028-0836, 1476-4687. doi: 10.1038/s41586-018-0185-0. URL http://www.nature.com/articles/s41586-018-0185-0.

[77] Tiegang Chen, Xiaoyong Zhang, Xiaojun Yan, Bin Zhang, Jun Jiang, Dawei Huang, Mingjing Qi, and Ruijie Sun. Harnessing Magnets to Design Tunable Architected Bistable Material. *Advanced Engineering Materials*, 21(3):1801255, March 2019. ISSN 14381656. doi: 10.1002/adem.201801255. URL https://onlinelibrary.wiley.com/doi/10.1002/adem.201801255.

[78] Yunus Alapan, Alp C. Karacakol, Seyda N. Guzelhan, Irem Isik, and Metin Sitti. Reprogrammable shape morphing of magnetic soft machines. *Science Advances*, 6(38):eabc6414, September 2020. ISSN 2375-2548. doi: 10.1126/sciadv.abc6414. URL https://www.science.org/doi/10.1126/sciadv.abc6414.

[79] Xu Wang, Guoyong Mao, Jin Ge, Michael Drack, Gilbert Santiago Cañón Bermúdez, Daniela Wirthl, Rico Illing, Tobias Kosub, Lothar Bischoff, Changan Wang, Jürgen Fassbender, Martin Kaltenbrunner, and Denys Makarov. Untethered and ultrafast soft-bodied robots. *Communications Materials*, 1(1):67, September 2020. ISSN 2662-4443. doi: 10.1038/s43246-020-00067-1. URL https://www.nature.com/articles/s43246-020-00067-1.

[80] Sanne J. M. van Vilsteren, Hooman Yarmand, and Sepideh Ghodrat. Review of Magnetic Shape Memory Polymers and Magnetic Soft Materials. *Magnetochemistry*, 7(9):123, September 2021. ISSN 2312-7481. doi: 10.3390/magnetochemistry7090123. URL https://www.mdpi.com/2312-7481/7/9/123.

[81] Anil K. Bastola and Mokarram Hossain. The shape – morphing performance of magnetoactive soft materials. *Materials & Design*, 211:110172, December 2021. ISSN 02641275. doi: 10.1016/j.matdes.2021.110172. URL https://linkinghub.elsevier.com/retrieve/pii/S0264127521007279.

[82] Krishnaja G and Balasubramanian Kandasubramanian. Exertions of magnetic polymer composites fabricated via 3d printing. *Industrial & Engineering Chemistry Research*, 61(46):16895–16909, 2022. doi: 10.1021/acs.iecr.2c02299. URL https://doi.org/10.1021/acs.iecr.2c02299.

[83] Qiqiang Hu, Hanjin Huang, Erbao Dong, and Dong Sun. A Bioinspired Composite Finger With Self-Locking Joints. *IEEE Robotics and Automation Letters*, 6(2):1391–1398, April 2021. ISSN 2377-3766, 2377-3774. doi: 10.1109/LRA.2021.3056345. URL https://ieeexplore.ieee.org/document/9345370/.

[84] Adam T. Clare, Paul R. Chalker, Sean Davies, Christopher J. Sutcliffe, and Sozos Tsopanos. Selective laser melting of high aspect ratio 3D nickel–titanium structures two way trained for MEMS applications. *International Journal of Mechanics and Materials in Design*, 4(2):181–187, June 2008. ISSN 1569-1713, 1573-8841. doi: 10.1007/s10999-007-9032-4. URL http://link.springer.com/10.1007/s10999-007-9032-4.

[85] Jingda Tang, Zongfei Tong, Yukun Xia, Ming Liu, Zengyao Lv, Yang Gao, Tongqing Lu, Shejuan Xie, Yongmao Pei, Daining Fang, and T. J. Wang. Super tough magnetic hydrogels for remotely triggered shape morphing. *Journal of Materials Chemistry B*, 6(18):2713–2722, 2018. ISSN 2050-750X, 2050-7518. doi: 10.1039/C8TB00568K. URL http://xlink.rsc.org/?DOI=C8TB00568K.

[86] Jingda Tang, Qianfeng Yin, Yancheng Qiao, and Tiejun Wang. Shape Morphing of Hydrogels in Alternating Magnetic Field. *ACS Applied Materials & Interfaces*, 11(23):21194–21200, June 2019. ISSN 1944-8244, 1944-8252. doi: 10.1021/acsami.9b05742. URL https://pubs.acs.org/doi/10.1021/acsami.9b05742.

[87] Deok Gyoon Chung, Joonhwan Kim, DongHoon Baek, Joonyeong Kim, and Dong-Soo Kwon. Shape-Locking Mechanism of Flexible Joint Using Mechanical Latch With Electromagnetic Force. *IEEE Robotics and Automation Letters*, 4(3):2661–2668, July 2019. ISSN 2377-3766, 2377-3774. doi: 10.1109/LRA.2019.2897006. URL https://ieeexplore.ieee.org/document/8632705/.

[88] Amelia Yilin Lee, Jia An, and Chee Kai Chua. Two-Way 4D Printing: A Review on the Reversibility of 3D-Printed Shape Memory Materials. *Engineering*, 3(5):663–674, October 2017. ISSN 20958099. doi: 10.1016/J.ENG.2017.05.014. URL https://linkinghub.elsevier.com/retrieve/pii/S209580991730718X.

[89] Michiel Plooij, Glenn Mathijssen, Pierre Cherelle, Dirk Lefeber, and Bram Vanderborght. Lock Your Robot: A Review of Locking Devices in Robotics. *IEEE Robotics & Automation Magazine*, 22(1):106–117, March 2015. ISSN 1070-9932. doi: 10.1109/MRA.2014.2381368. URL http://ieeexplore.ieee.org/document/7059366/.

[90] Katia Bertoldi, Vincenzo Vitelli, Johan Christensen, and Martin van Hecke. Flexible mechanical metamaterials. *Nature Reviews Materials*, 2(11):17066, November 2017. ISSN 2058-8437. doi: 10.1038/natrevmats.2017.66. URL http://www.nature.com/articles/natrevmats201766.

[91] Ali Valipour, Mohammad H Kargozarfard, Mina Rakhshi, Amin Yaghootian, and Hamid M Sedighi. Metamaterials and their applications: An overview. *Proceedings of the Institution of Mechanical Engineers, Part L: Journal of Materials: Design and Applications*, page 146442072199585, March 2021. ISSN 1464-4207, 2041-3076. doi: 10.1177/1464420721995858. URL http://journals.sagepub.com/doi/10.1177/1464420721995858.

[92] F. S. L. Bobbert, S. Janbaz, and A. A. Zadpoor. Towards deployable meta-implants. *Journal of Materials Chemistry B*, 6(21):3449–3455, 2018. ISSN 2050-750X, 2050-7518. doi: 10.1039/C8TB00576A. URL http://xlink.rsc.org/?DOI=C8TB00576A.

[93] M. A. Leeflang, F. S. L. Bobbert, and A. A. Zadpoor. Additive manufacturing of non-assembly deployable mechanisms for the treatment of large bony defects. *Additive Manufacturing*, 46:102194, October 2021. ISSN 22148604. doi: 10.1016/j.addma.2021.102194. URL https://linkinghub.elsevier.com/retrieve/pii/S2214860421003560.

[94] Kirsten Lussenburg, Aimée Sakes, and Paul Breedveld. Design of non-assembly mechanisms: A state-of-the-art review. *Additive Manufacturing*, 39:101846, March 2021. ISSN 22148604. doi: 10.1016/j.addma.2021.101846. URL https://linkinghub.elsevier.com/retrieve/pii/S2214860421000117.

[95] Jens Wittenburg. *Kinematics*. Springer Berlin Heidelberg, Berlin, Heidelberg, 2016. ISBN 978-3-662-48486-9 978-3-662-48487-6. doi: 10.1007/978-3-662-48487-6. URL http://link.springer.com/10.1007/978-3-662-48487-6.

[96] ISO. 80000-1 Quantities and units - Part 1: General, December 2022.

[97] N. E. Putra, K. G. N. Borg, P. J. Díaz-Payno, M. A. Leeflang, M. Klimopoulou, P. Taheri, J. M. C. Mol, L. E. Fratila-Apachitei, Z. Huan, J. Chang, J. Zhou, and A. A. Zadpoor. Additive manufacturing of bioactive and biodegradable porous iron-akermanite composites for bone regeneration. *Acta Biomaterialia*, 148:355–373, August 2022. ISSN 17427061. doi: 10.1016/j.actbio.2022.06.009. URL https://linkinghub.elsevier.com/retrieve/pii/S1742706122003488.

[98] N.E. Putra, A. Tigrine, S. Aksakal, V.R. de la Rosa, P. Taheri, L.E. Fratila-Apachitei, J.M.C. Mol, J. Zhou, and A.A. Zadpoor. Poly(2-ethyl-2-oxazoline) coating of additively manufactured biodegradable porous iron. *Biomaterials Advances*, 133:112617, February 2022. ISSN 27729508. doi: 10.1016/j.msec.2021.112617. URL https://linkinghub.elsevier.com/retrieve/pii/S0928493121007578.

[99] Xiangxia Wei, Ming-Liang Jin, Haiqiang Yang, Xiao-Xiong Wang, Yun-Ze Long, and Zhangwei Chen. Advances in 3D printing of magnetic materials: Fabrication, properties, and their applications. *Journal of Advanced Ceramics*, 11(5):665–701, May 2022. ISSN 2226-4108, 2227-8508. doi: 10.1007/s40145-022-0567-5. URL https://link.springer.com/10.1007/s40145-022-0567-5.

[100] Ellen T. Roche, Markus A. Horvath, Isaac Wamala, Ali Alazmani, Sang-Eun Song, William Whyte, Zurab Machaidze, Christopher J. Payne, James C. Weaver, Gregory Fishbein, Joseph Kuebler, Nikolay V. Vasilyev, David J. Mooney, Frank A. Pigula, and Conor J. Walsh. Soft robotic sleeve supports heart function. *Science Translational Medicine*, 9(373):eaaf3925, January 2017. ISSN 1946-6234, 1946-6242. doi: 10.1126/scitranslmed.aaf3925. URL https://www.science.org/doi/10.1126/scitranslmed.aaf3925.

[101] Thomas S. Lumpe and Kristina Shea. Computational Design of Multi-State Lattice Structures With Finite Mechanisms for Shape Morphing. *Journal of Mechanical Design*, 145(7):071701, July 2023. ISSN 1050-0472, 1528-9001. doi: 10.1115/1.4056928. URL https://asmedigitalcollection.asme.org/mechanicaldesign/article/145/7/071701/1159634/Computational-Design-of-Multi-State-Lattice.

[102] Xudong Yang, Yuan Zhou, Huichan Zhao, Weicheng Huang, Yifan Wang, K. Jimmy Hsia, and Mingchao Liu. Morphing matter: from mechanical principles to robotic applications. *Soft Science*, 3(4), November 2023. ISSN 2769-5441. doi: 10.20517/ss.2023.42. URL https://www.oaepublish.com/articles/ss.2023.42. Publisher: OAE Publishing Inc.

[103] Jian Sun, Qinghua Guan, Yanju Liu, and Jinsong Leng. Morphing aircraft based on smart materials and structures: A state-of-the-art review. *Journal of Intelligent Material Systems and Structures*, 27 (17):2289–2312, October 2016. ISSN 1045-389X, 1530-8138. doi: 10.1177/1045389X16629569. URL https://journals.sagepub.com/doi/10.1177/1045389X16629569.

[104] Aniello Riccio, Andrea Sellitto, and Miriam Battaglia. Morphing Spoiler for Adaptive Aerodynamics by Shape Memory Alloys. *Actuators*, 13(9):330, September 2024. ISSN 2076-0825. doi: 10.3390/act13090330. URL https://www.mdpi.com/2076-0825/13/9/330.

[105] Robert J. Morrison, Scott J. Hollister, Matthew F. Niedner, Maryam Ghadimi Mahani, Albert H. Park, Deepak K. Mehta, Richard G. Ohye, and Glenn E. Green. Mitigation of tracheobronchomalacia with 3D-printed personalized medical devices in pediatric patients. *Science Translational Medicine*, 7(285), April 2015. ISSN 1946-6234, 1946-6242. doi: 10.1126/scitranslmed.3010825. URL https://www.science.org/doi/10.1126/scitranslmed.3010825.

[106] Jack M Haglin, Adam E M Eltorai, Joseph A Gil, Stephen E Marcaccio, Juliana Botero-Hincapie, and Alan H Daniels. Patient-Specific Orthopaedic Implants. *Orthopaedic Surgery*, 8(4):417–424, November 2016. ISSN 1757-7853, 1757-7861. doi: 10.1111/os.12282. URL https://onlinelibrary.wiley.com/doi/10.1111/os.12282.

[107] Kwok Chuen Wong. 3D-printed patient-specific applications in orthopedics. *Orthopedic Research and Reviews*, Volume 8:57–66, October 2016. ISSN 1179-1462. doi: 10.2147/ORR.S99614. URL https://www.dovepress.com/3d-printed-patient-specific-applications-in-orthopedics-peer-reviewed-article-ORR.

[108] Tsung-yen Hsieh, Raj Dedhia, Brian Cervenka, and Travis T. Tollefson. 3D Printing: current use in facial plastic and reconstructive surgery. *Current Opinion in Otolaryngology & Head & Neck Surgery*, 25(4):291–299, August 2017. ISSN 1068-9508, 1531-6998. doi: 10.1097/MOO.0000000000000373. URL https://journals.lww.com/00020840-201708000-00008.

[109] Israel Valverde, Gorka Gomez-Ciriza, Tarique Hussain, Cristina Suarez Mejias, Maria N. Velasco-Forte, Nicholas Byrne, Antonio Ordoñez, Antonio Gonzalez-Calle, David Anderson, Mark G. Hazekamp, Arno A. W. Roest, Jose Rivas-Gonzalez, Sergio Uribe, Issam El-Rassi, John Simpson, Owen Miller, Enrique Ruiz, Ignacio Zabala, Ana Mendez, Begoña Manso, Pastora Gallego, Freddy Prada, Massimiliano Cantinotti, Lamia Ait-Ali, Carlos Merino, Andrew Parry, Nancy Poirier, Gerald Greil, Reza Razavi, Tomas Gomez-Cia, and Amir-Reza Hosseinpour. Three-dimensional printed models for surgical planning of complex congenital heart defects: an international multicentre study. *European Journal of Cardio-Thoracic Surgery*, 52(6):1139–1148, December 2017. ISSN 1010-7940, 1873-734X. doi: 10.1093/ejcts/ezx208. URL http://academic.oup.com/ejcts/article/52/6/1139/3925909.

[110] Yoo Jin Choo, Mathieu Boudier-Revéret, and Min Cheol Chang. 3D printing technology applied to orthosis manufacturing: narrative review. *Annals of Palliative Medicine*, 9(6):4262–4270, November 2020. ISSN 22245820, 22245839. doi: 10.21037/apm-20-1185. URL http://apm.amegroups.com/article/view/52460/html.

[111] Nicholas Wallace, Nathaniel E. Schaffer, Ilyas S. Aleem, and Rakesh Patel. 3D-printed Patient-specific Spine Implants: A Systematic Review. *Clinical Spine Surgery: A Spine Publication*, 33(10):400–407, December 2020. ISSN 2380-0186. doi: 10.1097/BSD.0000000000001026. URL https://journals.lww.com/10.1097/BSD.0000000000001026.

[112] Hisaki Aiba, Benedetta Spazzoli, Shinji Tsukamoto, Andreas F. Mavrogenis, Tomas Hermann, Hiroaki Kimura, Hideki Murakami, Davide Maria Donati, and Costantino Errani. Current Concepts in the Resection of Bone Tumors Using a Patient-Specific Three-Dimensional Printed Cutting Guide. *Current Oncology*, 30(4):3859–3870, March 2023. ISSN 1718-7729. doi: 10.3390/curroncol30040292. URL https://www.mdpi.com/1718-7729/30/4/292.

[113] Christian Benignus, Peter Buschner, Malin Kristin Meier, Frauke Wilken, Johannes Rieger, and Johannes Beckmann. Patient Specific Instruments and Patient Individual Implants—A Narrative Review. *Journal of Personalized Medicine*, 13(3):426, February 2023. ISSN 2075-4426. doi: 10.3390/jpm13030426. URL https://www.mdpi.com/2075-4426/13/3/426.

[114] Hari Narayan Singh, Sanat Agrawal, and Yashwant Kumar Modi. Additively manufactured patient specific implants: A review. *Archive of Mechanical Engineering*, February 2024. ISSN 2300-1895. doi: 10.24425/ame.2024.149635. URL https://journals.pan.pl/dlibra/publication/149635/edition/130627/content.

[115] Elisabetta M. Zanetti, Gionata Fragomeni, Michela Sanguedolce, Giulia Pascoletti, Luigi De Napoli, Luigino Filice, and Gerardo Catapano. Additive Manufacturing of Metal Load-Bearing Implants 1: Geometric Accuracy and Mechanical Challenges. *Chemie Ingenieur Technik*, 96(4):486–501, April 2024. ISSN 0009-286X, 1522-2640. doi: 10.1002/cite.202300171. URL https://onlinelibrary.wiley.com/doi/10.1002/cite.202300171.

[116] Elisabetta M. Zanetti, Gionata Fragomeni, Michela Sanguedolce, Giulia Pascoletti, Luigi De Napoli, Luigino Filice, and Gerardo Catapano. Additive Manufacturing of Metal Load-Bearing Implants 2: Surface Modification and Clinical Challenges. *Chemie Ingenieur Technik*, 96(4):502–512, April 2024. ISSN 0009-286X, 1522-2640. doi: 10.1002/cite.202300172. URL https://onlinelibrary.wiley.com/doi/10.1002/cite.202300172.

[117] M.G.E. Oldhoff, M.J. Mirzaali, N. Tümer, J. Zhou, and A.A. Zadpoor. Comparison in clinical performance of surgical guides for mandibular surgery and temporomandibular joint implants fabricated by additive manufacturing techniques. *Journal of the Mechanical Behavior of Biomedical Materials*, 119:104512, July 2021. ISSN 17516161. doi: 10.1016/j.jmbbm.2021.104512. URL https://linkinghub.elsevier.com/retrieve/pii/S1751616121001971.

[118] Alexander M. DeHaan, Jacob R. Adams, Matthew L. DeHart, and Thomas W. Huff. Patient-Specific Versus Conventional Instrumentation for Total Knee Arthroplasty: Peri-Operative and Cost Differences. *The Journal of Arthroplasty*, 29(11):2065–2069, November 2014. ISSN 08835403. doi: 10.1016/j.arth.2014.06.019. URL https://linkinghub.elsevier.com/retrieve/pii/S0883540314004276.

[119] Travis Small, Viktor Krebs, Robert Molloy, Jason Bryan, Alison K. Klika, and Wael K. Barsoum. Comparison of Acetabular Shell Position Using Patient Specific Instruments vs. Standard Surgical Instruments: A Randomized Clinical Trial. *The Journal of Arthroplasty*, 29(5):1030–1037, May 2014. ISSN 08835403. doi: 10.1016/j.arth.2013.10.006. URL https://linkinghub.elsevier.com/retrieve/pii/S0883540313007882.

[120] Isobel M Dorling, Lars Geenen, Marion J L F Heymans, Jasper Most, Bert Boonen, and Martijn G M Schotanus. Cost-effectiveness of patient specific *vs* conventional instrumentation for total knee arthroplasty: A systematic review and meta-analysis. *World Journal of Orthopedics*, 14(6):458–470, June 2023. ISSN 2218-5836. doi: 10.5312/wjo.v14.i6.458. URL https://www.wjgnet.com/2218-5836/full/v14/i6/458.htm.

[121] Shuang Ma, Xiaojin Zhang, and Songlin Chen. The Promises and Challenges toward Mass Customization of Healthcare Services. *Systems*, 12(5):156, May 2024. ISSN 2079-8954. doi: 10.3390/systems12050156. URL https://www.mdpi.com/2079-8954/12/5/156.

[122] Pia Reimann, Martin Brucker, Dariusch Arbab, and Christian Lüring. Patient satisfaction - A comparison between patient-specific implants and conventional total knee arthroplasty. *Journal of Orthopaedics*, 16(3):273–277, May 2019. ISSN 0972978X. doi: 10.1016/j.jor.2019.03.020. URL https://linkinghub.elsevier.com/retrieve/pii/S0972978X19300364.

[123] David H. Ballard, Patrick Mills, Richard Duszak, Jeffery A. Weisman, Frank J. Rybicki, and Pamela K. Woodard. Medical 3D Printing Cost-Savings in Orthopedic and Maxillofacial Surgery: Cost Analysis of Operating Room Time Saved with 3D Printed Anatomic Models and Surgical Guides. *Academic Radiology*, 27(8):1103–1113, August 2020. ISSN 10766332. doi: 10.1016/j.acra.2019.08.011. URL https://linkinghub.elsevier.com/retrieve/pii/S1076633219304180.

[124] Philip Tack, Jan Victor, Paul Gemmel, and Lieven Annemans. Do custom 3D-printed revision acetabular implants provide enough value to justify the additional costs? The health-economic comparison of a new porous 3D-printed hip implant for revision arthroplasty of Paprosky type 3B acetabular defects and its closest alternative. *Orthopaedics & Traumatology: Surgery & Research*, 107(1):102600, February 2021. ISSN 18770568. doi: 10.1016/j.otsr.2020.03.012. URL https://linkinghub.elsevier.com/retrieve/pii/S1877056820301249.

[125] Michael Lawless, Brian Swendseid, Natalia Von Windheim, Kyle VanKoevering, Nolan Seim, and Matthew Old. Review of cost and surgical time implications using virtual patient specific planning and patient specific implants in midface reconstruction. *Plastic and Aesthetic Research*, 9:26, 2022. ISSN 23496150. doi: 10.20517/2347-9264.2021.108. URL https://www.oaepublish.com/articles/2347-9264.2021.108.

[126] Meng Meng, Jinzuo Wang, Huagui Huang, Xin Liu, Jing Zhang, and Zhonghai Li. 3D printing metal implants in orthopedic surgery: Methods, applications and future prospects. *Journal of Orthopaedic Translation*, 42:94–112, September 2023. ISSN 2214031X. doi: 10.1016/j.jot.2023.08.004. URL https://linkinghub.elsevier.com/retrieve/pii/S2214031X2300058X.

[127] Shokouh Attarilar, Mahmoud Ebrahimi, Faramarz Djavanroodi, Yuanfei Fu, Liqiang Wang, and Junlin Yang. 3D Printing Technologies in Metallic Implants: A Thematic Review on the Techniques and Procedures. *International Journal of Bioprinting*, 7(1):306, August 2024. ISSN 2424-7723, 2424-8002. doi: 10.18063/ijb.v7i1.306. URL https://accscience.com/journal/IJB/7/1/10.18063/ijb.v7i1.306.

[128] Eduardo García-Rey, Rosario Madero, and Eduardo García-Cimbrelo. THA Revisions Using Impaction Allografting With Mesh Is Durable for Medial but Not Lateral Acetabular Defects. *Clinical Orthopaedics & Related Research*, 473(12):3882–3891, December 2015. ISSN 0009-921X. doi: 10.1007/s11999-015-4483-7. URL https://journals.lww.com/00003086-201512000-00034.

[129] Vahid Moosabeiki, Marius A. Leeflang, Jasper G. Gerbers, Pier H. De Jong, Demien Broekhuis, Yash Agarwal, Jagathes N. Ganesen, Bart L. Kaptein, Rob G.H.H. Nelissen, Mohammad J. Mirzaali, and Amir A. Zadpoor. Additively manufactured shape-morphing implants for the treatment of acetabular defects. *Acta Biomaterialia*, July 2025. ISSN 1742-7061. doi: 10.1016/j.actbio.2025.07.018. URL https://linkinghub.elsevier.com/retrieve/pii/S1742706125005112.

[130] Jue Wang and Alex Chortos. Performance metrics for shape-morphing devices. *Nature Reviews Materials*, 9(10):738–751, September 2024. ISSN 2058-8437. doi: 10.1038/s41578-024-00714-w. URL https://www.nature.com/articles/s41578-024-00714-w.

[131] Miao Miao Yuan and Bo Hua Sun. Adjustable stiffness of chain mail fabrics. *Composite Structures*, 368:119237, September 2025. ISSN 0263-8223. doi: 10.1016/j.compstruct.2025.119237. URL https://linkinghub.elsevier.com/retrieve/pii/S0263822325004027.

[132] Sebastien J.P. Callens and Amir A. Zadpoor. From flat sheets to curved geometries: Origami and kirigami approaches. *Materials Today*, 21(3):241–264, April 2018. ISSN 13697021. doi: 10.1016/j.mattod.2017.10.004. URL https://linkinghub.elsevier.com/retrieve/pii/S1369702117306399.

[133] Sebastien J.P. Callens, Nazlı Tümer, and Amir A. Zadpoor. Hyperbolic origami-inspired folding of triply periodic minimal surface structures. *Applied Materials Today*, 15:453–461, June 2019. ISSN 23529407. doi: 10.1016/j.apmt.2019.03.007. URL https://linkinghub.elsevier.com/retrieve/pii/S2352940719300824.

[134] Sebastien J. P. Callens, Daniel Fan, Ingmar A. J. Van Hengel, Michelle Minneboo, Pedro J. Díaz-Payno, Molly M. Stevens, Lidy E. Fratila-Apachitei, and Amir A. Zadpoor. Emergent collective organization of bone cells in complex curvature fields. *Nature Communications*, 14(1):855, March 2023. ISSN 2041-1723. doi: 10.1038/s41467-023-36436-w. URL https://www.nature.com/articles/s41467-023-36436-w.

[135] Branko Grünbaum and Geoffrey C. Shephard. Tilings by Regular Polygons. *Mathematics Magazine*, 50(5):227–247, November 1977. ISSN 0025-570X, 1930-0980. doi: 10.1080/0025570X.1977.11976655. URL https://www.tandfonline.com/doi/full/10.1080/0025570X.1977.11976655.

[136] D. Chavey. Tilings by Regular Polygons - II A Catalog of Tilings. In *Symmetry 2*, pages 147–165. Elsevier, 1989. ISBN 978-0-08-037237-2. doi: 10.1016/B978-0-08-037237-2.50019-2. URL https://linkinghub.elsevier.com/retrieve/pii/B9780080372372500192.

[137] Lauren Dreier, Trevor J. Jones, Abigail Plummer, Andrej Košmrlj, and P.-T. Brun. Beaded metamaterials, April 2024. URL http://arxiv.org/abs/2404.04227. arXiv:2404.04227 [cond-mat].

[138] S.N. Krivoshapko and V.N. Ivanov. *Encyclopedia of Analytical Surfaces*. Springer International Publishing, Cham, 2015. ISBN 978-3-319-11772-0 978-3-319-11773-7. doi: 10.1007/978-3-319-11773-7. URL http://link.springer.com/10.1007/978-3-319-11773-7.

[139] F Minding. Wie sich entscheiden läfst, ob zwei gegebene krumme Flächen auf einander abwickelbar sind oder nicht; nebst Bemerkungen über die Flächen von unveränderlichem Krümmungsmaafse. In *Band 19*, pages 370–387. De Gruyter, December 1839. ISBN 978-3-11-238986-7 978-3-11-238985-0. doi: 10.1515/9783112389867-019. URL https://www.degruyter.com/document/doi/10.1515/9783112389867-019/html.

[140] Paula Carretero and Ildefonso Castro. A New Approach to Rotational Weingarten Surfaces. *Mathematics*, 10(4):578, February 2022. ISSN 2227-7390. doi: 10.3390/math10040578. URL https://www.mdpi.com/2227-7390/10/4/578.

[141] Mariana Hadzhilazova, Ivailo M Mladenov, and John Oprea. Unduloids and their geometry. *Archivum Mathematicum*, 43(5):417–429, 2007. URL http://dml.cz/dmlcz/108081.

[142] Fabio Crameri, Grace E. Shephard, and Philip J. Heron. The misuse of colour in science communication. *Nature Communications*, 11(1): 5444, October 2020. ISSN 2041-1723. doi: 10.1038/s41467-020-19160-7. URL https://www.nature.com/articles/s41467-020-19160-7.

[143] Chun-Feng Lai, Elena De Momi, Giancarlo Ferrigno, and Jenny Dankelman. Using a Guidance Virtual Fixture on a Soft Robot to Improve Ureteroscopy Procedures in a Phantom. *Robotics*, 13(9): 140, September 2024. ISSN 2218-6581. doi: 10.3390/robotics13090140. URL https://www.mdpi.com/2218-6581/13/9/140.

[144] Jonathan Wei. [Tus caderas feat. Dr jei] Inexperienced doctor's tricks on patients exposed at 3mE TU Delft, December 2021. URL https://www.youtube.com/watch?v=I5Qm_UX6knI&t=11s. Accessed: 2025-04-10.